DESIGN AND SIMULATION OF COILS FOR HIGH FIELD MAGNETIC RESONANCE IMAGING AND SPECTROSCOPY

A Dissertation

by

JOSEPH VINCENT RISPOLI

Submitted to the Office of Graduate and Professional Studies of
Texas A&M University
in partial fulfillment of the requirements for the degree of

DOCTOR OF PHILOSOPHY

Chair of Committee,	Mary Preston McDougall
Committee Members,	Janet Bluemel
	Duncan J. Maitland
	Steven M. Wright
Head of Department,	Gerard L. Coté

August 2015

Major Subject: Biomedical Engineering

ABSTRACT

The growing availability of high-field magnetic resonance (MR) scanners has reignited interest in the in vivo investigation of metabolics in the body. In particular, multinuclear MR spectroscopy (MRS) data reveal physiological details inaccessible to typical proton (^{1}H) scans. Carbon-13 (^{13}C) MRS studies draw considerable appeal owing to the enhanced chemical shift range of metabolites that may be interrogated to elucidate disease metabolism and progression. To achieve the theoretical signal-to-noise (SNR) gains at high B_0 fields, however, *J*-coupling from ^{1}H-^{13}C chemical bonds must be mitigated by transmitting radiofrequency (RF) proton-decoupling pulses. This irradiated RF power is substantial and intensifies with increased decoupling bandwidth as well as B_0 field strength. The preferred ^{13}C MRS experiment, applying broadband proton decoupling, thus presents considerable challenges at 7 T. Localized tissue heating is a paramount concern for all high-field studies, with strict Specific Absorption Rate (SAR) limits in place to ensure patient safety. Transmit coils must operate within these power guidelines without sacrificing image and spectral quality. Consequently, RF coils transmitting proton-decoupling pulses must be expressly designed for power efficiency as well as B_1 field homogeneity.

This dissertation presents innovations in high-field RF coil development that collectively improved the homogeneity, efficiency, and safety of high field ^{13}C MRS. A review of electromagnetic (EM) theory guided a full-wave modeling study of coplanar shielding geometries to delineate design parameters for coil transmit efficiency. Next, a

novel RF coil technique for achieving B_1 homogeneity, dubbed forced current excitation (FCE), was examined and a coplanar-shielded FCE coil was implemented for proton decoupling of the breast at 7 T. To perform a series of simulation studies gauging SAR in the prone breast, software was developed to fuse a suite of anatomically-derived heterogeneous breast phantoms, spanning the standard four tissue density classifications, with existing whole-body voxel models. The effects of tissue density on SAR were presented and guidance for simulating the worst-case scenario was outlined. Finally, for improving capabilities of multinuclear coils during proton coil transmit, a high-power trap circuit was designed and tested, ultimately enabling isolation of ^{13}C coil elements during broadband proton decoupling pulses. Together, this work advanced the hardware capabilities of high-field multinuclear spectroscopy with immediate applicability for performing broadband proton-decoupled ^{13}C MRS in the breast at 7 T.

For my wife, Mandy Jenkins Rispoli

ACKNOWLEDGMENTS

I wish to recognize Dr. Mary Preston McDougall and Dr. Steven Wright for their guidance and dedication throughout the course of my doctoral program. I thank my chair, Dr. McDougall, for imparting a love of MR, providing exciting research opportunities, and delivering unwavering support. I also thank Dr. Wright for his mentorship and commitment to developing my capacity for research. I acknowledge my committee members—Dr. Janet Bluemel for lending her expertise with NMR spectroscopy and Dr. Duncan Maitland for imparting valuable counsel on academic careers and establishing a line of research.

I thank my colleagues at the University of Texas Southwestern Medical Center, namely Dr. Craig Malloy, Dr. Ivan Dimitrov, and Dr. Sergey Cheshkov. Our 7T collaborations in a clinical setting bestowed lasting motivation to expand the capabilities of MRI and MRS.

Last, yet foremost, I acknowledge my family for their support and love. Throughout this endeavor my wife Mandy was my inspiration to realize my potential, and her academic perseverance sets a lofty precedent. I am grateful to my parents and sister for encouraging my continued education, and I thank my boys for sharing their enthusiasm to learn everything there is to know about the universe, especially the planet Earth.

NOMENCLATURE

^{1}H	Hydrogen atom, often dubbed “proton” in MR literature
^{13}C	Carbon-13 isotope
2D	Two-dimensional
3D	Three-dimensional
7T	Compound adjective indicating B_0 = 7 tesla
AC	Alternating current
ACR	American College of Radiology
AP	Anterior–posterior
AWG	American wire gauge
B_0	Static magnetic flux density
B_1	RF magnetic flux density
B_1^-	Circularly-polarized receive B_1
B_1^+	Circularly-polarized transmit B_1
B_2	Proton-decoupling RF magnetic flux density
B_{2max}	Maximum peak amplitude of B_2
BI-RADS®	Breast Imaging Reporting and Data System
CV	Coefficient of variation
CVP	Common voltage point
DC	Direct current
E	RF electric field

EM	Electromagnetic
ESR	Equivalent series resistance
FCE	Forced current excitation
FDA	Food and Drug Administration
FDTD	Finite-difference time-domain
FID	Free induction decay
FOV	Field of view
HF	Head–foot
IEC	International Electrotechnical Commission
LR	Left–right
MR	Magnetic resonance
MRI	Magnetic resonance imaging
MRS	Magnetic resonance spectroscopy
NMR	Nuclear magnetic resonance
NOE	Nuclear Overhauser effect
PCB	Printed circuit board
ppm	Parts per million
RF	Radiofrequency
SAR	Specific absorption rate
SNR	Signal-to-noise ratio
X	Non-^{1}H isotope in multinuclear MR experiment

TABLE OF CONTENTS

LIST OF FIGURES

FIGURE Page

LIST OF TABLES

CHAPTER I

INTRODUCTION

I.1 Background and Motivation

I.1.1 Magnetic Resonance Spectroscopy

In 1946, Bloch and Purcell discerned the phenomenon of nuclear magnetic resonance (NMR), wherein nuclei absorb and emit radiofrequency (RF) magnetic fields detectable by means of Faraday's law of induction (1-3). The first NMR experiments detecting ^{13}C, the carbon isotope exhibiting a magnetic moment, were conducted by Lauterbur and Holm in 1957 (4,5). Development of ^{13}C NMR lagged that of other nuclei (primarily ^{1}H and ^{31}P), however, owing to severely limited sensitivity from multiple fronts: carbon-13 is only 1.1% naturally abundant and its sensitivity inherently suffers given its low gyromagnetic ratio ($\gamma_{13C}/\gamma_{1H} = 0.25$), the cube of which is proportional to NMR signal (6-10). Furthermore, ^{13}C acquisitions are degraded by strong ^{13}C-^{1}H couplings, which may be mitigated by proton decoupling techniques that result in considerable RF power deposition, presenting a patient safety concern (11). Despite the challenges, in vivo ^{13}C magnetic resonance spectroscopy (MRS) studies in humans began in 1989; natural abundance studies by both Bottomley and Heerschap employed broadband proton decoupling at 1.5 T and pushed RF power to the limits imposed by specific absorption rate (SAR) safety guidelines (12-14). Subsequent ^{13}C studies were largely reserved for dynamic studies of metabolic pathways using ^{13}C-enriched glucose (15). Still, the clinical potential of natural abundance ^{13}C MRS is compelling if the low sensitivity can be

overcome (16,17). Spectral resolution is exceptional, since ^{13}C metabolite resonances spread over a wider range as compared to other nuclei (>200 ppm for ^{13}C, 25 ppm for ^{31}P, 10 ppm for ^{1}H) (8,18).

I.1.2 Ultra-High Fields

Whole-body 7T scanners significantly increase the potential of in vivo MRS by enhancing sensitivity and chemical shift dispersion (19-22). However, the increased B_0 magnetic field also intensifies undesired frequency effects, as the ^{1}H Larmor frequency coincides with shorter wavelengths in the human body that make homogeneous excitation a challenge. Furthermore, at higher B_0 radiation losses intensify and decrease coil efficiency, while electric fields may intensify and concentrate to form SAR "hot spots." Designing an efficient RF coil that produces a homogeneous B_1 field throughout a volume becomes much more challenging at high fields. For this reason, whole-body transmit coils are nonexistent in 7T scanners; instead, custom coils tailored to the anatomy of interest are required for high-field studies.

I.1.3 Carbon-13 Spectroscopy of the Breast

Traditionally, the low sensitivity of ^{13}C is addressed with very large voxel sizes and lengthy signal acquisition averaging; however, with the improved sensitivity expected from high-field magnets, localized in vivo ^{13}C MRS may now become more medically pertinent and support a new generation of studies involving the detection of natural abundance ^{13}C (17). For instance, collaborators at the University of Texas Southwestern Medical Center are exploring the role of diet in the pathogenesis of breast cancer, as fat consumption is highly correlated with breast cancer mortality rates (23,24). In particular,

there are indications the ω-6/ω-3 lipid ratio may significant (25). Proton MRS studies at 7 T have been able to quantify total choline and lipid compounds in the human breast (26); however, the more limited ^{1}H chemical shift prohibits discernment of ω-3 and ω-6 fatty acid peaks through conventional proton MRS. Preliminary ^{13}C MRS studies at 7 T have demonstrated the ability to quantify trans-fats (27) and the ω-6/ω-3 lipid ratio in vivo in the breast (28). Still, the role of ^{13}C MRS to detect lipid biomarkers in tumors remains largely unexplored, predominantly hindered by the engineering challenges.

I.1.4 Addressing ^{1}H–^{13}C Heteronuclear Couplings

Heteronuclear couplings between ^{13}C and ^{1}H occur both through proximity in space (nuclear Overhauser effect—NOE) and chemical bonds (*J*-coupling). The former may actually be exploited to improve spectral SNR or detect information on molecular structure, and as NOE enhancement does not require significant irradiated RF power it is not considered a hindrance. The latter coupling mechanism, however, creates an impediment for most in vivo studies; unmitigated, *J*-coupling results in splitting of spectral peaks and the undesired presence of sidebands. The impact of *J*-coupling may be mitigated by applying a proton decoupling RF field (B_2) during ^{13}C signal readout (29). A common ^{1}H pulse sequence employed for proton decoupling is WALTZ-16 (17,30). The power required for B_2 is substantial and increases with both decoupling bandwidth and B_0, presenting significant challenges for both broadband-decoupled and high-field studies. At 7 T, the decoupling bandwidth is typically limited by power capacity and SAR guidelines, together demanding that the ^{1}H coil demonstrate both transmit efficiency and adequate decoupling from ^{13}C coils. To date, a majority of in vivo studies at 7 T have relied on

geometric decoupling to isolate the ^{13}C coil, circumventing the need for tuned trap circuitry (28,31-34). One such 7T coil exploiting geometric decoupling is discussed further in Chapter III. Still, the extremely low sensitivity of ^{13}C implores the development of more complex coil geometries that would otherwise significantly couple to proton coils. A trap circuit implementation capable of isolating ^{13}C coils during broadband proton decoupling is needed to facilitate coil designs focused on maximizing B_2 transmit efficiency and ^{13}C receive sensitivity. Furthermore, given the high levels of RF power irradiation during broadband decoupling pulses, accurate anatomical SAR modeling is obligatory to ensure power deposition from B_2 does not exceed critical levels leading to tissue heating.

I.2 Dissertation Objective and Organization

The primary objective of this work is to advance the hardware capabilities of high-field multinuclear spectroscopy with a particular focus on ^{13}C detection from the breast. This dissertation presents original research addressing four specific aims for achieving this objective:

- Aim 1: Development of a RF shielding scheme suitable for geometrically-dense multi-element 7T coil designs
- Aim 2: Development of a 7T volume breast coil capable of efficient and homogenous B_2 transmit
- Aim 3: Safety modeling of 7T RF coils with anatomically-accurate prone female body phantoms
- Aim 4: Development of multinuclear RF coil trap circuitry for isolating ^{13}C coil elements during high-power broadband proton decoupling

Chapter I of this dissertation commenced by outlining the motivation for this work, discussing the advantages, challenges, and relevance of high-field MR with particular emphasis on ^{13}C MRS breast cancer metabolic research. This chapter continues by

examining the four specific aims in more detail, underscoring their common context for high-field MRS of the breast and framing their combined contribution to the MR research community.

Chapter II explores the EM theory behind loss mechanisms in RF coils and their relationship to B_0 field strength. Of particular concern at high fields are tissue dielectric and radiative losses and their potential to create RF hot spots interior to tissue. Incorporating shielding in RF coils, while not a new technique, becomes increasingly compelling at 7 T to mitigate unwanted *E*-field behavior. The use of multi-element coil arrays is desired to maximize SNR at high fields; however, traditional shielding implementations become prohibitive when considering orthogonal B_1 fields from multiple coil elements. To this end, Chapter II describes a technique dubbed coplanar shielding that is relatively simple to implement, providing many benefits of conventional shielding while limiting undesired B_1 flux blockage from other coil elements. This shielding scheme employs a concentric copper conductor on the same plane as the coil, with the shield width and spacing to the coil influencing its efficacy. With complex RF coil geometries it is often prohibitive to derive tractable analytical solutions to optimize performance; hence flexible full-wave EM modeling methods such as finite-difference time-domain (FDTD) are invaluable for the coil design process. In Chapter II, the efficiency and optimization of the coplanar shielding geometry is methodically analyzed through FDTD modeling, with specific cases prototyped, verified on the bench, and demonstrated with 7T imaging. The benefits of coplanar shielding are quantified for both transmit and receive coils, and design guidelines are presented for optimizing B_1 transmit (B_1^+) efficiency. As a result,

this flexible shielding scheme may be readily employed on high-field coils and is particularly advantageous for efficiently transmitting proton decoupling pulses for ^{13}C MRS.

Performing broadband decoupling to mitigate *J*-coupling at 7 T necessitates an efficient transmit coil tuned to the Larmor frequency of ^{1}H—298 MHz. Chapter III presents a quadrature ^{1}H transmit breast coil with a Helmholtz-saddle configuration that provides anatomical image-based localization and homogeneous proton decoupling. The asymmetric loading effects of the breast and thorax are increasingly pronounced at higher frequencies; here, this design challenge is mitigated by using the forced current excitation (FCE) technique to drive equal currents to coil elements. FCE drives the top and bottom loops in a Helmholtz coil, irrespective of the loading asymmetry, resulting in homogenous B_2 excitation throughout the breast. Furthermore, the efficiency gained with quadrature operation is particularly beneficial when considering SAR power limitations. The results presented in this chapter include impressive B_2 homogeneity throughout the breast and the acquisition of the first in vivo proton-decoupled ^{13}C spectrum from the breast at 7 T.

Since the early days of ^{13}C MRS at 1.5 T, broadband proton decoupling has presented a SAR concern for patient safety. Electromagnetic modeling is an important tool for characterizing SAR during coil transmit, as SAR is a direct consequence of RF *E* fields in the body. The necessity of understanding the nature of *E*-field effects in the body becomes increasing compelling at high fields and especially so with broadband proton decoupling, as SAR is proportional to both B_0^2 and B_2^2. For high-field breast studies, accurate anatomical SAR modeling must be performed to determine RF coil safety

parameters for in vivo use. Accordingly, Chapter IV investigates the safety of transmit coils for breast MR at 7 T, with a particular focus on how breast tissue density affects coil operation and safety. Several female whole-body voxel models are available to the scientific community for simulating biological EM effects; however, all were developed in the standing or supine position. Consequently, no female body voxel models exist for simulating prone MR scanning in the pendant breast, as is typically performed to avoid respiratory motion artifacts. Thus, to accurately predict SAR in a pendant breast with an adjoining body load, a method was developed and detailed in Chapter IV for fusing standalone breast phantoms with available whole-body voxel models. SAR modeling of 11 different breast phantoms, encompassing the broad range of tissue densities among the patient population, was then performed to characterize coil performance and determine the locations most susceptible to tissue heating. The results in this chapter present the first detailed account of the significant increases in expected SAR when performing high-field MR studies of denser breast tissue. This knowledge is crucial for safely performing high-power studies such as broadband proton-decoupled ^{13}C MRS at 7 T.

Despite the success of the FCE coil described in Chapter III for detecting in vivo ^{13}C spectra, additional SNR is required to better quantify metabolite peaks. To this end, arrays of small coil elements have long been employed to dramatically improve MR sensitivity near the surface while collectively detecting NMR spins further into the body (35). While ^{1}H array coils designs may be considered well-established, unique engineering challenges are presented for interrogating X-nuclei such as ^{13}C. Chief among them is the inductive coupling between ^{13}C and ^{1}H elements that, unless mitigated, results in

substantial energy transfer between coils. Chapter V examines trap circuitry for providing RF coil isolation in multinuclear MR experiments an. The design criteria presented within this chapter mandate the traps operate under the most extreme conditions with respect to power and sensitivity, i.e., to acquire broadband proton-decoupled ^{13}C MRS at 7 T. The Philips Achieva RF amplifiers are capable of outputting 4 kW at each Larmor frequency, and the WALTZ-16 decoupling sequence typically utilizes a large proportion of this power capability. The distinction between *LC* and *LCC* traps is reviewed, and the advantages and challenges of building trap circuits with various inductor and capacitor components are delineated. Multiple trap designs were evaluated on the bench and utilized at 7 T to detect broadband proton-decoupled ^{13}C from a lipid phantom. A particular *LCC* trap design built from a coaxial stub inductor and high-voltage porcelain chip capacitors is highlighted owing to both its exceptional performance and adaptability for small array coil elements with diverse spatial orientations. This trap circuit design is instrumental in the design and implementation of a multi-channel ^{13}C receive array for proton-decoupled, natural abundance ^{13}C MRS of the breast.

Chapter VI concludes this dissertation with a review of the findings presented herein and their combined impact on multinuclear MRS studies of the breast at 7 T. Furthermore, this chapter discusses potential future directions for this line of research. Finally, Chapter VI closes by considering how both the hardware and EM modeling techniques presented in this work may be readily applied to other anatomical regions and problem areas.

I.2.1 Dissertation Style

The formatting style used for reference citations and table/figure titles follows that of *Magnetic Resonance in Medicine*. The chapter organization of this dissertation follows the Journal Article Style Format as delineated by the Texas A&M University Office of Graduate and Professional Studies and the Department of Educational Psychology. Accordingly, Chapters II-V present manuscripts formatted and intended for publication, with each chapter addressing one of the four specific aims of this dissertation.

CHAPTER II

ANALYSIS OF COPLANAR SHIELDING AS A METHOD TO IMPROVE EFFICIENCY AND PARALLEL IMAGING PERFORMANCE OF RADIOFREQUENCY COILS

II.1 Introduction

At high fields, radiative and dielectric tissue losses increase and account for a more significant share of radiofrequency (RF) coil loss (22,36,37). Compensating for these losses by boosting transmit power intensifies the electric (E) field, increasing the specific absorption rate (SAR) and consequently the risk of tissue heating. Adding RF shields is a standard approach to alleviate B_0-dependent radiative losses and becomes increasingly compelling at higher fields (38). Adriany et al. characterized the performance of a variety of 7T surface coils with conventional shielding, reporting appreciable benefits over unshielded versions and categorically recommending RF shields for coils larger than 7 cm (39).

To better fit within required form factors, a variety of shielding methods have been explored as alternatives to typical copper sheeting. For instance, shielding is inherently provided on the return path of the resonance structure when employing transmission line elements in microstrip or transverse electromagnetic (TEM) coils (40-43). In the traditional case of lumped-element surface or volume coils a separate shielding structure is required. One such scheme adds concentric conductors around each coil; variations of this method have been shown to realize several objectives of RF shielding, including

reduced radiative losses, inter-element coupling, and load-induced frequency shift, while also limiting flux blockage from other elements (44-49). A simple implementation, dubbed coplanar shielding, encircles the coil with a continuous copper loop. Notably, this scheme, in contrast to other concentric shielding approaches, maintains the overlapping ability of array elements. Preliminary results with a single-loop surface coil indicated a coplanar shield improved the coil filling factor and reduced total coil loss at 7 T, thus improving transmit efficiency (48). This work further examines coplanar shielding with emphases on improving signal-to-noise ratio (SNR), radiative and dielectric tissue losses, parallel imaging performance, and SAR. Seeing as complex coil designs often lack tractable analytical solutions, the utility of full-wave electromagnetic modeling for determining the shield geometry is demonstrated, and resulting design guidelines are verified by bench measurements and imaging examples. Two example coil configurations are presented: a circular loop surface coil and a half-volume five-element receive array. Results confirm coplanar-shielded coils benefit from improved SNR and transmit efficiency with reduced *E*-field losses. Furthermore, inter-element isolation and accelerated imaging performance are shown to improve in the coplanar-shielded receive array. Thus, given its simple construction and appreciable benefits, coplanar shielding presents an attractive design option for high-field coils.

II.2 Theory

II.2.1 Coil Losses

Although all sources of coil resistance—ohmic, radiative, and tissue losses—escalate with increased frequency, the components most intensified at higher B_0 fields are radiation loss

and tissue dielectric loss stemming from electric field displacement current. For a loop coil with diameter d operating at frequency ω, the tissue dielectric and radiation losses are proportional to ω^4 while the latter also scales with d^4 (37). Consequently, mitigating these loss mechanisms' effects on imaging quality becomes more imperative at high fields, particularly with larger coils. Furthermore, tissue heating in localized regions with intense E fields, dubbed hot spots, presents a paramount high-field patient safety concern; hence a reduction of E fields is vital considering the quadratic relationship to power deposition in tissue, given SAR = $\sigma|\mathbf{E}|^2/(2\rho)$ [W/kg], where σ is the electrical conductivity [S/m], $\mathbf{E}$ is the peak electric field vector [V/m], and ρ is the material density [kg/m^3].

Tissue dielectric losses from displacement currents are associated with both the non-conservative and conservative electric fields. The non-conservative E field associated with dB/dt is an inevitable consequence of the B_1 field and is present throughout the coil's sensitive region, with its impact influenced by permittivity of the sample and coil homogeneity. Coplanar shielding manipulates the non-conservative E field by compressing the near-zone B_1 field, as a result spatially confining dielectric losses in the patient. This effect may be considered steering the B_1 field and may also be employed to produce a greater coil filling factor, that is, improve the ratio of magnetic energy stored in the region of interest (ROI) versus all space. The optimal coplanar shield spacing is not straightforward, however; closer proximity of shielding to the coil has been shown to improve coil loss until a critical point where near-field B_1 compression catastrophically diminishes SNR (38).

The conservative E field is produced in opposition to the coil electromotive force (EMF) and can be mitigated in coil design by both segmentation and shielding. RF coils are typically designed to maximize current uniformity in order to produce homogeneous B_1. To this end, segmenting lumped-element coil conductors with capacitors reduces current phase shifts, decreasing the voltage potential across each break and, accordingly, the conservative E field's average value throughout the sample (50). Taming the conservative E field with coil segmentation reduces capacitive coupling to both the sample dielectric and the coil cabling, typically outweighing reduced performance from the capacitors' added ohmic losses (51,52). Near-coil shielding such as the coplanar scheme may be employed to further shape the conservative E field; that is, the coil's stray capacitance is smoothed by the uniformly-spaced shield conductor (51), with the coil and shield traces analogous to an asymmetric coplanar-strip line (53). Note a coplanar shield, or any shield for that matter, will add to inductive losses associated with B_1-induced currents on the shield surface. However, these inductive losses are typically outweighed by a reduction of other loss mechanisms, easily verifiable by comparing coil quality factors (Q). Ultimately, a spatial confinement and smoothing of the conservative E field lessens the impact of varying the dielectric load as multiple patients or anatomies are imaged with the coil (54). In this way, effective shielding reduces sample-induced tuning shifts and facilitates balancing the coil at the feed (51).

Radiative losses present a concern at higher fields; while coils designed to interrogate a specific anatomy remain the same physical size, shorter wavelengths at higher fields increase the electrical length of coil conductors. The extent that an RF coil

behaves as an antenna is quantified by its radiation resistance, or in power terms the radiation efficiency, the latter being the ratio of radiated power over the net input power to the coil. The radiation efficiency from both surface and volume coils has been shown to scale upward with fields strength; however, at high fields the contribution of radiative losses is much less substantial in the presence of a high-dielectric sample (55,56). Thus, at high fields radiative losses are expected to be more significant in proximity to lower-dielectric materials such as adipose tissue, as opposed to higher-dielectrics including muscle or brain.

While the addition of coplanar shielding may reduce radiation from the coil, it is necessary to consider the shield's own radiative field. It is common practice to bridge gaps in RF shields with a large capacitance, allowing RF currents to pass while preventing gradient-induced eddy currents. Maintaining the RF current path mitigates induction of an associated EMF voltage and conservative E field, yet it permits the shield to act as a loop antenna. For an electrically small-to-medium loop antenna, the radiated field is maximum on the coil plane and lowest along its axis (57); thus, with a coplanar shield the subject is typically positioned away from the maximum radiating plane. Still, as B_0 or the coil size is increased, care must be taken to segregate the antenna mode of the coplanar shield from the B_1 frequency. Recall the first anti-resonant mode of a loop antenna with diameter d occurs at angular frequency $\omega = c/d$, or equivalently, when $d = \lambda/2\pi$ (58). If tuned near the coil's frequency, e.g., a 16-cm diameter coplanar shield at 7 T, this odd current mode can interfere with the desired balanced coil mode and act as a radiator of coupled energy.

II.2.2 Metrics for Shield Analysis

The effective transmit and receive coil sensitivities, $|\mathbf{B}_1^+|$ and $|\mathbf{B}_1^-|$, are defined as the modulus of the B_1 component rotating with and opposite the direction of nuclear precession, respectively. The Q-factor is an effective measure of net coil losses; thus a higher coil Q, as anticipated with a well-executed shield implementation, indicates a net decrease in coil losses and higher SNR (38). Likewise, a loaded-to-unloaded Q ratio (Q_L/Q_{UL}) lower than 0.5 is desired as it suggests more inductive losses and thus ample magnetic field energy is stored in the sample (59). However, qualifying a coil with this ratio alone has drawbacks when fields extend beyond the homogeneous B_1 ROI; thus, a better measure of coil performance is the transmit efficiency, computed as the average $|\mathbf{B}_1^+|$ in the ROI for a given input power. Homogeneity in the ROI can be evaluated with the coefficient of variability (CV), calculated by dividing the average $|\mathbf{B}_1^+|$ by the standard deviation.

The average E field in the sample may be assessed in relation to average $|\mathbf{B}_1^+|$ in the ROI. Along with the aforementioned conservative and non-conservative fields, this metric also includes any radiated field attenuating in the sample. In the near-field presence of a load, this latter E-field component is not accounted for in radiation efficiency calculations only measuring wave propagation in the far field. Accordingly, a superior determination of antenna behavior may be obtained by first calculating radiation efficiency in the unloaded case with far-field measurements. Then the contribution of radiative losses to the total power dissipated in tissue may be gauged by scaling the

unloaded radiation efficiency with ohmic (conductive) losses in the unloaded versus loaded simulation results.

As SAR is proportional to the squared electric field modulus, i.e., $|\mathbf{E}|^2$, it is desirable to achieve high average $|\mathbf{B}_1^+|$ while minimizing the peak E field, i.e., $|\mathbf{E}|_{max}$. Hence a lower ratio of $|\mathbf{E}|_{max}^2/|\mathbf{B}_1^+|$ throughout the coil's ROI may be construed as an indicator of peak local SAR reduction; furthermore, spatial E-field averaging may be performed to mitigate bias from any extremely localized hot spots.

II.3 Methods

II.3.1 Electromagnetic Modeling

The effects of coplanar shielding on various performance metrics were analyzed with full-wave electromagnetic modeling. Simulations were performed using commercial FDTD software (XFdtd® 7.4, Remcom, State College, Pennsylvania, USA). Two coil sizes were modeled, with mean diameters of 8 cm and 16 cm; for each case a single coil was centered at the origin on the xz plane, principally producing y-directed B_1. Two coil conductor configurations were modeled individually: printed circuit board (PCB) and wire. The PCB trace was meshed as a two-dimensional sheet (4-mm width for 8-cm coil, 6-mm width for 16-cm coil), while wire was modeled as a three-dimensional revolved solid with a circular cross section (18 AWG/0.5-mm radius for 8-cm coil, 12-AWG/1-mm radius for 16-cm coil).

The parameterization features available in commercial electromagnetic solver packages may be straightforwardly exploited to perform studies of coplanar shielding behavior. The shield width and coil-to-shield spacing (delineating shield radius) were

parameterized in XFdtd, and QtScript macros were developed to construct 100 combinations of shield width and spacing, in 1-mm steps from 1-10 mm. The coplanar shield was meshed as a two-dimensional sheet. The unshielded case was also simulated for each coil geometry. All conductors were assigned the electrical properties of copper (σ = 59.6 MS/m and ε_r = 1). While variable spacing from the coil to the load is known to affect concentric shielding performance (44), in this study load spacing was simulated at one distance to mimic 1-cm padding present in coils utilized for in vivo studies. A slab measuring 32 × 32 × 20 cm was centered and spaced 1 cm below the coil and assigned the electrical properties of muscle at 7 T (σ = 0.55 S/m and ε_r = 80).

All coils included equally-spaced, 2-mm wide breaks (six for 8-cm coil, 12 for 16-cm coil) to accommodate the feed and segmentation capacitors. Capacitor values for each simulation were assigned to exhibit uniform current around the loop. To achieve this goal, each cases was first simulated with all breaks populated by ideal (i.e., infinite impedance) current sources. The resulting input impedances of the current sources were imported into MATLAB® 8.3 (MathWorks, Natick, Massachusetts, USA) and the capacitances required to cancel the average inductances of the current sources were calculated (60). The capacitor values were then fed back into XFdtd with custom QtScript code facilitating unique assignment for each shielded case. The capacitor definition included 0.2-Ω resistance to model ohmic losses from equivalent series resistance and solder resistivity (61). A second round of simulations were run utilizing a single 50-Ω voltage source across the break at the +x extent of each coil. This untuned feeding arrangement was validated against a more computationally lengthy simulation incorporating a shunt tuning capacitor

in the feed definition; agreement was substantiated by comparing input impedance, field, and power results. For all cases, the mesh was excited by a broadband pulse and simulations converged when transients dissipated to levels -50 dB below peak values.

To illustrate the value of employing coplanar shields with variable loads and B_0 field strengths, additional simulation cases were performed with the 16-cm PCB coil. A lower-dielectric phantom representing adipose tissue (σ = 40 mS/m and ε_r = 5.6) was modeled at 7 T, with the expectation that radiative losses would become more significant. Also, simulations with the muscle load were performed at 3 T. To present a straightforward comparison to 7 T, the dielectric values of the phantom were kept constant, despite muscle tissue exhibiting lower conductivity and permittivity at 128 MHz, the Larmor frequency at 3 T. Capacitor values were once again assigned to optimize current at 3 T.

The two PCB coils and 12-AWG wire coil were gridded with maximum 1-mm Yee cell dimensions, while the 18-AWG wire coil was gridded with maximum 0.5-mm dimensions. More conservative gridding with 0.25-mm dimensions was evaluated for specific geometries and verified to produce results in very close agreement. Owing to the two-dimensional geometry of the PCB conductors and coplanar shields, these conductors were located on only one xz plane of Yee cells in the mesh, while the wire conductors were located on the central xz plane of the coil with additional, narrower cross sections located on the two adjacent xz planes. A surface conductor correction was applied to copper planes to ensure conductivity consistent with five skin depths. Remcom's conformal meshing algorithm for curved objects was applied to all conductors after

validation against a case using 0.25-mm gridding with the algorithm disabled. For all cases, the model was surrounded by a quarter wavelength of free space padding cells and the boundary comprised seven perfectly matched layers. Simulations were run on a workstation with two linked NVIDIA GeForce® GTX 780 GPU cards, each with 3 GB RAM and 2304 cores, resulting in an average computational time of 12 minutes. Convergence was determined by transients dissipating to -50 dB deviation from the excitation pulse. The ROI of the coil was defined as the hemisphere below the loop. Three planar sensors captured steady-state *B*- and *E*-field data at 298 MHz, the Larmor frequency at 7 T. Volume sensors were not utilized owing to the requisite data storage overhead. The circuit components, i.e., feeds and capacitors, recorded both transient and steady-state data. Renderings of the coil, load, and sensor planes are illustrated in Figure II-1.

Resulting sensor data were imported into MATLAB for post-processing. The volume of each Yee cell was taken into consideration when computing average field values since cell dimensions varied due to the adaptive gridding. FDTD results from

Figure II-1. Renderings of surface coil adjacent to the phantom load and EM field sensors. (**a**) 16-cm coil with coplanar shield centered over dielectric slab. (**b**) Sensors 1a and 1b were located on the xy and yz planes, respectively, both orthogonal to the coil and consisting of hemispheres (of the coil radius) excluding the region within 1 cm of the coil. (**c**) Sensor 2 was a square sensor located 1 mm inside the near face of the slab on the xz plane.

selected shielding geometries were validated against in-house full-wave spectral-domain analysis code (62) by comparing calculated input impedance, current uniformity, and field patterns over the uniform loading phantom.

The quality factor Q was calculated from the initial round of FDTD simulations utilizing ideal current sources. The input impedances (with resistance R and reactance X) were summed and Q-factors were calculated from $Q = \omega L/R = X/R$, with R including the aforementioned ohmic capacitor losses. The remaining metrics were computed with results from the second round of simulations. SNR was determined from the average $|\mathbf{B}_1^-|$ in the ROI divided by $\sqrt{R_{\text{in}}}$ at the feed. Transmit efficiency was calculated by dividing the average $|\mathbf{B}_1^+|$ in the ROI by the square root of power dissipated from combined ohmic, radiative, and tissue losses. Average $|\mathbf{E}|/|\mathbf{B}_1^+|$ in the ROI was computed to assess sample losses due to E fields. Local SAR was gauged by the ratio of computed $|\mathbf{E}|_{\text{max}}^2/|\mathbf{B}_1^+|$ throughout the coil's ROI.

Finally, radiation efficiency is determined in FDTD as the proportion of power radiating into the mesh boundary; if the model includes a sample load, this metric excludes radiation dissipated in the sample, and it should also be noted that most power radiating out of the FDTD mesh would ultimate dissipate in the subject due to confinement by the magnet bore and magnet room RF screen (63).

II.3.2 Radiofrequency Coils

II.3.2.1 Circular Loop Surface Coil

A single circular loop surface coil was evaluated with three separate shielding topologies—coplanar shielded, and ground plane shielded, and unshielded. The surface

coil was etched on 1.6-mm thick, 1-ounce copper-clad FR-4 PCB with 16-cm mean diameter and 6-mm conductor width. Note the PCB copper thickness should be at least fivefold the RF skin depth to prevent unnecessary ohmic losses; in this case, the 1-ounce copper thickness of 34 μm is about nine times the 3.8-μm skin depth at 298 MHz. The coil was segmented by 12 equally-spaced 2-mm breaks. Following simulation data analysis, a coplanar shield with 7-mm conductor width and 176-mm inner diameter (resulting in 5-mm spacing between coil and shield) was fabricated for placement around the loop coil. The ground plane shielded case was evaluated by orienting a copper sheet 4.5 cm below the surface coil, a separation previously determined to be best suited for surface coils of this size (39). Different capacitors values, 8.2 and 10 pF (Passive Plus, Huntington, New York, USA), were utilized for the unshielded and shielded cases, respectively. The coils were loaded with a 25-cm diameter, 11-cm tall cylindrical saline phantom ($\sigma = 0.55$ S/m). Each coil was evaluated in unloaded and loaded conditions, with all cases balanced matched to 50 Ω with variable capacitors (SGNMNC1206E, Sprague-Goodman, Westbury, New York, USA; NMAJ55HVE, Voltronics, Salisbury, Maryland, USA). *Q*-factors were measured with a network analyzer (Keysight E5071C, Santa Clara, California, USA) based on the -7 dB width of the S_{11} response (64).

II.3.2.2 Receive Array

A custom "Olympic rings" array of five overlapping elements was constructed to compare coplanar-shielded and unshielded parallel imaging performance. Each element was shaped from 18-AWG wire formed into an 8-cm diameter loop and segmented into six equal arcs. The resulting gaps were connected by ceramic chip capacitors (100B series, American

Technical Ceramics, Huntington Station, New York, USA; 1111C series, Passive Plus). Elements were mounted on a half-cylindrical acrylic former with a 78-mm radius. A standard active trap configuration incorporating the match capacitor, variable solenoid (164 series, Coilcraft, Cary, Illinois, USA), and PIN diode (MA4P7470F-1072, MACOM, Lowell, Massachusetts, USA) detuned the array elements during transmit, with additional protection provided midway around the loop by a passive trap incorporating dual anti-parallel diodes and the tune capacitor. Inter-element decoupling was accomplished via optimal geometric overlap for nearest neighbors, while all elements utilized low-input impedance preamplifier decoupling (65). Standard resonant cable traps were included at each element's feed. For the shielded array, each wire element was encircled by a coplanar shield etched on 0.2-mm thick, 1-ounce copper-clad FR-4 PCB with 89-mm inner diameter and 97-mm outer diameter; this geometry was determined from simulation results further discussed in the next section. Each individual element's coplanar shield remained electrically isolated by affixing insulating polyimide tape between overlapping conductors. Photographs of the arrays are shown in Figure II-2.

The half-volume arrays were loaded with a cylindrical 1-gallon saline phantom, with conductivity of muscle at 7 T ($\sigma = 0.55$ S/m), spaced 5 mm from the conductors. *Q*-factor measurements were performed using the procedure described above for the surface coil. Imaging was performed on a whole-body 7T scanner (Achieva, Philips Medical Systems, Cleveland, Ohio, USA) with the receive array and phantom positioned inside a commercial quadrature transmit head coil (Nova Medical, Wilmington, Massachusetts, USA). A 3D T_1 High-Res Isotropic Volume Excitation (THRIVE) sequence was utilized

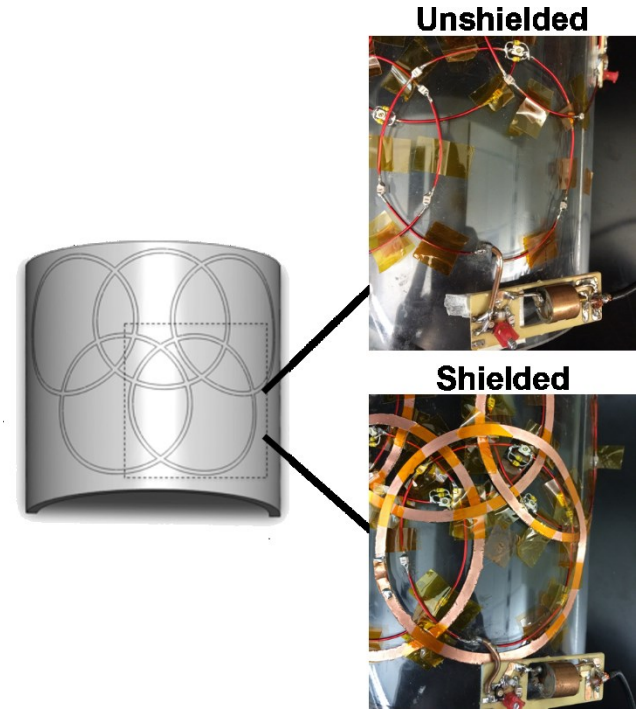

Figure II-2. Rendering and photographs of the unshielded and coplanar-shielded "Olympic rings" 5-element receive arrays. The inset photographs include the coaxial cable and the PCB incorporating the cable trap and active detuning circuit.

with 4-ms TR, 1.83-ms TE, 8° flip angle, 1-mm isotropic resolution throughout an 18 × 18 × 32 cm FOV. Array performance was evaluated from resulting images by comparing SNR and noise correlation matrices, with noise data acquired per the methodology detailed in (66). To gauge accelerated imaging performance, bidirectional SENSE scans (67) were executed with reduction factors of up to $R = 3$ in the phase-encoding direction (right/left—RL) and up to $R = 2$ in the frequency-encoding direction (feet/head—FH). The resulting coil geometry factors (g) were calculated and illustrated as g-factor maps on a coronal slice through the phantom.

II.4 Results

II.4.1 Electromagnetic Modeling

Simulation results suggest, regardless of coil size, a specific coil-to-shield spacing exists that optimizes transmit efficiency for any particular dielectric load at a given B_0. Furthermore, a qualitative comparison confirmed the aforementioned metrics from wire and PCB coils with equivalent mean diameters are in agreement. Still, optimizing transmit efficiency comes at the expense of other metrics, including SNR and local SAR. Thus, the design decision is ultimately a tradeoff between several performance metrics.

For muscle imaging at 7 T, modeling results suggest transmit efficiency peaks when the coplanar shield's inner radius is spaced 8 mm from the mean coil diameter, with wider shield widths delivering diminishing improvements. Plots illustrating the transmit efficiency, average $|\mathbf{E}|$ in the sample, relative SNR, $|\mathbf{B}_1^+|$ CV, relative peak local SAR, and radiation efficiency are displayed in Figure II-3 and Figure II-4 (color-weighted and line plots, respectively) for the 8-cm loop, while corresponding plots for the 16-cm loop are shown in Figure II-5 and Figure II-6. As shown in Figure II-4a, a 10-mm wide shield is expected to provide 28% improvement in $|\mathbf{B}_1^+|$ efficiency against the unshielded case. In general, an increasingly wider coplanar shield benefits transmit efficiency and SNR while reducing the average E field in the sample. $|\mathbf{B}_1^+|$ homogeneity is generally improved with increased shield spacing from the coil. Notably, all shielded cases improve the ratio of average $|\mathbf{E}|/|\mathbf{B}_1^+|$ compared to the unshielded case, indicating proportionately reduced losses stemming from the E field. The radiation efficiency is quite

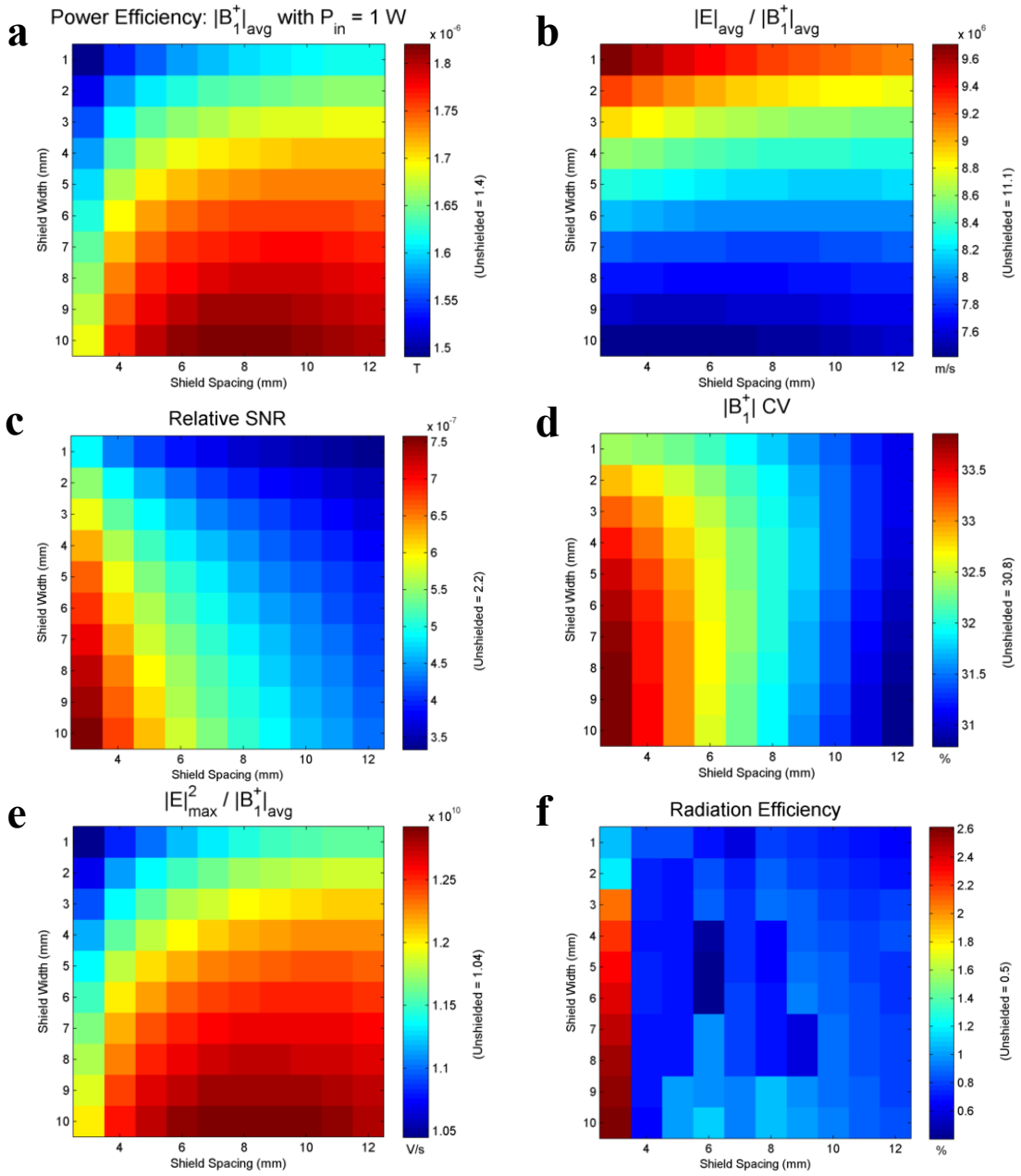

Figure II-3. Color-weighted simulation results for a single 8-cm loop PCB surface coil loaded with muscle at 7 T. (**a**) $|\mathbf{B}_1^+|$ transmit efficiency peaks at 8-mm spacing and wider shield widths. (**b**) The average *E* field reduces with greater shield widths. (**c**) SNR improves with closer shield spacing and greater shield widths. (**d**) The coefficients of variation suggest shield geometries with shorter spacing produce marginally worse $|\mathbf{B}_1^+|$ homogeneity. (**e**) The indicator of peak local SAR follows the transmit efficiency plot of (a), as dominant *dB*/*dt* induced *E*-field losses result with greater spatial confinement of B_1. (**f**) Radiation efficiency is insignificant with a large high-dielectric load at 7 T unless the shield is extremely close (3-mm spacing to mean = 1-mm air gap) to the coil conductor.

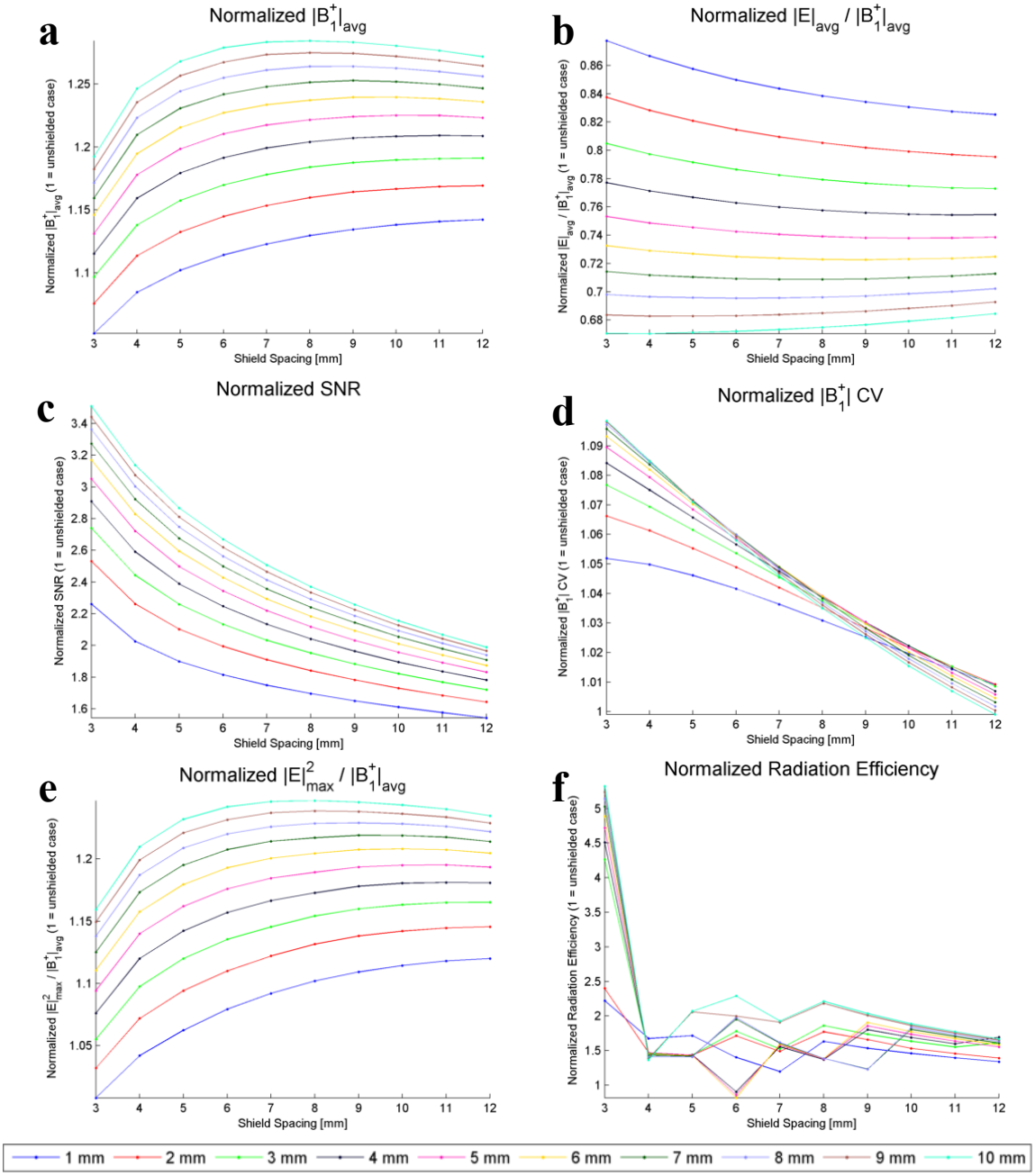

Figure II-4. Normalized line plots (unshielded coil = 1) corresponding to Figure II-3 for a single 8-cm loop PCB surface coil loaded with muscle at 7 T. The legend at bottom identifies plot colors for each shield width.

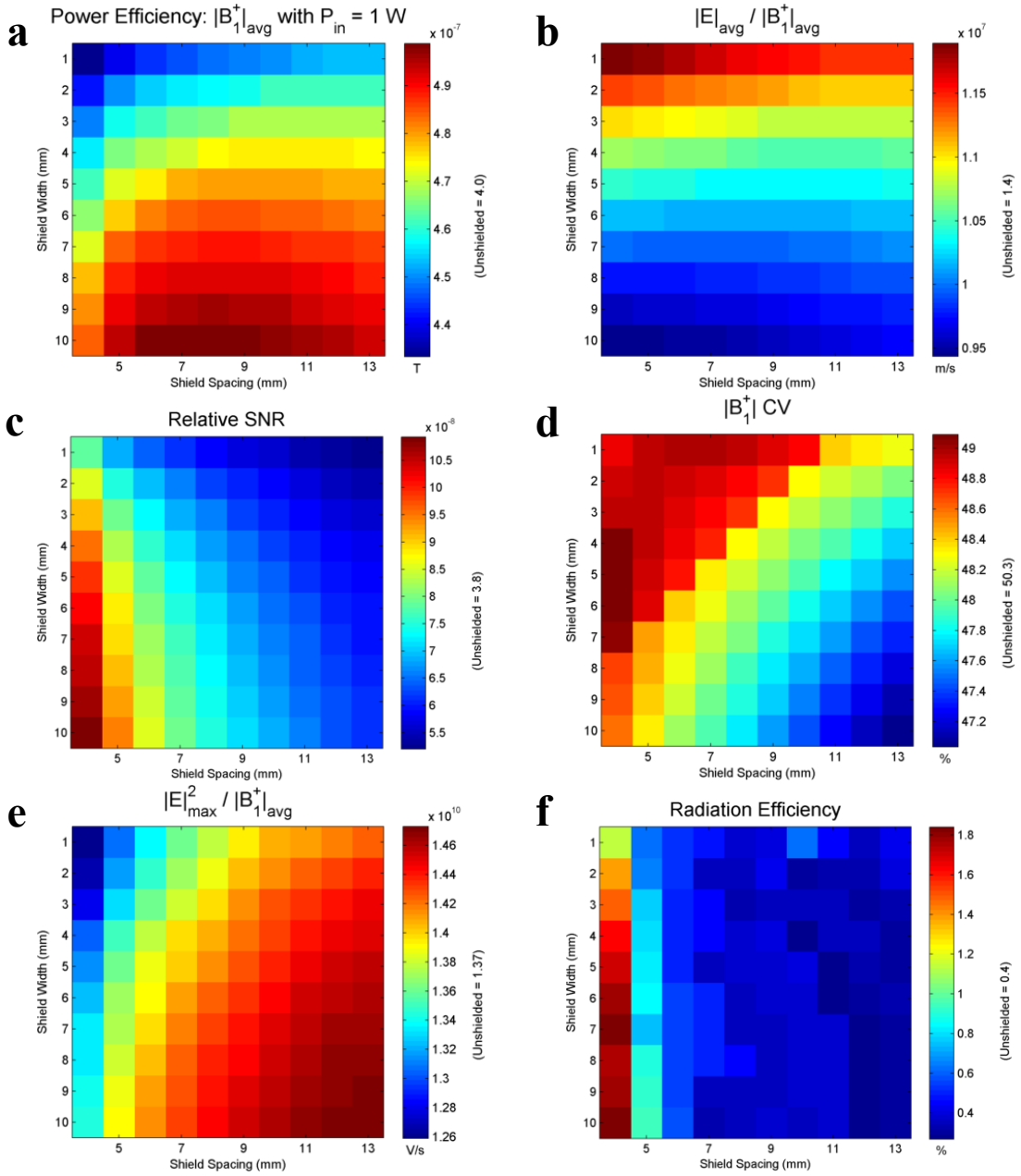

Figure II-5. Color-weighted simulation results for a single 16-cm loop PCB surface coil loaded with muscle at 7 T. (**a**) $|\mathbf{B}_1^+|$ transmit efficiency peaks at 8-mm spacing and wider shield widths. (**b**) The average *E* field reduces with greater shield widths. (**c**) SNR improves with closer shield spacing and greater shield widths. (**d**) The $|\mathbf{B}_1^+|$ coefficients of variation suggest shield geometries with shorter width and spacing result in greater inhomogeneity; still, all shielded cases present a marginal improvement. (**e**) The indicator of peak local SAR suggests greater shield spacing and width results in higher SAR. (**f**) Radiation efficiency is insignificant with a large high-dielectric load at 7 T.

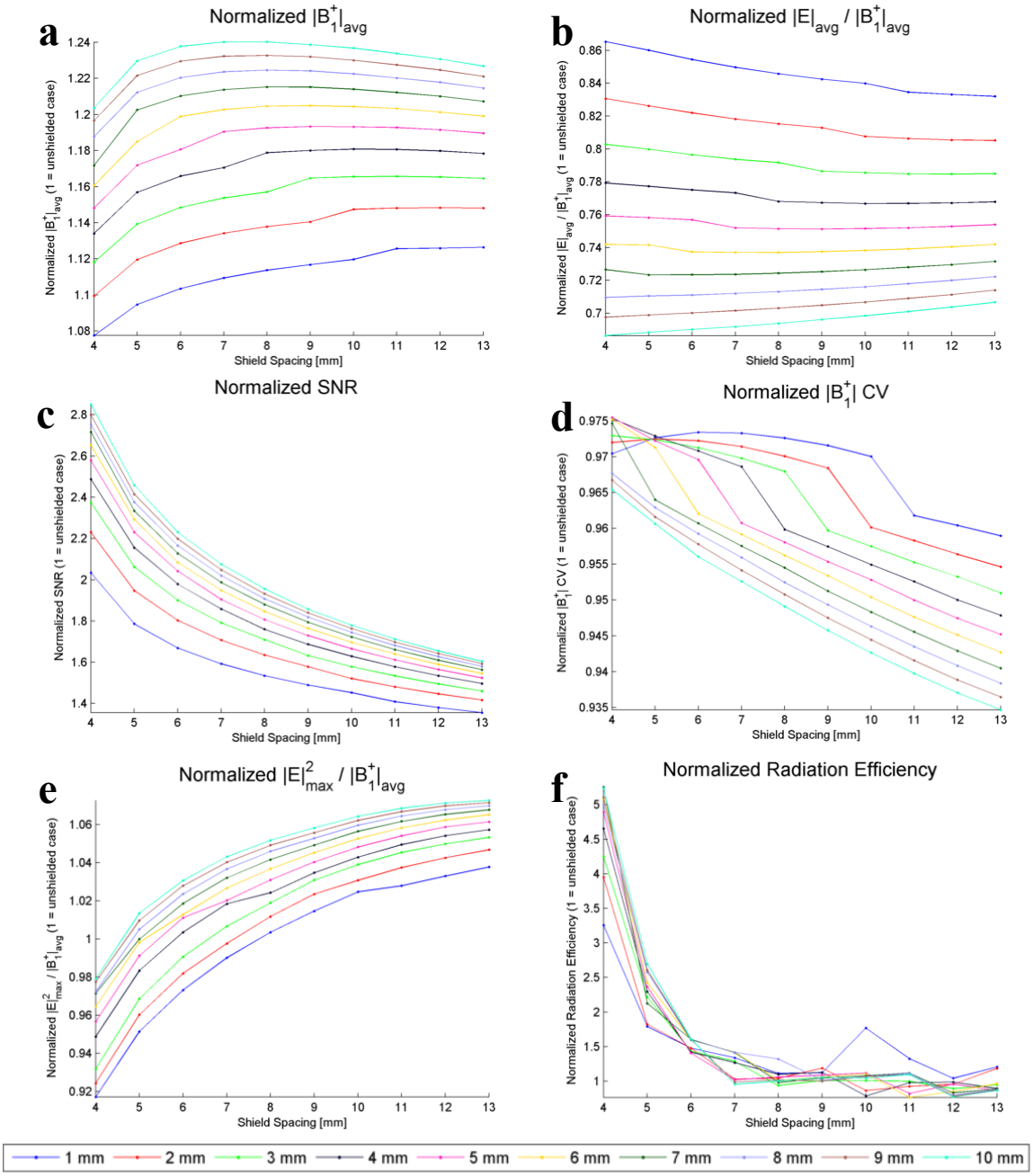

Figure II-6. Normalized line plots (unshielded coil = 1) corresponding to Figure II-5 for a single 16-cm loop PCB surface coil loaded with muscle at 7 T. The legend at bottom identifies plot colors for each shield width.

low with the large muscle load at 7 T; instead, the majority of coil losses originate from the dB/dt-induced non-conservative E field. Note the $|\mathbf{E}|_{max}^2/|\mathbf{B}_1^+|$ plots indicate a potential increase in peak local SAR of up to 25% depending on shield geometry.

As expected, the appropriate shield geometry differs with varying dielectric loads. Results with the 16-cm PCB coil at 7 T with the adipose tissue load are presented in Figure II-7 and Figure II-8. These cases extend to shield spacing of 23 mm, yet a maximum transmit efficiency was not yet discerned, indicating further improvement with additional spacing. Radiative losses at 7 T become much more significant with the lighter-dielectric load, as shown in Figure II-7f—the unshielded coil exhibited radiation efficiency of 11%, easily reduced by employing a shield, preferably with width of at least 6 mm.

The effects of shield geometry also change at different B_0 field strengths, as shown in Figure II-9 and Figure II-10 for tissue with 7T muscle dielectric properties at 3 T. As with the lighter dielectric load at 7 T, greater spacing to the shield was required to discern peak coil efficiency. For imaging this load at 3 T, efficiency peaks when the coplanar shield is spaced about 18 mm from the mean coil diameter, with wider shield widths providing diminishing improvements. The improvement in power efficiency is less profound but still significant. Employing a coplanar shield at 3 T also improves SNR and E-field losses as compared to an unshielded coil. Although expected to be low given the high-dielectric phantom, results suggest radiative losses are not a paramount concern at 3 T, as efficiency from the unshielded coil was merely 0.10% as compared to 0.35% at 7 T.

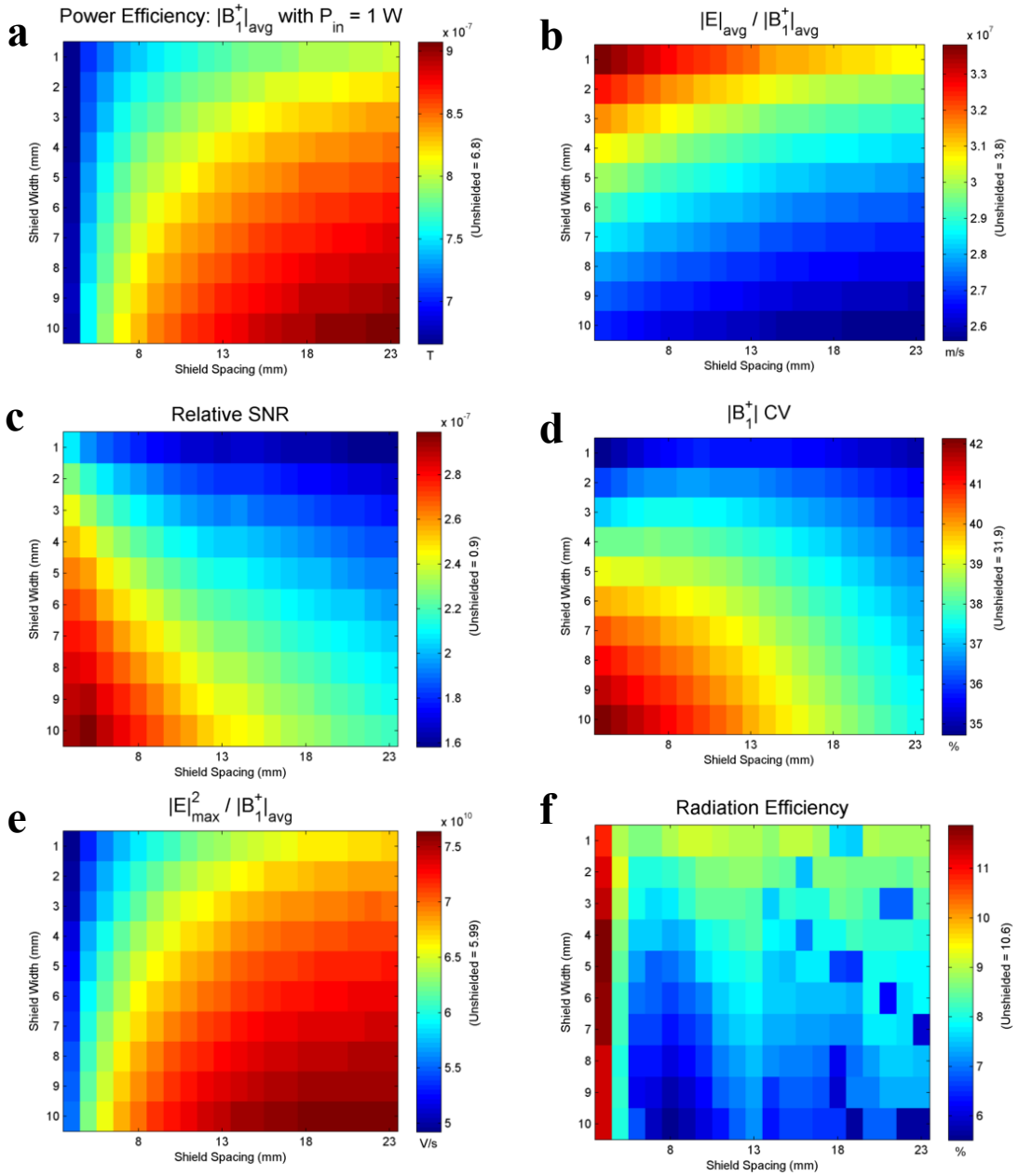

Figure II-7. Color-weighted simulation results for a single 16-cm loop PCB surface coil loaded with adipose tissue at 7 T. (**a**) $|\mathbf{B}_1^+|$ transmit efficiency peaks with > 23-mm spacing and wider shield widths. (**b**) The average *E* field reduces with greater shield widths. (**c**) SNR improves with closer shield spacing and greater shield widths. (**d**) The $|\mathbf{B}_1^+|$ coefficients of variation suggest wider shield geometries with shorter spacing result in greater inhomogeneity; all shielded cases are somewhat more inhomogeneous. (**e**) The indicator of peak local SAR suggests greater shield spacing and width results in higher SAR. (**f**) Radiation efficiency is reduced by up to half with most shielding geometries.

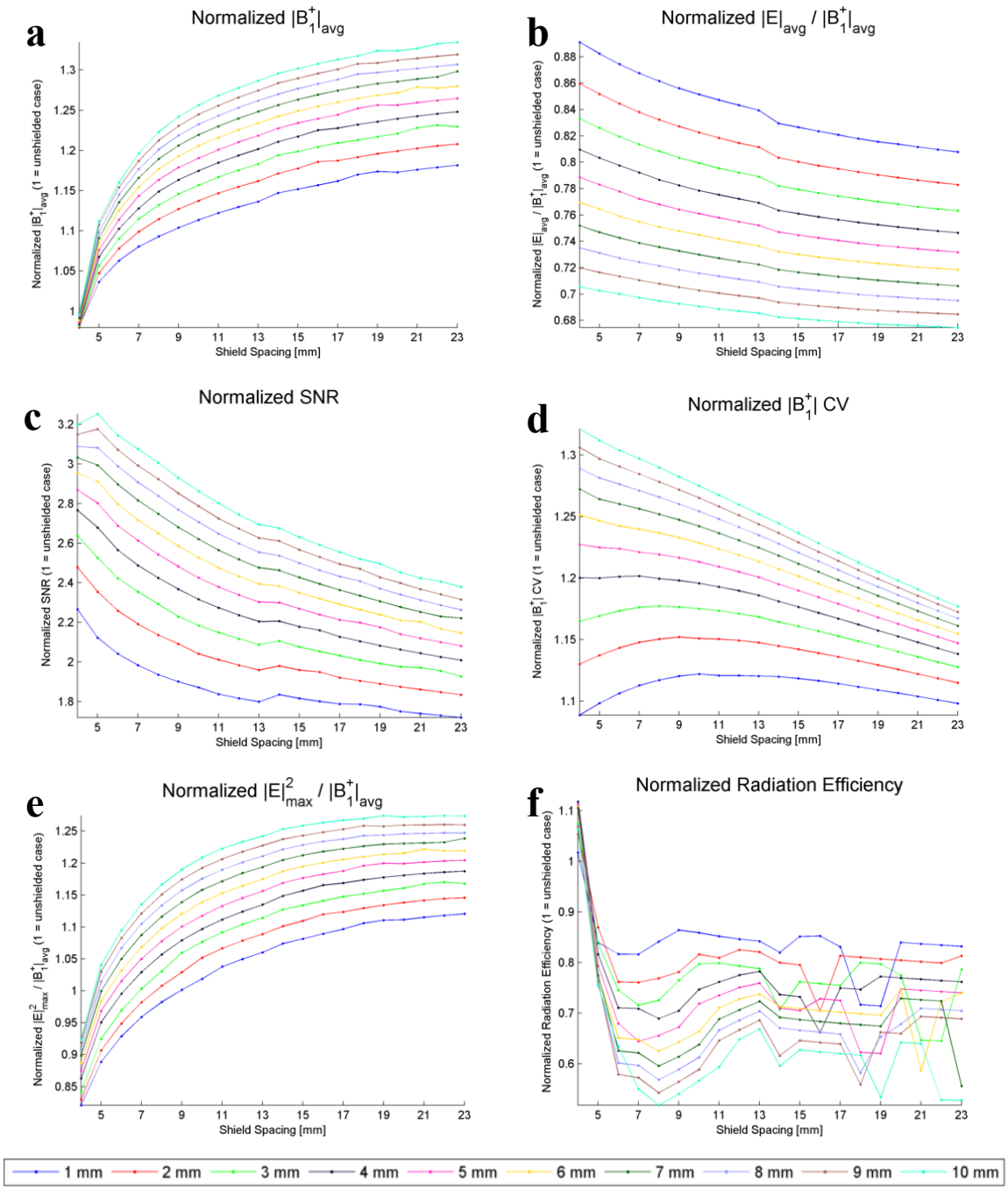

Figure II-8. Normalized line plots (unshielded coil = 1) corresponding to Figure II-7 for a single 16-cm loop PCB surface coil loaded with adipose tissue at 7 T. The legend at bottom identifies plot colors for each shield width.

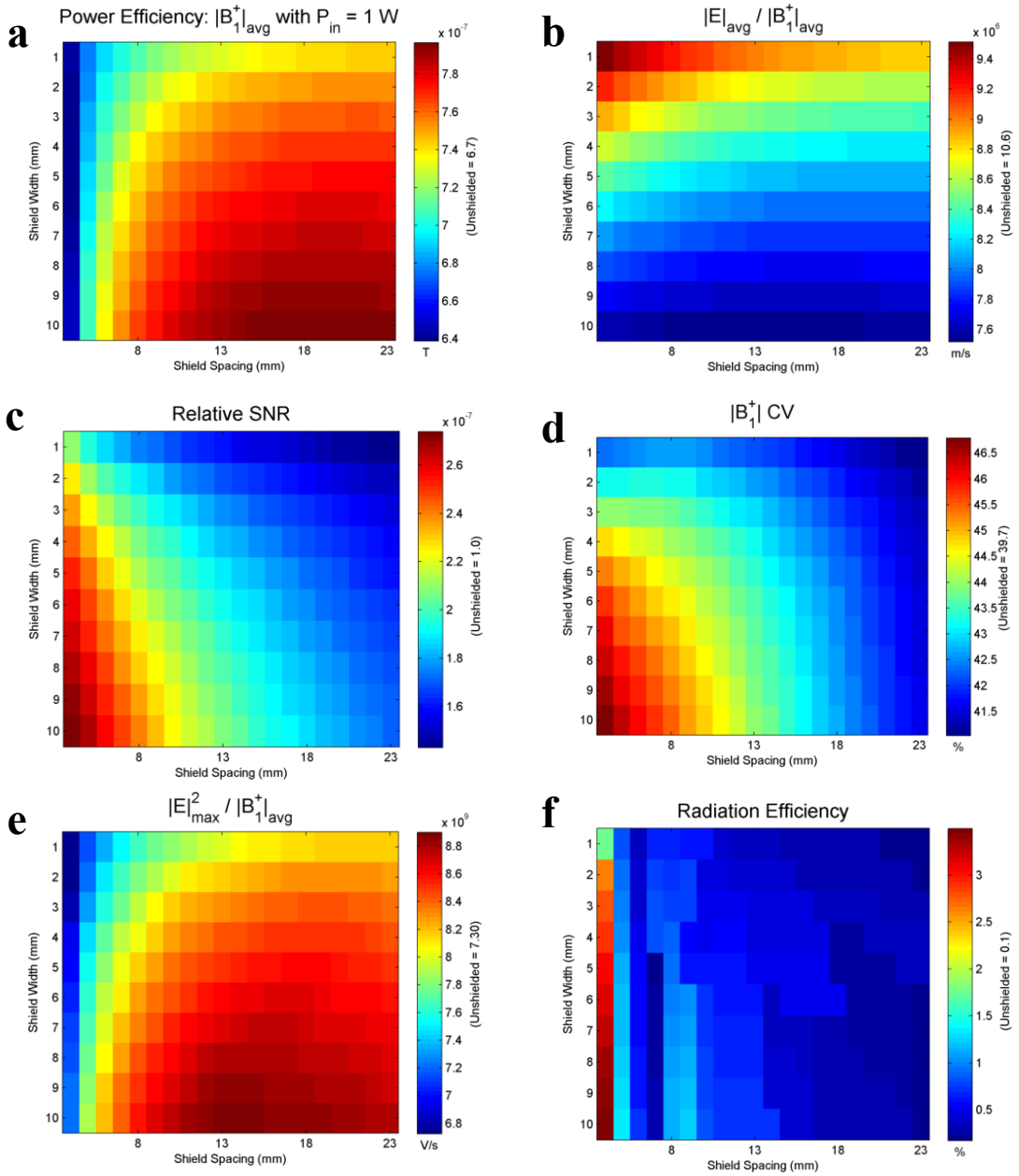

Figure II-9. Color-weighted simulation results for a single 16-cm loop PCB surface coil loaded with muscle at 3 T. (**a**) $|\mathbf{B}_1^+|$ transmit efficiency peaks at 18-mm spacing and wider shield widths. (**b**) The average *E* field reduces with greater shield widths. (**c**) SNR improves with closer shield spacing and greater shield widths. (**d**) The coefficients of variation suggest regions with higher average SNR also have marginally worse $|\mathbf{B}_1^+|$ homogeneity. (**e**) The indicator of peak local SAR suggests a worst case with 14-mm spacing. (**f**) Radiation efficiency is insignificant with a large high-dielectric load at 3 T.

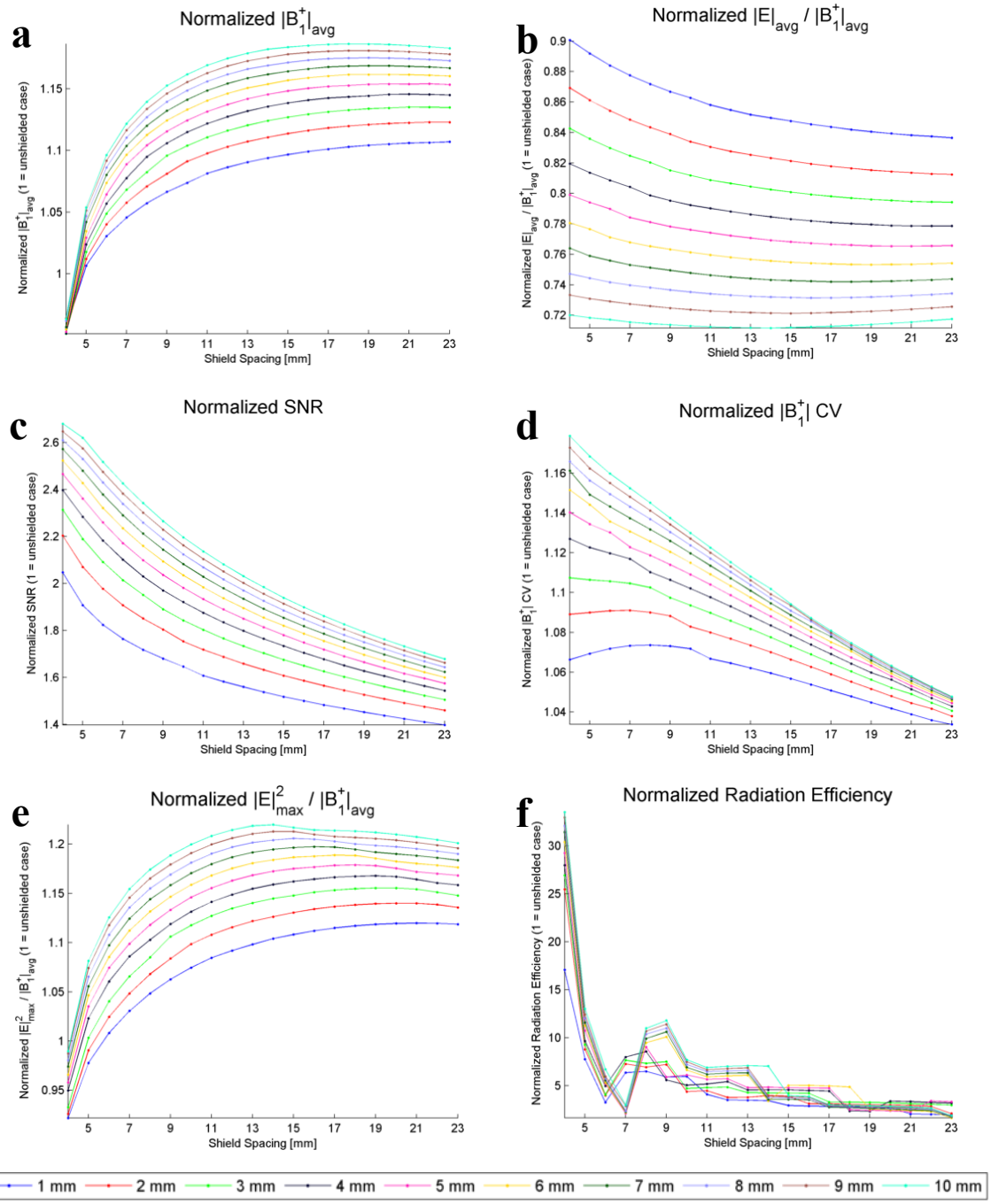

Figure II-10. Normalized line plots (unshielded coil = 1) corresponding to Figure II-9 for a single 16-cm loop PCB surface coil loaded with muscle at 3 T. The legend at bottom identifies plot colors for each shield width.

The FDTD model of the coplanar-shielded loop coil was validated against results from in-house full-wave spectral-domain analysis code. An 8-cm loop coil with a 5-mm wide coplanar shield with 94-mm inner diameter was loaded by the rectangular saline phantom. The two models produced B_1 field patterns and input impedances in close agreement, with the in-house code calculating Z_{in} = 9.7 - j 64.6 Ω and FDTD determining Z_{in} = 9.8 - j 76.9 Ω. Furthermore, on-axis $|\mathbf{B}_1^+|$ values and relative field patterns corresponded well as illustrated in Figure II-11.

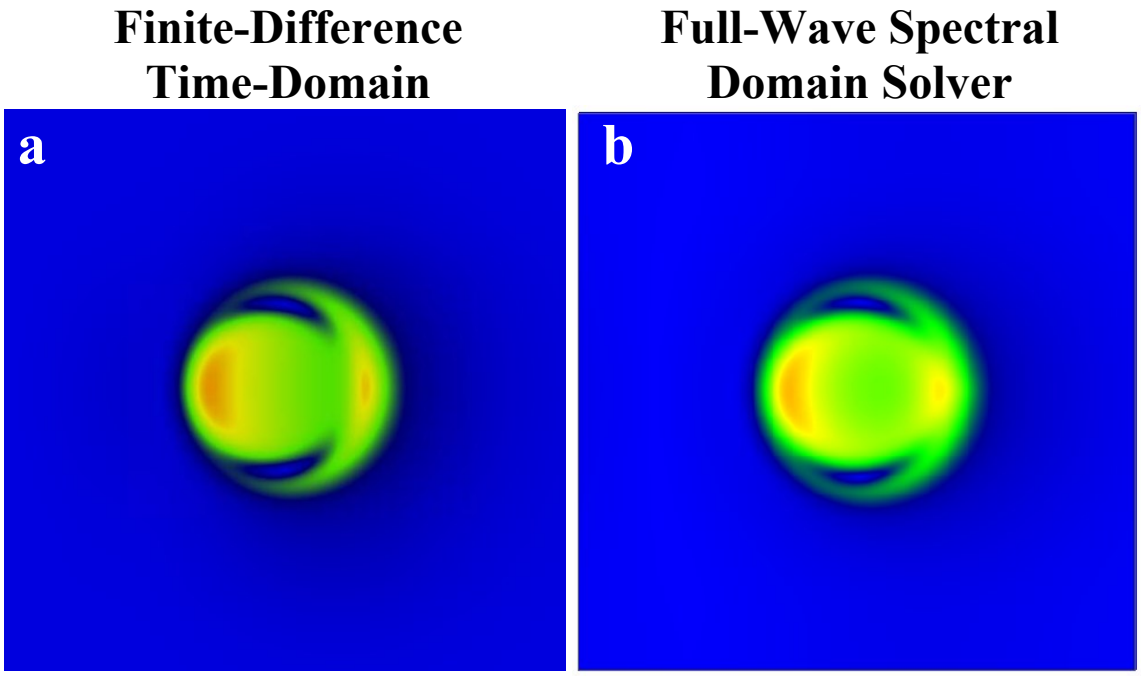

Figure II-11. Comparison of relative $|\mathbf{B}_1^+|$ field patterns 1 mm within the muscle phantom at 7 T using FDTD and in-house full-wave spectral domain solvers.

II.4.2 Radiofrequency Coils

II.4.2.1 Circular Loop Surface Coil

As shown in Table II-1, the coplanar shielded configuration of the 16-cm surface coil exhibited a higher loaded *Q*-factor (Q_l) as compared to the unshielded and ground plane shielded cases. The lower unloaded *Q*-factor (Q_{ul}) for the coplanar shielded case indicates greater coils losses owing to inductive coupling to the shielding conductor, yet the reduced tissue losses owing to an improvement in filling factor results in an improved Q_l compared to the alternative schemes. The unloaded-to-loaded *Q* ratios (Q_{ul}/Q_l) greater than two for all cases indicate losses from the sample dominate, as desired, in the loaded case. Given the higher Q_l for the coplanar shielded coil, the power required to achieve a given B_1 with this load is expected to be roughly a quarter less than required with the unshielded coil.

Also noteworthy were the frequency shifts between the loaded and unloaded cases, recorded before adjusting the tuning capacitor. The observed shifts were 14, 8, and 0.8 MHz for the unshielded, ground plane shielded, and coplanar shielded coils, respectively. The greatly reduced load-dependent tuning shift of the coplanar shielded coil offers a considerable advantage when utilizing a loop coil on different anatomies with variable loading effects.

Table II-1. Loaded and unloaded *Q*-factors from bench measurements comparing unshielded, coplanar shielded, and ground plane shielded versions of the 16-cm surface coil.

Configuration	Q_l	Q_{ul}	Q_{ul}/Q_l
Unshielded	9.2	100	11
Coplanar shielded	13	80	6.3
Ground plane shielded	9.5	110	11

II.4.2.2 Receive Array

Elements from the shielded and unshielded arrays exhibited loaded *Q*-factors of up to 28 and 8.1, respectively. The magnitude of these values are in close agreement with the simulated *Q*-factors of 31 and 9.4. Furthermore, the resulting shielded-to-unshielded *Q* ratios are within 5% when comparing bench measurements and simulations. Together, these data support the validation of simulation results with and without coplanar shields.

As an indication of improved parallel performance, the noise correlation matrices presented in Table II-2 and Figure II-12 reveal the shielded array exhibited 28% lower mean and 22% lower maximum noise correlation in comparison to the unshielded array. With phantom imaging at 7 T, the shielded array provided a 23% improvement in mean SNR throughout the top half (7-cm depth) of the cylindrical phantom. Figure II-13 displays SNR maps for the two arrays on an axial slice through the phantom.

Table II-2. Noise correlation matrices and mean non-diagonal values from the unshielded and coplanar-shielded arrays.

Unshielded Array: Mean = 4.62%				
100%	3.58%	3.60%	4.21%	3.25%
3.58%	100%	5.81%	3.97%	7.14%
3.60%	5.81%	100%	5.46%	4.39%
4.21%	3.97%	5.46%	100 %	4.81%
3.25%	7.14%	4.39%	4.81%	100%

Shielded Array: Mean = 3.34%				
100%	3.02%	3.24%	3.66%	3.69%
3.02%	100%	3.82%	2.66%	5.55%
3.24%	3.82%	100%	1.77%	2.75%
3.66%	2.66%	1.77%	100%	3.25%
3.69%	5.55%	2.75%	3.25%	100%

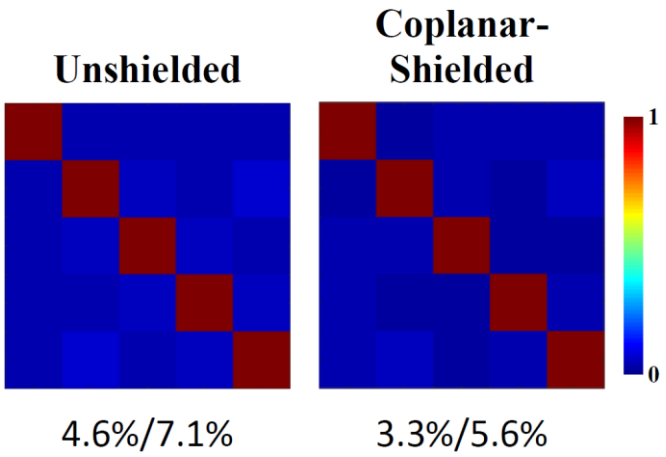

Figure II-12. The noise correlation matrices and mean/max values from the unshielded and coplanar-shielded arrays. Both matrices demonstrate sufficient decoupling between elements; still, the shielded array achieved a 27% and 22% reduction of average and maximum noise correlation, respectively.

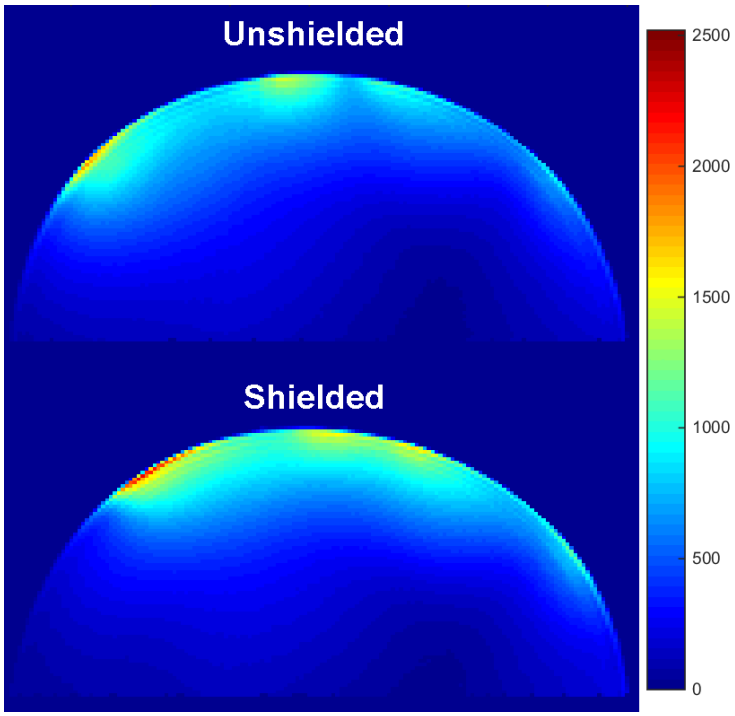

Figure II-13. A comparison of SNR maps in the axial view for the unshielded (top) and shielded (bottom) arrays. The shielded array provided a 23% improvement in mean SNR throughout the top half (7-cm depth) of the phantom.

Results from SENSE-accelerated imaging indicate the arrays perform similarly at lower bidirectional reduction factors and $R = 2$ in the phase-encoding direction (RL). However, with threefold reduction ($R = 3$) in the RL direction the coplanar-shielded array dramatically outperformed the unshielded array, with 64% and 85% the unshielded max and mean *g*-factors. Notably, at bidirectional $R = 6$ the shielded array exhibited a mean *g*-factor of 1.19, within the regime ($g < 1.2$) considered to be favorable for accelerated imaging (68). The *g*-factor maps for both arrays on the coronal plane at 7-cm depth in the phantom are shown in Figure II-14. The visible aliasing in the phase-encoding direction is typical when approaching functional limits of the reduction factor, indicating the quality of reconstruction from individual coil sensitivity maps is beginning to break down.

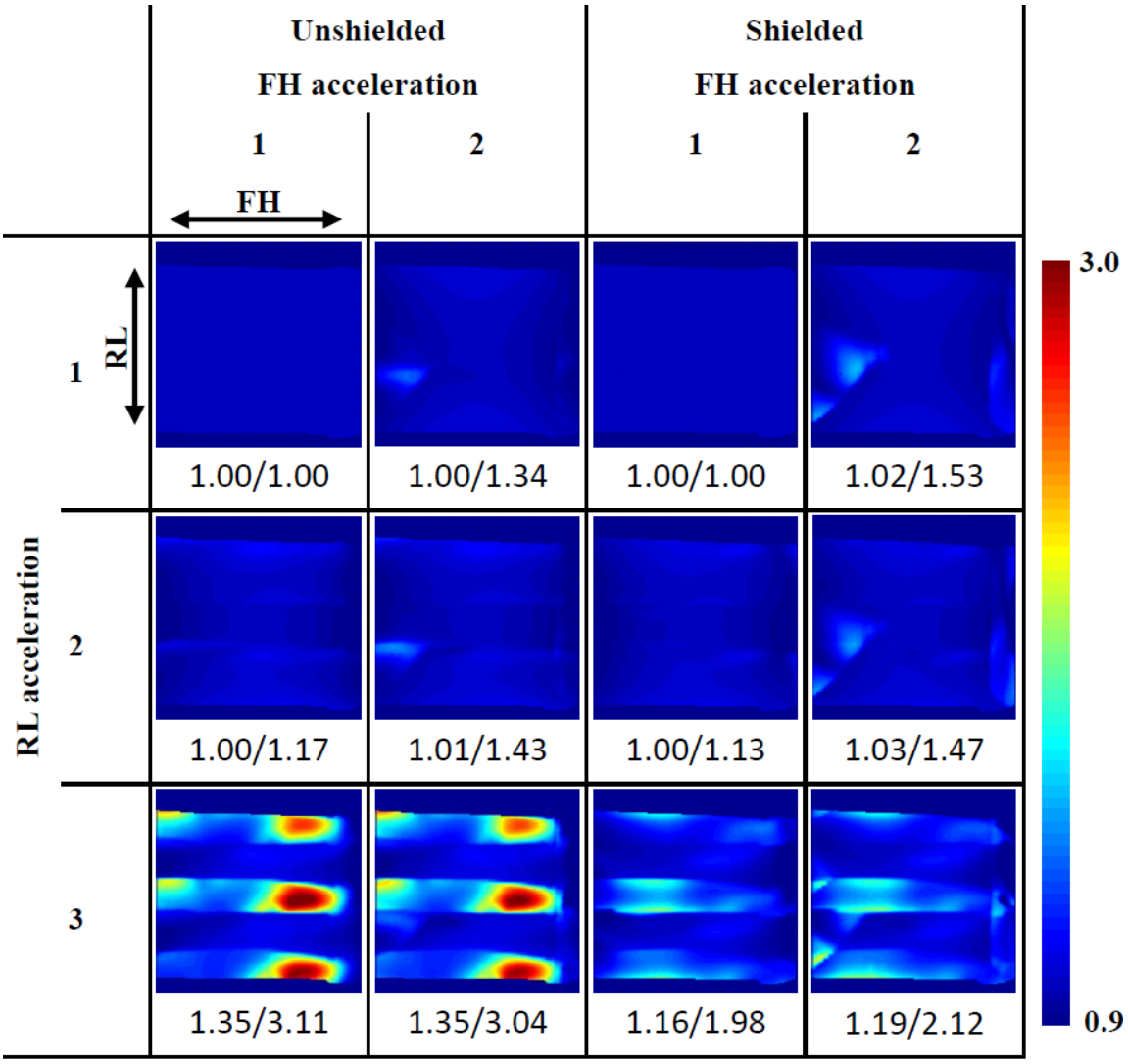

Figure II-14. *g*-Factor maps from bidirectional SENSE-accelerated scans with up to six-fold reduction factor. SENSE was applied in the right/left (RL, phase encoding) and feet/head (FH, frequency encoding) directions with reduction factors of up to $R = 3$ and $R = 2$, respectively. The mean and maximum *g*-factors are displayed below each individual map. The shielded array exhibits significantly lower *g*-factors with three-fold RL acceleration.

II.5 Discussion

Coplanar shields have been shown to improve Q and $|\mathbf{B}_1^+|$ power efficiency for transmit coils. Simulation results establish clear guidelines for maximizing transmit power efficiency. Furthermore, a wavelength dependence is evident in these guidelines. For the example of saline loading, transmit efficiency peaks with shield spacing of 18 mm and 8 mm at 3 T and 7 T, respectively. The ratio of these distances is within 4% the ratio of B_0 field strengths.

Improvements were also demonstrated in a five-element receive array of overlapped elements. By compressing the near-zone B_1 field, coplanar shielding reduces inductive coupling through $\mathbf{B}_1^-$ flux linkage. Despite the high-dielectric properties of the saline phantom, 7T imaging verified the coplanar shields improved SNR and inter-element isolation in conventional parallel imaging. Furthermore, while it has been shown that non-overlapped elements improve SNR in SENSE imaging by means of higher g-factors, despite additional coupling and basic noise (69), coplanar shielding recoups some of the reported performance deficits of overlapped elements, all the while maintaining an array's ability to maximize SNR through conventional parallel imaging. This benefit for overlapped elements is expected to increase with a lower-dielectric load, as the comparative field confinement effects of the shielded elements become more palpable.

Shield optimization with respect to other performance metrics is not as straightforward. As expected, results are dependent on composition of the load and B_0 field strength. In general, most coplanar shield implementations improve SNR while reducing radiation and average E field losses in the sample. $|\mathbf{B}_1^+|$ homogeneity throughout

the ROI is not significantly altered, yet shielding created a slight reduction in most cases. This result can be explained by the definition of the ROI extending outward to the radius of the coil conductor; a smaller ROI would be expected to exhibit improved homogeneity. At high fields, radiative losses are already insignificant when the coil is loaded with a large, high-dielectric sample; indeed, the dielectric sample itself furnishes a shielding effect with respect to radiation. Conversely, radiative loss is appreciable with a lower-dielectric sample such as adipose tissue; the unshielded 16-cm loop was projected to radiate 10% its net input power. In these cases with lighter dielectrics, a coplanar shield can considerably reduce radiative loss. Unfortunately, the field confinement present with coplanar shields also moderately increases peak local SAR, in agreement with results reported with other circumferential shield geometries (44).

During coil construction on the bench, the effects of adding a coplanar shield may be evaluated quickly by comparing *Q*-factors with and without a copper tape prototype. More precise coil construction is easily accomplished by etching copper-clad laminate. In this study, the parameterization capabilities inherent in most full-wave electromagnetic solvers have been shown to provide powerful guidance for fine tuning the shield geometry. Moreover, the modeling procedures presented here may be applied to evaluate other types of shielding and coil geometries.

CHAPTER III

QUADRATURE TRANSMIT COIL FOR BREAST IMAGING AT 7 TESLA USING FORCED CURRENT EXCITATION FOR IMPROVED HOMOGENEITY*

III.1 Synopsis

III.1.1 Purpose

To demonstrate the use of forced current excitation (FCE) to create homogeneous excitation of the breast at 7 tesla, insensitive to the effects of asymmetries in the electrical environment.

III.1.2 Materials and Methods

FCE was implemented on two breast coils: one for quadrature ^{1}H imaging and one for proton-decoupled ^{13}C spectroscopy. Both were a Helmholtz-saddle combination, with the saddle tuned to 298 MHz for imaging and 75 MHz for spectroscopy. Bench measurements were acquired to demonstrate the ability to force equal currents on elements in the presence of asymmetric loading to improve homogeneity. Modeling and temperature measurements were conducted per safety protocol. B_1 mapping, imaging, and proton-decoupled ^{13}C spectroscopy were demonstrated in vivo.

---

*Reprinted with permission from McDougall MP, Cheshkov S, Rispoli J, Malloy C, Dimitrov I, Wright SM. Quadrature transmit coil for breast imaging at 7 tesla using forced current excitation for improved homogeneity. J Magn Reson Imaging 2014;40:1165-1173. Copyright 2014 by Wiley Periodicals, Inc.

III.1.3 Results

Using FCE to ensure balanced currents on elements enabled straightforward tuning and maintaining of isolation between quadrature elements of the coil. Modeling and bench measurements confirmed homogeneity of the field, which resulted in images with excellent fat suppression and in broadband proton-decoupled carbon-13 spectra.

III.1.4 Conclusion

FCE is a straightforward approach to ensure equal currents on multiple coil elements and a homogeneous excitation field, insensitive to the effects of asymmetries in the electrical environment. This enabled effective breast imaging and proton-decoupled carbon-13 spectroscopy at 7 T.

III.2 Introduction

Diagnostic breast MRI at 1.5 tesla and 3 T offers high resolution morphological delineation and tissue contrast, diffusion, and perfusion functional imaging, and assessment of tissue metabolic composition with MR spectroscopy (26,70-77). A new generation of MR studies of the breast may be afforded by the improved sensitivity and chemical shift dispersion provided by the recent availability of commercial whole-body 7T scanners. The technical challenges at 7 T are significant compared with lower field strengths, however, including an increase in B_1 inhomogeneity, specific absorption rate (SAR), and an increased sensitivity of coils to loading. One approach for addressing these issues is to drive multiple transmit coils using multiple independent amplifiers, i.e., B_1 shimming (78,79) or Transmit SENSE (80,81). These are expensive and complex approaches that may not be available for routine clinical research for some time but may

be essential for optimal head and body imaging. Such approaches, however, may not be necessary to effectively image isolated anatomies. For instance, high quality images of smaller structures such as the knee (82,83) have been obtained at 7 T using a single transmit channel. The breast presents a more challenging anatomy to image at 7 T, however, because of its proximity to the thorax that brings about a significantly asymmetric influence on B_1 in the breast. This study presents an RF coil design that overcomes this issue by using transmission line techniques to force equal currents on multiple elements to generate homogeneous quadrature excitation of the breast at 7 T using a single transmitter.

Transmission line techniques to ensure equal currents on array elements with different impedances were introduced more than 50 years ago for broadcast antennas (84,85). The method, termed forced current excitation (FCE), has been investigated previously for use with MRI for mitigating coupling in high channel count arrays of microcoils (86) but the technique has not been applied to coils intended for in vivo use. Here we report the development and application of the FCE design to overcome the effects at 7 tesla of the asymmetric loading conditions present when imaging the breast. By forcing equal currents on the elements of a coil, two main benefits were realized: (i) B_1 homogeneity was achieved without the need for multiple transmitters, and (ii) the robustness provided by maintaining equal currents on multiple elements in the face of highly varying and asymmetric loads enabled tuning and maintaining of isolation between quadrature elements. The load-insensitive homogeneity and efficiency of the quadrature design make the coil particularly well suited for the straightforward addition of a receive

array insert, for performing localized ^{1}H spectroscopy, and for serving as the transmitter for the broadband ^{1}H decoupling often used in non-proton spectroscopy. This study discusses the theory of forced current excitation, the design and construction of the FCE quadrature breast coil for 7 T, and demonstrates the effectiveness of the design with in vivo imaging and broadband decoupled ^{13}C spectroscopy.

III.3 Theory

III.3.1 Effects of Asymmetric Loading as a Function of Field Strength

MR imaging of the breast is typically performed with the patient in a prone position and the breast pendant to avoid respiratory artifacts and improve image quality (74,76). Therefore, solenoidal coils and Helmholtz pairs historically have proven to be effective RF coil designs for breast imaging at 1.5 T and 3 T, generating a volume of homogeneous vertically directed field in the pendant breast with effective penetration into the chest wall (76,87-93). At 298 MHz (7 T), however, the unequal loading between the top of the coil near the thorax and the lower part of the coil away from the body results in a unequal currents on the loops of the Helmholtz pair and thus inhomogeneous excitation. This is illustrated in

Figure III-1 by the modeled comparison of a conventionally driven Helmholtz pair (two 16-cm loops with 8-cm coaxial spacing) exciting an asymmetric phantom at 1.5 T, 3 T, and 7 T. The phantom was designed to mimic the breast and thorax and will be discussed in more detail below. The notable point at 7 T as opposed to 1.5 T or 3 T is the 6-dB drop in sensitivity from the bottom of the “breast” to where it meets the “thorax.” Generating

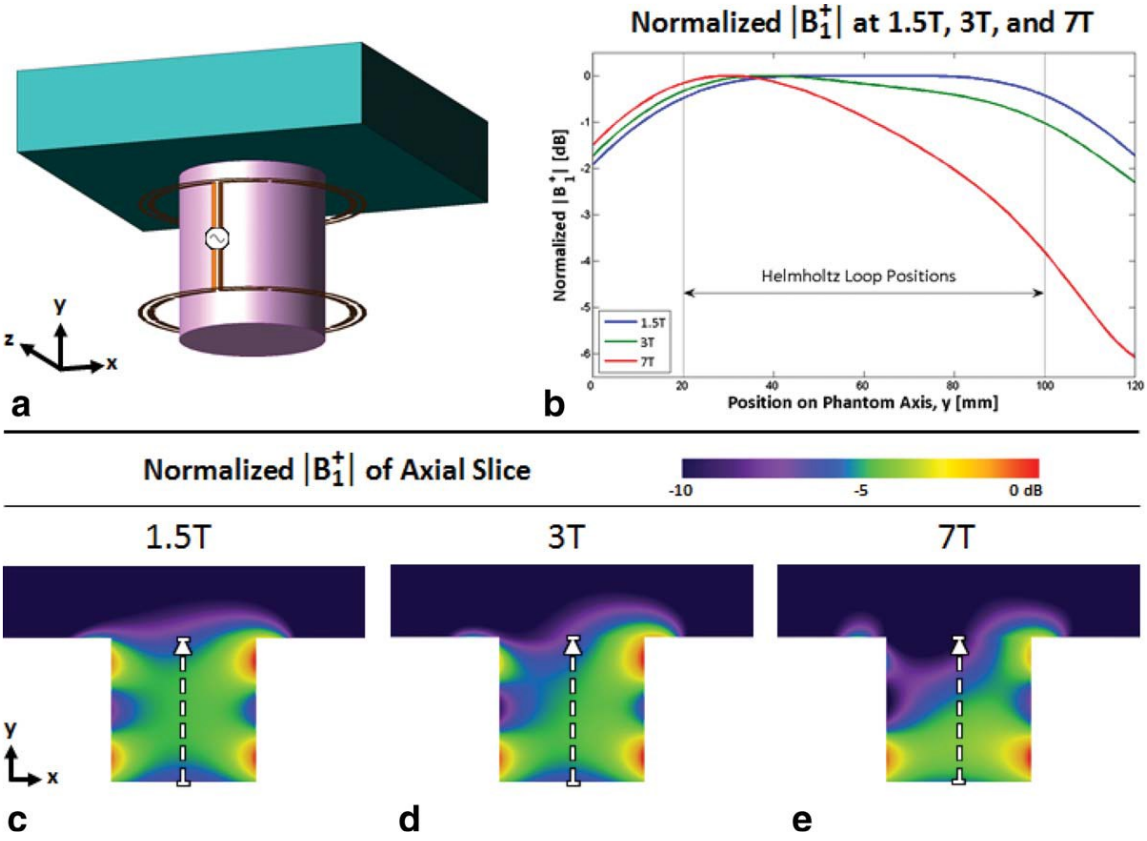

Figure III-1. Comparison of modeled $|\mathbf{B}_1^+|$ as a function of field strength produced by a Helmholtz coil with an asymmetric load that mimics imaging the pendant breast proximal to the thorax. (**a**) Rendering of the conventional, parallel-fed Helmholtz coil with an asymmetric phantom comprised of the electrical characteristics of breast tissue inside and the thorax above. (**b**) Profiles through the marked areas in (**c–e**) depicting $|\mathbf{B}_1^+|$ at 1.5T (63.9 MHz), 3.0T (128 MHz), and 7.0T (298 MHz). The effects of the asymmetric loading of the thorax on the current distribution on the two loops of the Helmholtz coil increases with frequency, resulting in a 6 dB fall off toward the thorax at 7.0 T.

equal currents on the two loops of the Helmholtz pair would in turn ensure a homogeneous field, but can be complex to implement. One approach would be to use a multiple channel transmitter with independent control of each amplifier. Coupling between elements is a complicating factor, but even this can be overcome in principle by using some form of current source amplifier (94-96). Lacking multiple transmit channels, one could design

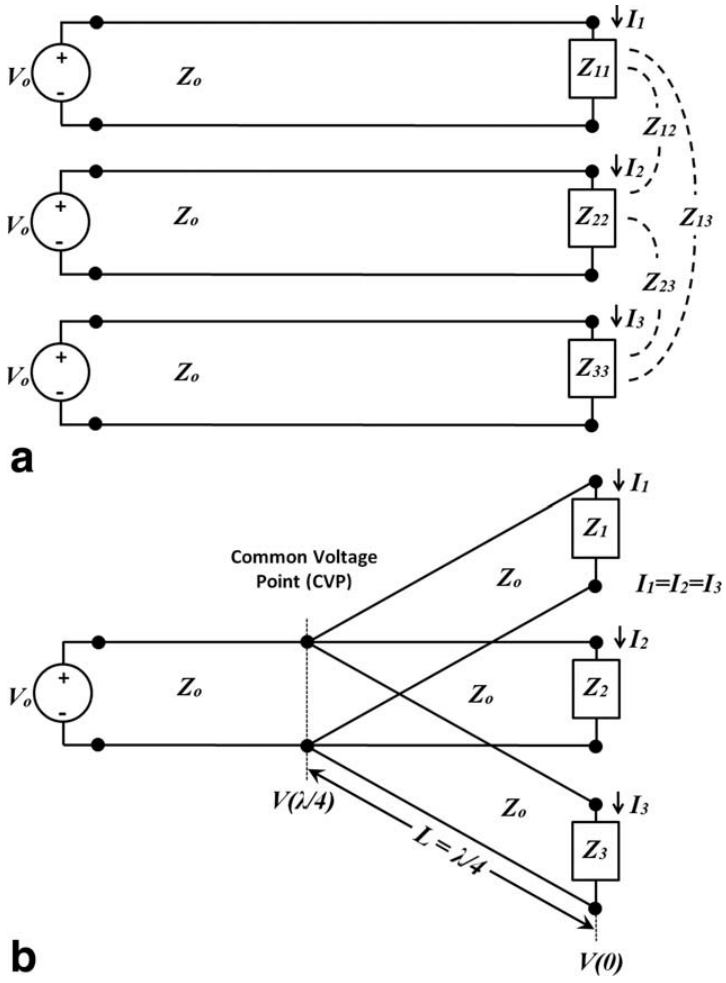

Figure III-2. Comparison of free excitation and forced current excitation (FCE). (**a**) Schematic illustration of three coils, identical or nonidentical, excited by the same voltage. This configuration is termed "free excitation." Asymmetries in positioning or environment, combined with the mutual impedances between coils generally leads to unequal load impedances presented to the sources, resulting in unequal currents despite identical excitation. (**b**) When connected to a common voltage point (CVP) by electrical quarter wave lines the feed currents are the same regardless of differences in the load impedances, effectively achieving "forced current excitation."

some form of tuning network to create equal currents on each element. Theoretically, this could be accomplished using current probes on each loop to provide feedback for independent tuning of the top and bottom loop in the presence of the asymmetric loading—

a complex approach not practical for use with patients. This study describes a specialized power splitter which enforces equal current, rather than equal power, at the feedpoints of the two loops independent of the loading conditions on either loop, thus generating a homogeneous excitation. We refer to this method as forced current excitation (FCE).

III.3.2 Forced Current Excitation

Conventionally, RF coils are driven in a "free-excitation" model, where a voltage source is controlled, and the current in the elements becomes dependent on the load impedance, as illustrated in Figure III-2a. However, as a consequence of asymmetries introduced by the specific anatomy (such as the thorax) as well as the electrical environment from tuning elements, receive coils, etc., the impedance presented to the voltage source will vary with its loading, as well as with the loading in the adjacent elements. The effects of asymmetric loading in a free excitation model as a function of field strength were demonstrated in the previous section, and are particularly prevalent at 7 tesla. To avoid this, FCE can be created, in which the current at the element feed ports can be made independent of the load impedance. This is illustrated in Figure III-2b, where the individual RF elements share a common feed port at an electrical distance of λ/4. Transmission line analysis of each feed line to any of the loads relates the voltage on the transmission line, the load impedance, and the load current as:

$$V(z) = \frac{I_{\mathrm{L}}}{2}\left[(Z_{\mathrm{L}} + Z_0)e^{+j\beta z} + (Z_{\mathrm{L}} - Z_0)e^{-j\beta z}\right] \qquad [\mathrm{II}.1]$$

where β is the propagation constant in the transmission line, z is the physical distance measured from the load, Z_{L} is the active impedance of the array element (which is generally different than its isolated input impedance), Z_0 is the characteristic impedance

of the transmission line, $V(z)$ is the voltage and I_L is the load current. In the special case where the transmission lines connecting the element feed points to a common voltage point are an electrical quarter wavelength (as shown in Figure III-2b), Eq. [II.1] simplifies to:

$$V\left(\frac{\lambda}{4}\right) = \frac{I_L}{2}\left[(Z_L + Z_0)e^{j\frac{\pi}{2}} + (Z_L - Z_0)e^{-j\frac{\pi}{2}}\right]. \quad [II.2]$$

After simplifying Eq. [II.2], the impact of the load impedance disappears and it can be shown that the load current depends only on the characteristic impedance of the line and the voltage at the common feed point:

$$I_L = \frac{V\left(\lambda/4\right)}{jZ_0}. \quad [II.3]$$

It should be noted that the voltage at the common voltage point (CVP) is indeed dependent on the load values, as is the actual value of the load current, I_L. What the FCE approach ensures, however, is that all the load currents are the same, regardless of differences in the load values, as long as all the elements are connected to the CVP through electrical quarter wavelength lines. As will be shown below, enforcing equal current at the different RF element ports results in improved B_1^+ homogeneity over free excitation in highly asymmetric loading conditions, as is the case in excitation of the pendant breast. It is worth noting that throughout the text, B_1^+ notation will be used where appropriate to indicate specific reference to properties of the transmitted field, though we operated in transmit–receive mode.

III.4 Methods

III.4.1 Coil Construction

Two coils were constructed which used the forced current technique: one for quadrature ^{1}H imaging and one for proton-decoupled ^{13}C spectroscopy. Henceforth these will be referred to as the "imaging coil" and the "spectroscopy coil," respectively. Both coils consisted of a Helmholtz-saddle combination, with the saddle tuned to 298 MHz for the quadrature imaging coil and tuned to 75 MHz (^{13}C) for the spectroscopy coil.

The Helmholtz component of the imaging coil was constructed from two identical loops (i.d. 16.0 cm; o.d. 17.2 cm; co-axial spacing 8.0 cm) to produce y-directed B_1 field. The saddle coil (diameter 15.3 cm; length 8.7 cm; aperture angle 120°, conductor width 0.6 cm) was constructed from two elements, affixed on opposite sides of a cylindrical former, and centered inside the Helmholtz coil, producing x-directed B_1 field. A dimensioned illustration is shown in Figure III-3a. Both the Helmholtz pair and the saddle pair were FCE-driven, enabling robust and straightforward/insensitive matching and tuning in quadrature due to the enforced equal currents ensuring symmetry. All coil elements were fabricated from industry-standard copper-clad FR-4 PCB and segmented by eleven 12.1 pF capacitors. Each element was also surrounded by a parallel co-planar shield (conductor width 0.4 cm, spaced 0.4 cm from element) segmented in two places with 1800 pF capacitors. FCE was implemented separately for the Helmholtz and saddle coils, with both elements in each coil pair connected to a common voltage point through quarter-wavelength coaxial cables. Traps integrated in the quarter-wavelength cables ensured current suppression on the outside of the coaxial shield. The match and tune circuit

for each coil pair was connected to its common voltage point (CVP) by a length of coaxial cable chosen to facilitate matching to 50 Ω. Two identical coaxial cables with additional integrated traps connected the quadrature coil to the MR system. A photograph of the imaging coil is shown in Figure III-3b, with the relevant cable lengths and components labeled.

The Helmholtz component of the spectroscopy coil consisted of two identical loops (i.d. 14.8 cm; o.d. 16.0 cm; co-axial spacing 7.4 cm) surrounded by a parallel co-planar shield that provided uniform proton decoupling over the volume of the breast when driven with FCE. A conventionally driven, unshielded saddle coil was used for ^{13}C transmission and reception (diameter 13.2 cm; length 8.0 cm; aperture angle 121°; conductor width 0.6 cm).

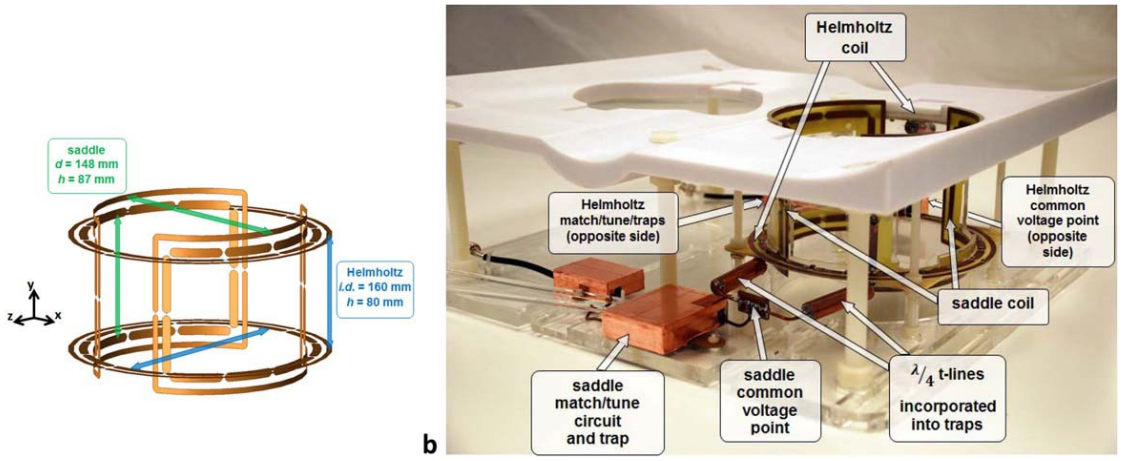

Figure III-3. Rendering and photograph of the quadrature Helmholtz–saddle FCE coil. (**a**) 3D rendering of the coil with gaps for capacitors and dimensions shown. (**b**) Photograph of the completed quadrature coil with important features marked.

III.4.2 Electromagnetic Modeling and Bench Measurements

Commercial FDTD simulation software (XFdtd 7.1, Remcom, State College, PA) was used to perform electromagnetic modeling for determining safe operating parameters. The 5-mm resolution High Fidelity Female Body Mesh provided by NMR Hershey (Center for NMR Research, Pennsylvania State University, College of Medicine at Hershey) and distributed by Remcom was designed with the body in the supine position and therefore was not conducive to filling the interior of the volume coil when in the prone position. Therefore, for SAR evaluation, a geometric phantom was generated consisting of a cylinder with the electrical properties of breast tissue spaced 1 cm inside of the coil conductors. The cylinder was connected to a rectangular region with the properties of muscle to represent the thorax. Electrical properties of the breast and thorax regions of the phantom were obtained from (97), with conductivity $\sigma = 0.04$ S/m and relative permittivity $\varepsilon_r = 5.64$ for breast tissue, and $\sigma = 0.77$ S/m and relative permittivity $\varepsilon_r = 58.2$ for the thorax. The coil volume was discretized on a 1 mm grid and each FCE element was fed with a 50-Ω, 1-A (steady state) current source to simulate the FCE drive condition.

To illustrate the benefits of FCE, bench measurements of field patterns for the 16.0-cm i.d. Helmholtz coil were obtained using an automated three-dimensional (3D) positioning system reported previously (98). Field maps were acquired in an unloaded and in an asymmetrically loaded condition designed to mimic the presence of the thorax. The measurements were then repeated with the coil in a conventionally driven (non-FCE) configuration. To create the asymmetric loading conditions, a rectangular thorax phantom filled with 0.77 S/m saline solution was placed on top of the coil former. In all cases

(unloaded, loaded, FCE, non-FCE), the coils were matched and tuned to 298 MHz and field measurements were acquired as S_{21} measurements (network analyzer HP 4395A) between the Helmholtz and a 4-mm i.d. shielded loop controlled by the automated positioner. It is worth noting that the saddle coil elements are symmetrically loaded by the thorax phantom; thus to illustrate the benefits of FCE, measurements were made on the Helmholtz coil only.

III.4.3 Imaging

All imaging and spectroscopy studies were conducted on a protocol approved by the local institutional review board. After obtaining written informed consent, data were acquired on a whole-body 7T scanner (Achieva, Philips Medical Systems, Cleveland, OH). Surface and volume direct temperature measurements were performed in oil phantoms using Reflex fiber optic temperature measurement system (Neoptix Canada LP) following the Philips-prescribed coil testing protocol to establish coil safety. Specifically, temperature was recorded before, during, and after the heating protocol. We used an RF intensive imaging protocol with 3% RF duty cycle, maximum B_1^+ = 20 μT, and a total scanning time of 10 min. The studies were carried out at room temperature (18-21°C, depending on the particular day of the experiment; temperature variation on a particular day was ±0.1°C), and each phantom was allowed to equilibrate for 10 min before the initiation of the RF heating studies. Temperature was measured both in the oil phantom and near the electrical elements on the coil and demonstrated marginal heating (less than 1°C), within safety guidelines (99).

Imaging was performed using the ^{1}H unilateral quadrature breast coil described above in transmit/receive mode. The subjects were in prone position, with the head resting on pillows and with arms either to the side or above the head. The coil has openings on the sides of the saddle coil elements along the LR direction, which allows for access to the breast, such that the technologist can adjust the positioning of the subject. Each of the FCE coil pairs was tuned and matched per individual volunteer. Studies included the following: (i) B_1^+ mapping using dual repetition time (TR) method acquisition (100) with nominal flip angle of 50 degrees, TR1/TR2 = 35/140 ms, and resolution 2 × 2 × 10 mm, (ii) fat suppressed 3D T1 weighted (THRIVE) sagittal, TR/echo time (TE) = 6.6/2.8 ms, FA=8 degrees, two spatial resolutions—0.8 mm and 0.45 mm isotropic, 1:40 and 5:40 min acquisition, respectively, with SPAIR (Spectral Selection Attenuated Inversion Recovery) fat suppression (101), inversion delay = 150 ms and (iii) 3D T2-weighted imaging (VISTA) with nonselective excitation, no fat suppression, sagittal, TR/TE = 2000/100 ms, TSE factor = 67, field of view (FOV) 250 × 200 × 105 mm, 0.6 × 0.6 × 3.0 mm acquired resolution). Maximum B_1^+ was limited to 20 μT in system software.

III.4.4 Broadband Proton-Decoupled ^{13}C MRS

Localized (ISIS, 50 × 50 × 50 mm) ^{13}C spectra were acquired with the previously described "spectroscopy coil" by averaging 64 acquisitions with TR = 13 s for a total scan time of 14:44 min. The large voxel was selected to compensate for the intrinsically low sensitivity of natural abundance ^{13}C MRS. Because the goal of the study was fat composition analysis, however, the large voxel size did not represent a significant limitation as it would in the case of a lesion study. The repetition time was relatively long

to mitigate SAR issues typical for proton-decoupled ^{13}C MRS. Additionally, this choice benefited the MRS quantification because ^{13}C T1s are relatively long. One offset was used, centered on the CH_2 envelope of the fingerprint region (~29 ppm). WALTZ-16 decoupling with an 18 μT proton pulse centered at 1.3 ppm (for the fingerprint region) and NOE (10 μT at 5% duty cycle and a mixing time of 1.5 s) were used to simplify the spectra and enhance SNR. Scans were acquired with BW = 16 kHz and 2k points. Maximum B_1^+ for ^{13}C was limited to 220 μT in software.

III.5 Results and Discussion

III.5.1 Modeling and Field Mapping

Modeled $|\mathbf{B}_1^+|$ values and SAR maps for the Helmholtz pair and the saddle pair are shown in Figure III-4, as generated by the Remcom XFdtd software in the phantom described above. The axial, sagittal, and coronal views are oriented with respect to the magnet axis (z). All three views are the isocenter plane. The benefit of the FCE approach, enforcing equal currents on the elements of the Helmholtz pair and saddle pair, is evident in the top-bottom symmetry in the SAR and $|\mathbf{B}_1^+|$ maps for the Helmholtz pair and in the left–right symmetry for the saddle pair despite the presence of asymmetric loading conditions. The asymmetries in the SAR modeling indicating increased SAR at the bottom of the saddle pair (seen in the axial modeling) and one side of the Helmholtz pair (seen in the sagittal and coronal modeling) are due to closer proximity to the feed points. Specifically, both elements of the saddle coil were excited on the −y side and both loops of the Helmholtz pair are excited on the +z side.

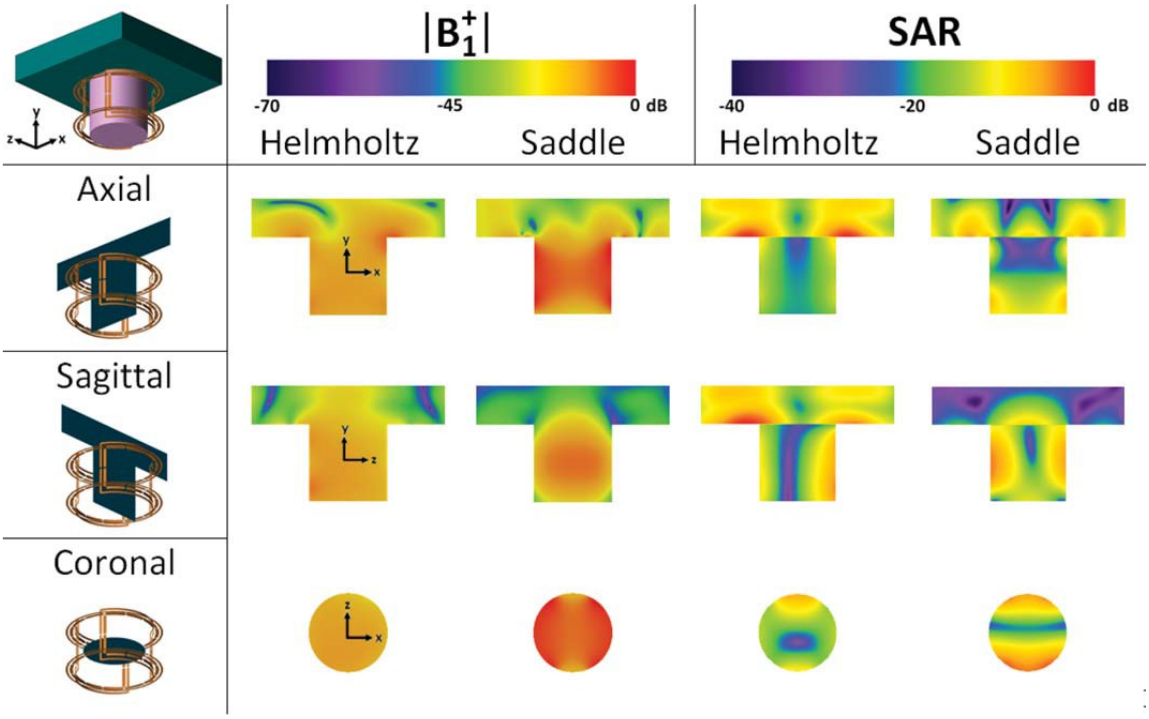

Figure III-4. $|\mathbf{B}_1^+|$ and SAR field plots generated by Remcom XFdtd. The phantom is a 12.0-cm diameter, 12.0-cm tall cylinder with the nominal properties of breast tissue connected to a 30.0 × 30.0 × 6.0 cm slab assigned the properties of muscle tissue, as described in the text. $|\mathbf{B}_1^+|$ plots demonstrate the homogeneity provided by the FCE design despite asymmetric loading. Asymmetries in the SAR plot are due to the feed locations on the Helmholtz and saddle pairs, as described in the text. The Helmholtz and saddle pairs were each normalized to 1 watt net input power. 0 dB corresponds to 2.0 μT and 1.47 W/kg in the $|\mathbf{B}_1^+|$ and SAR figures, respectively.

A comparison of field profiles between unloaded and asymmetrically loaded FCE and conventional Helmholtz coils is shown in Figure III-5, demonstrating the advantage of using FCE. The FCE driven pair created a homogeneous field in both the loaded and unloaded cases, confirming the presence of substantially equal currents on the two loops despite one of the loops being heavily loaded. Conversely, the presence of the heavy loading on one loop of the conventionally driven Helmholtz pair created a 3-dB variation

in the field intensity over the measurement range, in agreement with the electromagnetic modeling results shown in Figure III-1.

It is important to note that there is no difference between the SAR and homogeneity of a conventionally driven coil that is tuned to achieve equal currents on the elements and the FCE coil; the point of the FCE design is the ability to realize the equal currents straightforwardly. Independent tuning of the elements could be quite cumbersome in practice, particularly given that the coupling between the saddle and Helmholtz pairs is not minimized until the current balance is achieved.

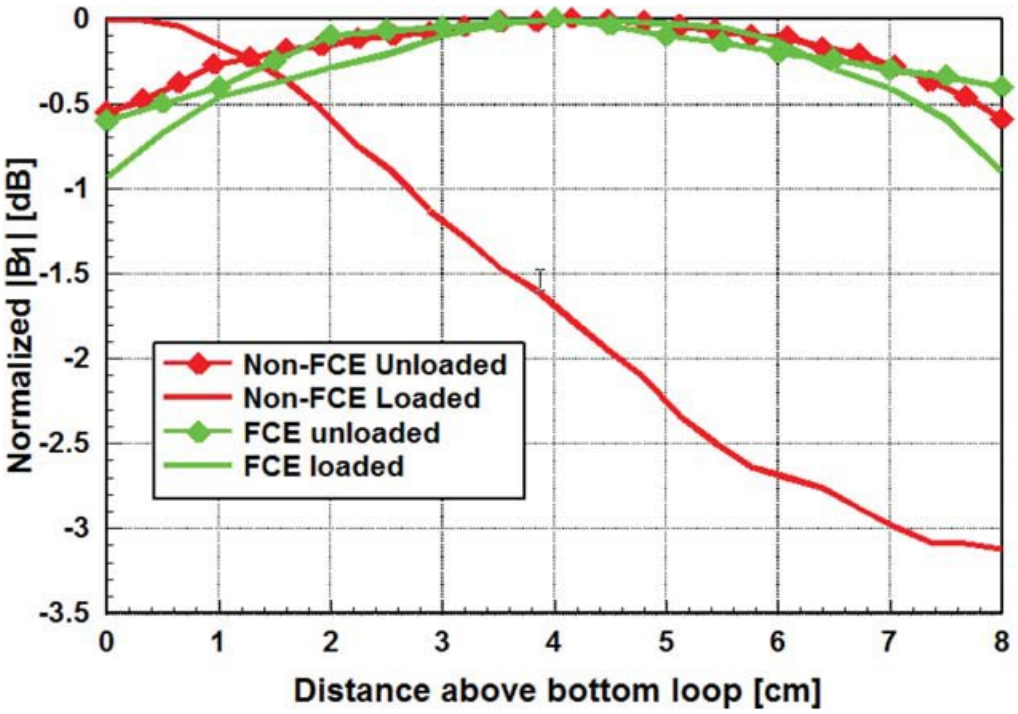

Figure III-5. Measured field profiles obtained as the S_{21} measurement between a shielded pickup loop and the Helmholtz coil in FCE and non-FCE mode, unloaded and asymmetrically loaded. Each profile is normalized to its respective maximum. The FCE maintains excellent homogeneity, comparable to the completely unloaded case, even in the presence of asymmetric loading.

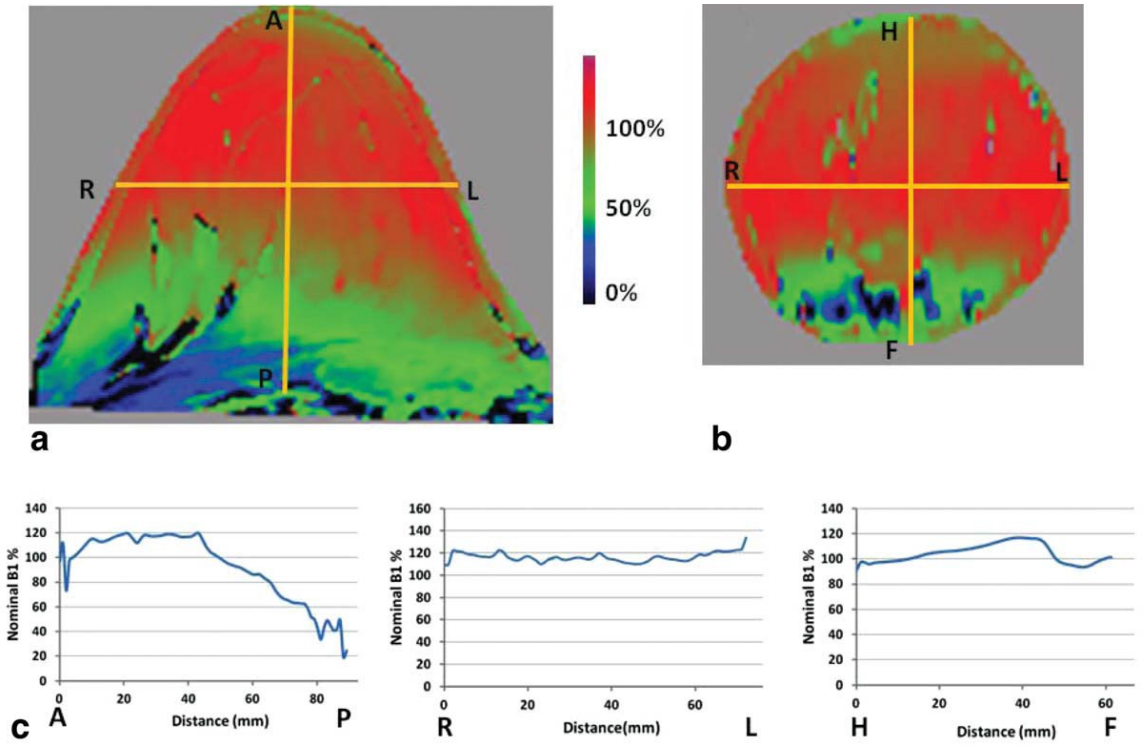

Figure III-6. B_1^+ map of a healthy volunteer. Power optimization was performed on the shim volume that included most of the breast volume proper. The nominal tip angle was 50 degrees and B_1^+ is shown as a percentage of that. (**a**) B_1^+ in the transverse plane as a percentage of nominal B_1^+. (**b**) B_1^+, coronal view. (**c**) B_1^+ AP, RL, and FH line profiles corresponding to the yellow lines in (a) and (b). The AP profile indicates approximately 1 cm penetration into the chest wall. The coefficient of variation of B_1^+ in AP direction in the breast tissue is approximately 20% in this case due to the posterior side of the breast extending outside the coil. The RL and HF profiles exhibit much smaller variations, 4% and 7%, respectively. The location of the HF profile line was chosen specifically to avoid the large anatomical null in the bottom center of the image.

III.5.2 Imaging

A B_1^+ map of a healthy volunteer is shown in Figure III-6. The anterior–posterior (AP) line profile (Figure III-6c) indicates approximately 1cm chest wall penetration. The B_1^+ coefficient of variation in the AP direction in the breast tissue is approximately 20%. The drop off into the chest wall is due to the fact that the breast did not fill the coil in this case.

The anterior side of the breast is in the homogeneous center of the coil and, with coil padding in place for patient comfort and safety, the posterior side extends outside the coil FOV. A larger diameter coil would address this issue, but with the wavelengths associated with 7 T, the benefits of a larger coil will need to be evaluated against the design challenges and potential loss of image quality. As expected, the B_1^+ profiles in the orthogonal directions (right–left [RL] and head–foot [HF] in Figure III-6) show much smaller variations (5–7%).

The first breast images acquired using the FCE quadrature coil are shown in Figure III-7. Three different sets of images are shown in the three columns. Upper and lower rows show adjacent slices. The left column is an isotropic T1W FFE 3D acquisition (voxel size 0.8 mm^3) using SPAIR fat suppression. Quality of the fat suppression is noted as excellent with residual signal being just several times the background noise level. The middle column is the same technique with 0.45 mm^3 voxels. Improved tissue margins are clearly observed on this ultra-high isotropic resolution image, and while its overall SNR is reduced as compared to the image acquired with the more clinically used resolution of 0.8 mm^3, it is still sufficient for clear visualization of the parenchyma. The ability to acquire images of such high resolution may lead to improvements in morphological characterization of tumors and their involvement in the surrounding tissues. The chest wall directly under the coil is also visualized, though with reduced intensity. Insufficient SNR is also noted in the region of the axilla. The right column shows 3D T2W TSE (0.6 × 0.6 × 3 mm^3) without fat suppression. A certain amount of blurring is observed in these T2-w 3D TSE images because this sequence relies on long echo trains that will be affected by

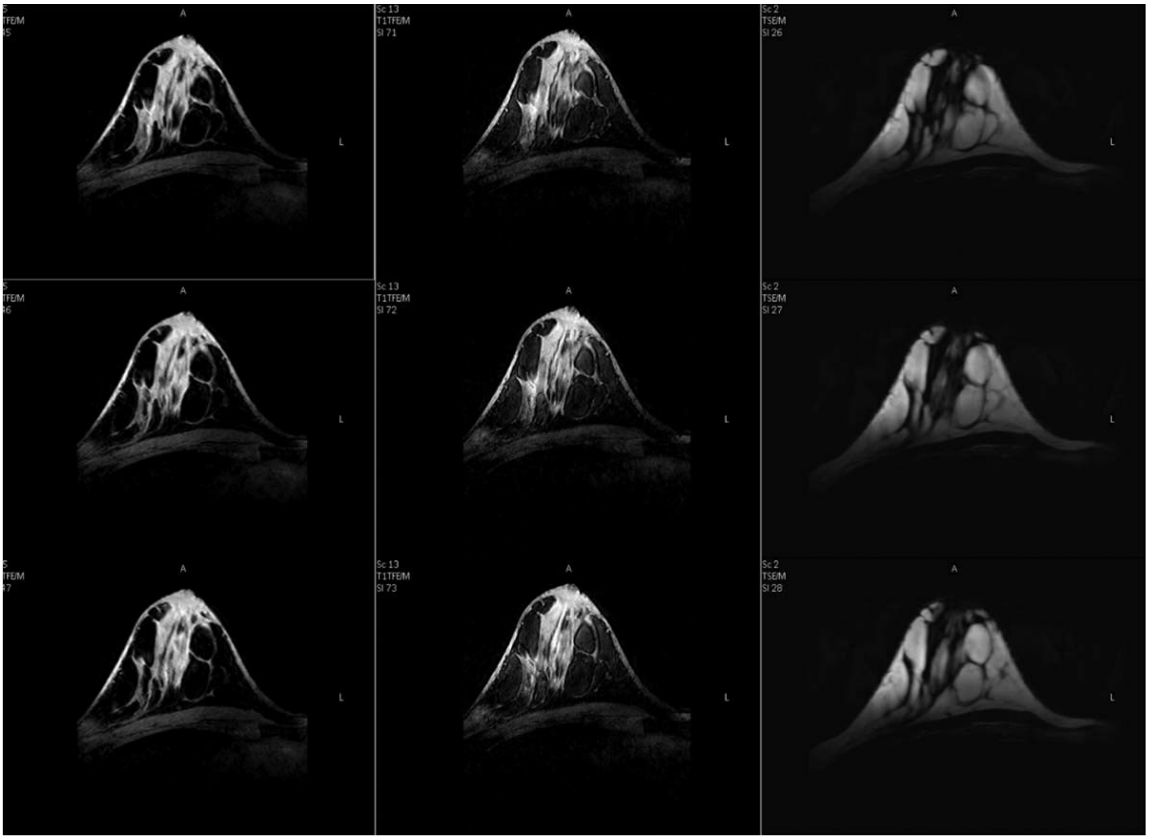

Figure III-7. Breast images using FCE quadrature ^{1}H breast coil. In columns: (left) T1W FFE 3D (0.80 mm^3) with SPAIR fat suppression; (middle) T1W FFE 3D (0.45 mm^3) with SPAIR fat suppression; (right) T2W TSE (VISTA) TSE (0.6 × 0.6 × 3.0 mm^3). Note excellent suppression of the fat signal on T1W images, almost to the background level.

the expected decrease in tissue T2 at 7 T. Modification of the echo train to include varying refocusing angles may alleviate this issue and preliminary work is underway (102).

III.5.3 In Vivo ^{13}C MRS

Broadband proton-decoupled ^{13}C NMR spectrum from the right breast of a normal volunteer is shown in Figure III-8, along with the data fit (in blue). All expected major lipid ^{13}C peaks in the fingerprint region are observed, showing no detectable decoupling artifacts (i.e., sidebands) over the entire acquisition bandwidth. In addition to the three fat

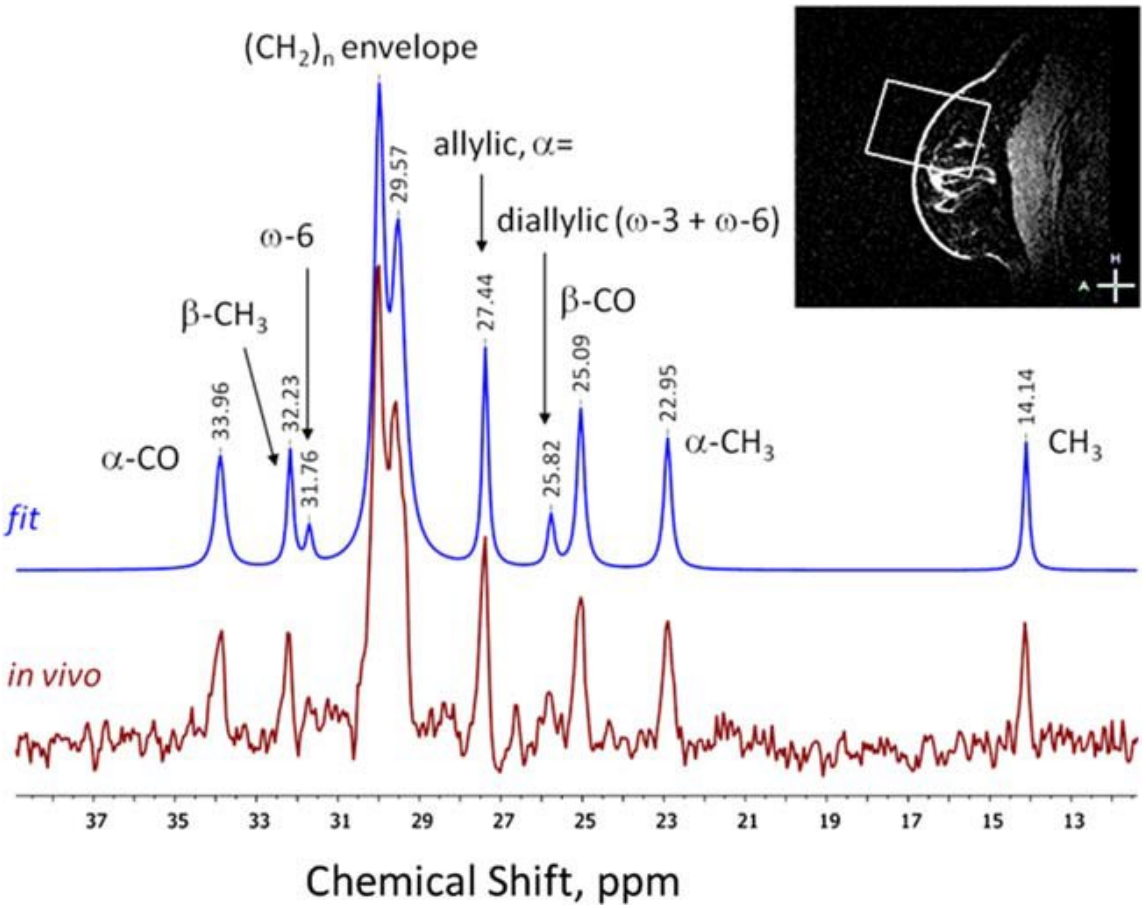

Figure III-8. Broadband proton-decoupled ^{13}C NMR spectrum from a healthy breast. (In this volunteer, the ratio omega-6/omega-3 = 1.94). The white square on the breast image insert represents the ISIS localization voxel.

fractions that can be obtained by means of proton MRS (saturated versus mono-unsaturated versus poly-unsaturated) as shown in Dimitrov et al. (26), fitting the ^{13}C spectrum allows for calculation of omega-6/omega-3 lipid ratio by the ratio of the diallylic (containing both omega-6 and omega-3) peak at 25.82 ppm and the omega-6 peak at 31.76 ppm (103). Further improvements in ^{13}C coil sensitivity will be required to reliably discern these peaks in vivo and to achieve shorter acquisition times, and work is underway in this area.

III.6 Conclusion

Construction and optimization of safe and effective radiofrequency coils at 7 T is a major challenge. The well-known interactions between transmit frequency and tissue dimensions and the increased sensitivity to loading at higher frequencies generate inhomogeneous B_1 fields, degrading image quality. To address these challenges, this work discussed a forced current excitation feed technique applied to a unilateral ^{1}H quadrature volume breast coil and a linear coil for proton-decoupled ^{13}C acquisition. The FCE design used transmission line properties to ensure equal currents at the feedpoints of the elements in a Helmholtz-saddle configuration despite unequal loading on the elements due to asymmetries in the electrical properties of the anatomy, the presence of multiple elements, tuning components, etc. The insensitivity to loading simplified matching and tuning and enabled the elements of the quadrature coil to be easily decoupled. The homogeneity of the coil was demonstrated by achieving images with excellent fat suppression and with the ability to achieve broadband proton decoupling in ^{13}C MRS.

This study has presented an option to provide limited control of currents on array elements to create more homogeneous B_1^+ excitation patterns using a single amplifier. Future work will include improving SNR by adding an array coil insert and optimization of imaging and spectroscopy parameters.

CHAPTER IV

AUTOMATED VOXEL MODEL MODIFICATION FOR HIGH FIELD SAR MODELING OF ANATOMICALLY-DERIVED BREAST PHANTOMS WITH VARYING TISSUE HETEROGENEITY

IV.1 Synopsis

IV.1.1 Purpose

Electromagnetic modeling of the breast to support establishing safe scan protocols is complicated by anatomical variability of fatty and glandular tissues and the associated effects on power deposition. This work presents 7T simulations using a whole-body model integrated with a variety of available breast phantoms spanning the standard four tissue density classifications representing the majority of the population.

IV.1.2 Methods

Nine heterogeneous breast phantoms and two homogeneous geometric phantoms were resized to fill a volume breast coil and individually fused to the whole-body model using a combination of voxel extrusion and removal operations. All cases were simulated using the finite-difference time-domain method.

IV.1.3 Results

Owing to higher-conductivity fibroglandular tissue regions, calculated local SAR in dense heterogeneous breast tissue was observed to be threefold higher as compared to a mostly fatty breast. Homogeneous phantoms were shown to be problematic, with the uniform fibroglandular phantom exhibiting wave behavior that generated excessive SAR hot spots.

IV.1.4 Conclusion

Simulating breast models as predominantly-fatty tissue can considerably underestimate the potential for tissue heating in women with substantial fibroglandular tissue. Accordingly, to appropriately characterize the worst-case scenario and adhere to safety limits, SAR analysis of breast coils should incorporate a heterogeneous breast model largely consisting of fibroglandular tissue.

IV.2 Introduction

Concern for patient safety is elevated for high field MRI studies, as specific absorption rate (SAR) scales according to B_0^2. Accordingly, the IEC and FDA guidelines on maximum SAR provide the basis for setting safe scanner parameters controlling input power to the radiofrequency (RF) coil. To comply with these guidelines for human studies, it is common practice to characterize RF transmit coils with full-wave electromagnetic modeling in order to establish the parameters ensuring safe power and SAR levels. Typically, finite-difference time-domain (FDTD) based methods are utilized owing to the ease of incorporating SAR calculations with heterogeneous body models (104-106). Simulating RF field behavior during breast scans necessitates incorporating a female body phantom into the FDTD mesh and while several adult female whole-body voxel models are available to the research community, all are oriented in the standing or supine positions (107-111); unfortunately these orientations limit the existing voxel models' applicability for simulating the filling factor of breast coils designed for women in the prone position, as is typically performed to avoid respiratory artifacts (74,76). Rudimentary efforts to

model a prone breast either replaced or supplemented the body model with geometric volumes representing homogeneous breast tissues (28,112).

Accurate breast modeling is confounded further by the anatomical variability of fatty and glandular tissues and their distinct mass densities and dielectric properties. Recognizing the need for anatomically-correct heterogeneous breast phantoms, van der Velden et al. fused a body model with 3D image data acquired from five healthy volunteers and ultimately noted that the observed disparity of simulated SAR distributions among these models was due to indeterminate variations in size and tissue makeup (113). Breast size and tissue density have great variability among the patient population; to classify the extent of breast tissue density across women, radiologists largely have embraced the four tissue composition categories prescribed by the American College of Radiology (ACR) in the Breast Imaging Reporting and Data System (BI-RADS®) (114). Using this method, breast density is defined as (a) almost entirely fat, (b) scattered fibroglandular tissue, (c) heterogeneous fibroglandular tissue, and (d) extreme fibroglandular tissue. An analysis of projected SAR encompassing these four classifications has yet to be examined.

In order to address the need to augment existing whole-body voxel models to account for prone imaging and the necessity to use heterogeneous breast tissue models, this study presents simulations at 7 T of a whole-body voxel model fused with nine high-resolution, anatomically-correct breast phantoms spanning the four tissue density classifications. Results confirm the proportions of lipid and fibroglandular tissues in breast phantoms have significant yet predictable implications on projected SAR; specifically, a breast with extreme fibroglandular tissue may be exposed to threefold the local 10-g

average SAR as compared to a mostly-fatty breast. Consequently, it is recommended that worst-case characterizations of breast coil safety include SAR analysis using a heterogeneous breast model categorized as BI-RADS-d, i.e., with extreme fibroglandular tissue.

IV.3 Methods

IV.3.1 Voxel Models

Of the presently reported adult non-pregnant female whole-body models, "Ella" from the Virtual Population is the highest-resolution and most comprehensive tissue model of the adult female body (107). Still, Ella 1) represents a woman in the supine position and 2) does not include any fibroglandular tissue in the breast region. For this work, we adapted nine heterogeneous 0.5-mm resolution pendant breast phantoms produced by the Hagness group at the University of Wisconsin–Madison (UW) for modeling microwave interactions between 0.5 and 20 GHz (115). These phantoms were labelled according to the subject's radiologist-assigned BI-RADS classification, denoted BI-RADS-a, -b, -c, and -d (114). At least two phantoms were developed for each category, with the exception of a single phantom for BI-RADS-d. All nine breast models included tissues defined as fatty, fibroglandular, transitional, and skin. Within the fatty and fibroglandular classes, the preceding Wisconsin–Calgary study of microwave dielectric properties identified increasing incongruence of conductivity and permittivity values above 500 MHz and accordingly divided both tissue classes into three tiers, each defined by single-pole Cole-Cole and Debye relaxation models (116). As these discrepancies in dielectric properties have not been observed in the RF band, the three tiers for each tissue type were merged

into single definitions as fat or fibroglandular tissues. The fat, fibroglandular, and skin tissues were assigned dielectric properties using the four-pole Cole-Cole equations stipulated by the IT'IS Foundation's tissue properties database (117). Voxels designated as transitional were assigned dielectric and physical properties averaging the values from breast fat and gland tissues. The resulting tissue dielectric properties at 7 T were $\sigma = 0.033$ S/m and $\varepsilon_r = 5.5$ for breast fat, $\sigma = 0.85$ S/m and $\varepsilon_r = 62$ for breast gland, $\sigma = 0.44$ S/m and $\varepsilon_r = 34$ for transitional tissue, and $\sigma = 0.64$ S/m and $\varepsilon_r = 50$ for skin. For comparison to the approach of utilizing homogeneous phantoms, a hemispherical cylinder was also generated to represent the breast in the two extreme cases; that is, this geometry included a 1.5-mm skin layer with the remainder uniformly assigned either fatty or fibroglandular tissue.

The volumetric tissue data from the nine image-derived phantoms were imported into MATLAB® (MathWorks, Natick, Massachusetts, USA). Since these voxel models only included heterogeneous tissue from a single breast, with the thorax modeled as a uniform 2D slab of skin, fat, and muscle, modifications were necessary to enable seamless integration with the Ella body model. The voxels from the thorax slab were removed and each phantom was duplicated for bilateral breast simulation. The breast phantoms were then enlarged using a nearest-neighbor interpolation routine to achieve a maximum 13.3-cm diameter in order to equally fill the RF coil. The finest-resolution Ella v1.3 voxel model, with 0.5-mm isotropic resolution, was imported into MATLAB for joining to the 0.5-mm breast phantoms. To position the breast phantoms on the Ella model before the fusing operation detailed below, two voxels were manually selected for centering the

posterior coronal layer of all left and right breast phantoms. These locations were determined by orienting the base of each breast phantom on the inmost posterior coronal plane in Ella's anterior thorax that solely overlapped breast tissue, fat, and skin, i.e., without encroaching on the pectoral fascia or adjacent muscle tissue. As a result, the medial extent of each breast phantom's base was situated underneath Ella's skin layer, while the lateral extent of the base extended in free space above the anterior skin layer, as shown in Figure IV-1a.

To automate integration of breast phantoms with a body model, MATLAB functions were developed to extrude and trim voxels from each breast phantom (code available on site listed below). First, voxels on the posterior coronal layer separated from Ella by free space were individually extruded toward the body model, penetrating the skin layer until encountering a voxel of adjacent tissue. By the same token, breast phantom voxels defined as skin that were situated inside the Ella phantom were removed from the phantom. Any remaining voxels from the heterogeneous breast phantoms that were co-located with the body model took meshing precedence in simulations, overwriting Ella voxels assigned skin, breast (fat), subcutaneous adipose tissue, and average infiltrated fat. These extrusion and trimming functions were applied independently for both the left and right breast positions. To illustrate this integration, the Ella voxel model fused with BI-RADS-b UW Phantom 2 is illustrated in Figure IV-1b.

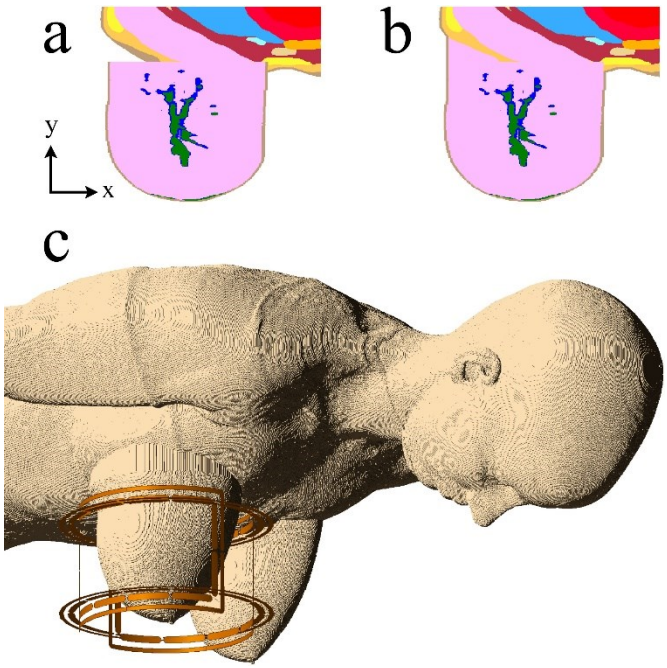

Figure IV-1. Renderings of the FDTD model including whole-body voxel model and breast phantom. **(a)** 2D axial mesh slices illustrating the initial discontinuity and **(b)** subsequent joining of BI-RADS-a UW Phantom 1 and Ella, with skin tissue labelled brown, glandular tissue green, transitional tissue blue, and fatty tissues pink, yellow, and orange; **(c)** rendering of the Ella voxel model fused with BI-RADS-c UW Phantom 2 surrounded by the quadrature FCE volume breast coil.

IV.3.2 Simulations

All breast phantoms were exported in a file format to facilitate import into commercial FDTD software (XFdtd® 7.4, Remcom, State College, Pennsylvania, USA). A previously-described quadrature ^{1}H breast volume coil (28,118) was positioned over each of the 11 right breast phantoms. The coil conductors were centered on the breast phantom and separated from the nearest skin voxel by 10 mm, as is the case in the actual coil former. The quadrature coil was driven by 298-MHz sinusoidal feeds with appropriate 90° phase shifts to simulate quadrature operation at 7 T. To account for the different impedances of the quadrature pair, feed amplitudes were adjusted to deliver equal input power to the two

quadrature channels with less than 0.5% (-23 dB) variation. Cell gridding was adaptively set between 0.5 and 1.0 mm for the coil and breast phantom, and all curved conductor geometries utilized the software's conformal meshing capabilities. The entire mesh was surrounded by a quarter-wavelength of free space padding cells and the boundary comprised seven perfectly matched layers. Simulations were run on a workstation with two linked NVIDIA GeForce® GTX 780 GPU cards, each with 3 GB RAM and 2304 cores, resulting in an average computational time of 73 minutes. Convergence was determined by transients dissipating to -50 dB deviation from the pure sinusoidal wave. Steady-state field data were calculated for all tissue voxels interior to the RF coil and globally on a central sagittal plane, while SAR data were calculated throughout the phantoms.

IV.3.3 Analysis

Steady-state data output from FDTD simulations were imported into MATLAB for analysis. Average $|\mathbf{B}_1^+|$ was computed inside the volume RF coil; only tissue voxels were included in the average, and voxels were weighted based on volume. As MR scanners typically monitor SAR with respect to the transmit magnitude, all SAR results in this study were scaled to achieve an average $|\mathbf{B}_1^+| = 1$ μT at 100% duty cycle. Accordingly, the raw and 10-g average SAR for each case were gauged in units W/kg/μT^2. To assess relative transmit coil power requirements as it relates to breast density, the net input power required to achieve average $|\mathbf{B}_1^+| = 1$ μT was also noted. In this way, the results easily may be scaled to any amplitude and duty cycle at 7 T.

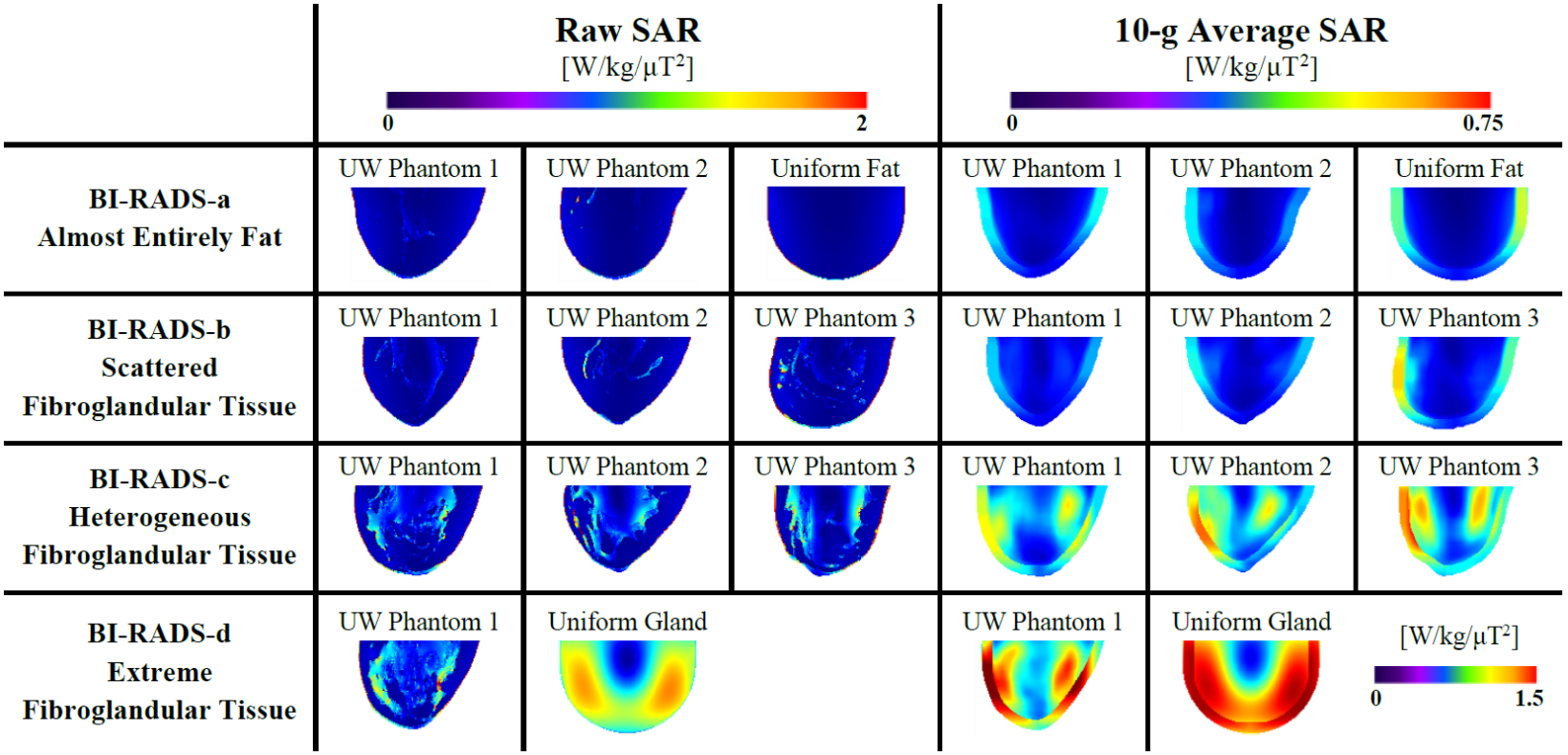

Figure IV-2. Raw and 10-g average SAR plots through the right breast's central sagittal slice for the 11 phantom cases. Extreme average SAR in the uniform glandular phantom required a separate scale bar for the single case. Note the increased SAR inside glandular tissue regions in the BI-RADS-c and -d phantoms. Furthermore, note the higher-density phantoms are more inclined to have localized internal SAR hot spots as opposed to surface localization in the mostly-fatty cases.

IV.4 Results

Figure IV-2 displays raw and 10-g average SAR plots on the central sagittal slice. The raw SAR plots reveal localized hot spots in the higher-conductivity fibroglandular tissue regions. Notably, all BI-RADS-c and -d phantoms resulted in maximum 10-g average SAR incorporating gland regions interior to the breast, while the maxima in all BI-RADS-a, -b, and uniform phantoms were on the breast surface incorporating the high-conductivity skin layer.

Coil efficiency and SAR data for all cases are shown in Table IV-1. Compared to the mostly-fatty BI-RADS-a phantoms, the maximum local 10-g average SAR was threefold higher in the denser BI-RADS-d UW Phantom 1. Note the extreme case of a uniform cylinder of dense gland tissue resulted in almost fourfold the SAR of the otherwise worst-case BI-RADS-d UW Phantom 1.

Table IV-1. Coil efficiency and maximum 10-g average SAR data for the 11 breast phantom cases. Input power is scaled to average $|\mathbf{B}_1^+| = 1$ μT throughout the breast.

Breast Phantom	Tissue Classification	Input Power [W]	Maximum 10-g Average SAR [W/kg/μT^2]
BI-RADS-a UW Phantom 1	almost entirely fat	0.63	0.30
BI-RADS-a UW Phantom 2	almost entirely fat	0.64	0.30
BI-RADS-b UW Phantom 1	scattered fibroglandular tissue	0.62	0.25
BI-RADS-b UW Phantom 2	scattered fibroglandular tissue	0.65	0.30
BI-RADS-b UW Phantom 3	scattered fibroglandular tissue	0.69	0.50
BI-RADS-c UW Phantom 1	heterogeneous fibroglandular tissue	0.72	0.61
BI-RADS-c UW Phantom 2	heterogeneous fibroglandular tissue	0.68	0.58
BI-RADS-c UW Phantom 3	heterogeneous fibroglandular tissue	0.72	0.69
BI-RADS-d UW Phantom 1	extreme fibroglandular tissue	0.75	0.89
Uniform fat with skin layer	almost entirely fat	0.67	0.45
Uniform gland with skin layer	extreme fibroglandular tissue	1.8	3.4

IV.5 Discussion and Conclusions

The results demonstrate significant variation among breast phantoms with varying levels of heterogeneity of healthy fat and glandular breast tissue. In addition, as shown in Figure IV-2, the geometric phantom representing homogeneous gland tissue illustrates the expected wave behavior in a uniform, electrically large dielectric (119). As such, its suitability for modeling in vivo breast scans is problematic.

This study has addressed two issues relevant to modeling the breast accurately—the need to augment existing body voxel models to account for prone imaging and the necessity to use heterogeneous breast tissue models. This work addressed the second issue by importing pre-categorized microwave phantoms, however other methods could be utilized including image data conversion (115,120,121) or heterogeneous phantom generation using software algorithms (122,123). Moreover, a high field calorimetry study spanning a variety of physical breast phantoms would be of particular interest. Even so, as the worst-case projected SAR clearly occurs with a denser breast, the characterization and SAR analysis of breast coils should incorporate a BI-RADS-d breast model in order to obtain the most conservative standards. Arguably, results from each of the remaining density classifications could also be included; in this way, a priori knowledge of the subject's breast density classification could allow for adjusting coil operating parameters, thus maximizing power availability while respecting safety limits. Conversely, if lacking prior knowledge of the subject, patient-specific strategies may be feasible; performing fat-water separation on a preliminary 3D image set may facilitate rapid SAR prediction, as has been demonstrated previously with body and brain imaging (124,125).

IV.6 Notes

The MATLAB library for resizing and fusing breast phantoms with a body model is available online at https://github.com/jrispoli/breast-body-fusion (SHA-1 hash 3b0e8b0740c8ae3688e694265b064df33ea728de). The image-derived breast phantoms utilized in this work are available online from the University of Wisconsin–Madison (126). As the fusing operation presented here does not modify the body model itself, nor require distribution with the body model, the resulting breast phantoms may be independently distributed under separate licensing terms.

CHAPTER V

TRAP DESIGN AND COMPONENT ANALYSIS FOR HIGH-POWER MULTINUCLEAR EXPERIMENTS

V.1 Introduction

Multinuclear MRI and MR spectroscopy (MRS) data reveal physiological details inaccessible to typical proton scans. Performing multinuclear experiments requires radiofrequency (RF) coils operating at both the proton (^{1}H) and second-nuclei (X) Larmor frequencies. If using two separate coils, they must be decoupled to prevent the induction of currents on the X-nuclei coil that cause sensitivity reduction and detuning of the ^{1}H coil. While inter-element interactions may be addressed by orthogonality, the inclusion of trap circuits provides the flexibility to position coils based on required anatomical coverage. The rudimentary trap circuit is a parallel *LC* tank tuned to the proton frequency and inserted on the X-nuclei coil. This design has been utilized extensively for multinuclear imaging and spectroscopy (127-132). One disadvantage of this approach is that the impedance of the *LC* circuit is inductive at the lower X frequency, counterproductive to current uniformity and homogeneity of the excitation RF field (B_1). To address this problem, a second capacitor may be added in series with the inductor, forming an *LCC* trap; as described by Webb, this improved trap circuit blocks current at the proton frequency while presenting an intended capacitance at the X frequency (133). Moreover, an analysis by Meyerspeer comparing *LC* and *LCC* traps elegantly proved the latter results in greater coil *Q*-factor and signal-to-noise ratio (SNR) (134).

Of the isotopes commonly interrogated in multinuclear studies, perhaps the most demanding is carbon-13 (^{13}C), owing to low natural abundance and strong J-couplings from ^{1}H-^{13}C chemical bonds. However, ^{13}C MRS studies draw considerable interest owing to the enhanced chemical shift range and reduced spectral overlap of organic compounds: metabolite ^{1}H resonances concentrated within 10 parts per million (ppm) are distributed across 200 ppm with ^{13}C MRS (7,8,135). To mitigate J-couplings and simplify spectra, proton-decoupling (B_2) pulses are typically transmitted during ^{13}C signal acquisition. The power required for B_2 is substantial and increases with decoupling bandwidth, presenting challenges for both broadband and high-field decoupling. For example, a broadband-decoupled ^{13}C spectrum of all metabolites necessitates B_2 excitation across the proton chemical shift range of 10 ppm and equates to 3 kHz at 7 T. In practice bandwidth is often limited by power capacity and specific absorption rate (SAR) safety guidelines, placing great importance on the ^{1}H coil transmit efficiency and the capability of ^{13}C coils to decouple from high-power ^{1}H irradiation. To date, a majority of in vivo studies at 7 T have relied on geometric decoupling to isolate the ^{13}C coil, circumventing the need for traps. Adriany and Gruetter achieved 700 Hz of WALTZ-16 decoupling in the head (34) with a 7T implementation of their widely-adopted, geometrically-decoupled quadrature half-volume coil (31). Chen et al. used the same coil design to apply B_{2max} = 18 μT in the leg (32), nominally decoupling across 1.6 kHz assuming B_2 inhomogeneity typical of a surface coil (33). Our group also has previously applied B_{2max} = 18 μT in the breast using a geometrically-decoupled volume coil optimized for homogeneity at 7 T (28). The initial reported use of an *LCC* trap for ^{13}C at 7 T was for on-resonance continuous wave

decoupling to examine one spectral peak (134). Serés Roig et al. subsequently added shielded *LCC* traps to two ^{13}C loops in a double-quadrature modification of the Adriany-Gruetter coil and decoupled across 700 Hz in the leg (136,137). Even at these limited bandwidths, ^{13}C coil coupling to B_2 has been shown to generate corona or arcing events (137). Considering that transient spikes degrade the resulting spectrum by uniformly distributing noise below the reciprocal of the discharge pulse width (64), the performance of lumped element components in this environment must be considered. This work assesses inductor and capacitor components in *LCC* trap configurations under the most demanding of applications: high-power broadband proton decoupling of ^{13}C MRS at 7 T. We show that the judicious selection of trap components leads to improved X-nuclei spectra under these stringent conditions.

V.2 Methods

V.2.1 Hardware

Six loops, with inner and outer diameters of 70 and 76 mm, respectively, were milled from 1-ounce copper-clad FR-4 boards and fabricated into coils tuned to 74.9 MHz for ^{13}C at 7 T. As illustrated in Figure V-1a, one loop coil was constructed without a trap circuit and included a 100-pF capacitor opposite the feed. Each of the remaining five loops instead incorporated an *LCC* trap circuit, as drawn in Figure V-1b, tuned to 298 MHz for blocking ^{1}H at 7 T. To preserve current uniformity on the trapped coils, *LCC* component values were established to collectively maintain the reactance of the 100-pF capacitor at 74.9 MHz. Per Eqs. 2 and 3 in (134), the minimum possible trap series inductor value was 12.2 nH; a value of L_s = 40 nH was chosen as a suitable balance of trap efficiency while limiting

the reduction of ^{13}C coil sensitivity. Of the two possible capacitance arrangements, we selected the solution that resulted in lower maximum voltages across components, with series trap capacitor C_s = 51 pF and parallel trap capacitor C_p = 8.2 pF. The coils were balanced matched and tuned to 74.9 MHz with variable capacitors (Voltronics, Salisbury, Maryland, USA). A single feed cable with an integrated 74.9-MHz balun and a 298-MHz cable trap attached to each individual coil through an SMA connection.

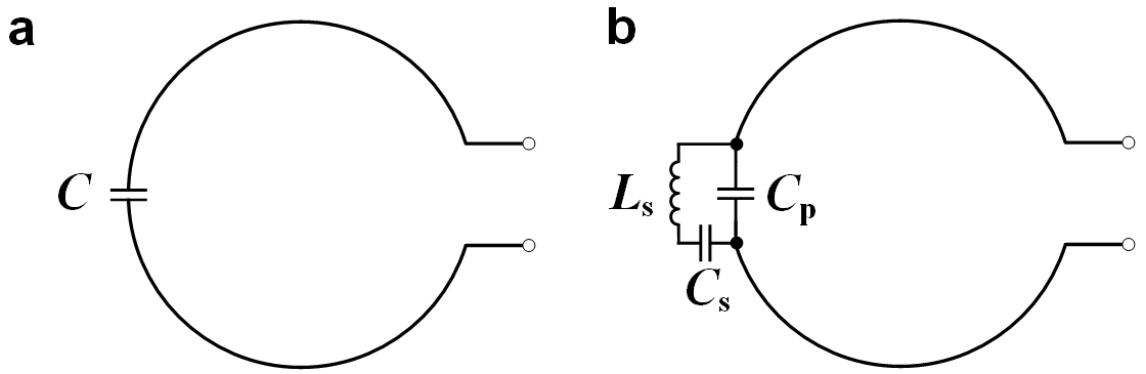

Figure V-1. Circuit diagrams for untrapped and *LCC*-trapped loop coils. (**a**) An untrapped loop coil with segmentation capacitor C = 100 pF, and (**b**) a loop coil with an *LCC* trap, composed of series capacitor C_s = 51 pF, series inductor L_s = 40 nH, and parallel capacitor C_p = 8.2 pF. At the X-nuclei frequency, the combined *LCC* reactance should equal that of C in (a).

V.2.2 Trap Components

Component selection is often a tradeoff between loss, quantified by R (or inversely Q), and power handling capability, rated as V_{max} or I_{max}. Unfortunately, ratings for working AC voltage are rarely provided by multilayer ceramic capacitor manufacturers. Limits for temperature-dependent breakdown owing to thermal runaway are typically listed;

however, the temperature-independent dielectric voltage breakdown is far more difficult to categorize as it is contingent on multiple factors including capacitance, frequency, and electrode materials (138). The latter failure mode is of greater concern with low duty cycle pulses shorter than the capacitor's thermal time constant; indeed, capacitor dielectric breakdown failures usually occur at peak RF voltages far below the rated DC working voltages (139). Clearly, components must withstand expected operating conditions, but excessively conservative selections lower coil Q and SNR while constraining coil design with bulky component footprints. For example, in a receive array application small components are desired to minimize the coil size, copper loading of the transmit coil, and B_1^+ flux blockage. As listed in Table V-1, we evaluated several multi-layer ceramic capacitors with DC voltage ratings from 1.5-7.2 kV (American Technical Ceramics, Huntington Station, New York, USA; Passive Plus, Huntington, New York, USA).

In this work, we constructed nominal 40-nH inductors using 18-AWG (d = 1 mm) copper magnet wire (8075, Belden, St. Louis, Missouri, USA) formed into 3.5 turns on a 2.3-mm radius with an overall length of 6 mm. In addition, we evaluated off-the-shelf tunable inductors (165 series, Coilcraft, Cary, Illinois, USA), an attractive solution for simplifying coil construction and trap tuning. Both solenoids are rated for maximum current based on wire gauge. While solenoids are relatively straightforward to construct and tune, their use in trap circuits presents some challenges; sharp wire bends on leads are prone to cause failures under high power, and the lack of inherent shielding permits interaction with transmit fields. To mitigate RF effects, the hand-wound solenoids were oriented in the B_0 direction to avoid coupling between the trap and the B_2 field (128), with

a subset circumferentially shielded to reduce electric field interactions (129,136). As an alternative to solenoid inductors, semi-rigid transmission line stubs were also evaluated (140). By precisely specifying the length l, a short-circuited segment of coaxial cable is transformed to a desired impedance [in Ω] of

$$Z_{sc} = jZ_0 \tan\left(\frac{2\pi}{\lambda} l\right), \quad \text{[V-1]}$$

with characteristic line impedance Z_0 and wavelength in the medium λ. The resulting inductance [in H] at angular frequency ω is given by

$$L = \frac{Z_0}{\omega} \tan\left(\frac{2\pi}{\lambda} l\right). \quad \text{[V-2]}$$

Owing to the steep slope of the above tangent term, fine-tuning the inductance by shortening the stub is an arduous task. Fortunately, replication is straightforward once the precise length is verified empirically. Parasitic reactance is innately diminished by using a stub topology, and in this work, electric field effects were further mitigated by conforming and soldering the stub to the coil trace and capping the short-circuited terminal with copper foil. The low physical profile and intrinsic shielding of the coaxial stub allows for greater flexibility for inductor positioning. In this configuration, the stub length must be shorter than the underlying coil segment, which may present a problem given the increased coil segmentation mandated at higher frequencies to prevent phase shifts. It is evident from the Z_0 term in Eq. [V-2] that a desired inductance may be achieved by employing a shorter length of higher-impedance transmission line. Accordingly, we found it advantageous to reduce the stub length by using 75-Ω semi-rigid coaxial cable (EZ 141-

75-Cu, EZ Form Cable, Hamden, Connecticut, USA). Photographs of the coils and trap circuits are shown in Figure V-2.

Table V-1. Trap components and manufacturer ratings for series inductor L_s, series capacitor C_s, and parallel capacitor C_p.

	L_s			C_s		C_p	
Coil	**Inductor Type**	**Part**	**Rating** [b]	**Part**	**Rating** [c]	**Part**	**Rating** [c]
Untrapped [a]	N/A	N/A	N/A	PPI 2225C101JP252X	2.5 kV	N/A	N/A
Trap 1	Variable solenoid, shielded	Coilcraft 165-02A06L	4.9 A	PPI 3838C470JP722X	7.2 kV	ATC 100E8R2BMN7200X	7.2 kV
Trap 2	Hand-wound solenoid, shielded	Belden 8075	2.3 A	PPI 3838C470JP722X	7.2 kV	ATC 100E8R2BMN7200X	7.2 kV
Trap 3	Hand-wound solenoid, unshielded	Belden 8075	2.3 A	PPI 3838C470JP722X	7.2 kV	ATC 100E8R2BMN7200X	7.2 kV
Trap 4	Transmission line stub	EZ Form EZ 141-75-Cu	5 kV	PPI 2225C470JP252X	2.5 kV	PPI 2225C8R2CP362X	3.6 kV
Trap 5	Transmission line stub	EZ Form EZ 141-75-Cu	5 kV	PPI 3838C470JP722X	7.2 kV	ATC 100E8R2BMN7200X	7.2 kV

[a] The untrapped coil's segmentation capacitor is listed as C_s.
[b] Solenoids are rated for RMS current causing 15°C rise from ambient; stubs are rated for RMS withstanding voltage at 60 Hz.
[c] Capacitors are rated for working DC voltage.

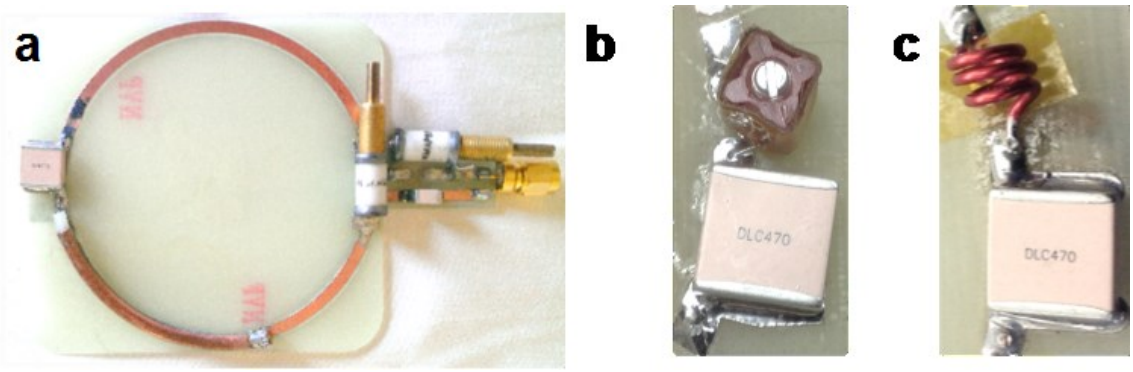

Figure V-2. Photographs illustrating various trap inductor types, all utilized in conjunction with identical 7.2-kV DC rated ceramic capacitors. (**a**) Carbon-13 coil incorporating Trap 5, with a short-circuited coaxial stub inductor conformed and soldered to the coil trace, (**b**) Trap 1 with a shielded commercial variable inductor, and (**c**) Trap 3 with an unshielded hand-wound solenoid. Note in all cases the parallel trap capacitor is obscured on the bottom side of the PCB.

V.2.3 Bench Measurements and Modeling

All traps and coils were characterized on the bench with a network analyzer (E5071C, Keysight Technologies, Santa Rosa, California, USA). All coils were loaded with a cylindrical phantom filled with canola oil, selected for its similar loading to the breast and suitability for ^{13}C spectroscopy. Coil Q-factors were calculated while matched and tuned to 74.9 MHz with the -7 dB S_{11} bandwidth method (64). Trap Q-factors were calculated from the S_{21} peaks at 298 MHz by marginally coupling to the isolated LCC structure with two decoupled 3-mm probes.

To model the traps under expected operating conditions, the EMF induced on the ^{13}C coil was estimated with Faraday's law of induction. Thus, as a worst-case scenario, in the presence of a uniform circularly-polarized proton decoupling field $B_2^+ = 20$ μT, an open-circuited linear loop coil with mean diameter of 73 mm induces 110 V across the terminals. The coils and trap circuits were then simulated numerically in SPICE, excited

by a 110-V, 298-MHz voltage source. Capacitor ESR values were identified from manufacturer data sheets, and coil and trap inductor losses were backed out from Q measurements.

V.2.4 Magnetic Resonance Spectroscopy

Carbon-13 spectra were acquired with a 7T Philips Achieva scanner, with WALTZ-16 used for proton decoupling. Given the limited efficacy of WALTZ-16 with inhomogeneous RF transmit coils (33), a previously-reported quadrature ^{1}H volume breast coil exhibiting better than 1-dB uniformity was employed for scout imaging and proton decoupling (28). A low-pass filter (BLP-100+, Mini-Circuits, Brooklyn, New York, USA) was included in the receive line directly before the preamplifier. Individually, the ^{13}C coils were placed in the homogeneous region of the breast coil and loaded with a 5-cm cylinder of canola oil. Pulse-and-acquire ^{13}C spectra were averaged from eight acquisitions of 4096 samples over 16 kHz, with TR = 8 s, TE = 150 μs, 70° flip angle, without NOE enhancement. WALTZ-16 was centered at 2.3 ppm with B_2^+ = 20 μT applied during the initial 20% (51 ms) of the 256 ms readout. With homogeneous B_{2max} = 20 μT, WALTZ-16 is expected to recover 90% of the perfectly-decoupled peak height across 2 kHz (33). Fully-coupled spectra were also acquired to illustrate decoupling effectiveness as well as quantify the increase in noise during decoupling pulses.

All spectra were processed in MATLAB® (MathWorks, Natick, Massachusetts, USA) using an in-house code library. Zero and first order phase corrections were applied to obtain absorption mode spectra, and baselines were corrected by piecewise cubic interpolation to simplify peak integration. No line broadening was applied. Peaks were

identified from the established canola oil ^{13}C NMR spectrum (141). SNR was calculated by dividing the integral of the largest peak by the standard deviation of the baseline noise in a vacant 500-sample region. To quantify noise breakthrough during decoupling, the standard deviations of the time-domain noise were evaluated from 200-sample regions immediately before and after the completion of the WALTZ-16 duty cycle, as illustrated in Figure V-3b. In this way, a lower ratio of decoupled versus coupled noise suggests superior noise rejection.

V.3 Results

SNR and loaded *Q*-factors for the coils and traps are listed in

Table V-2. The spectra acquired by the various coils are displayed in Figure V-3a. All trap configurations mitigated, to some degree, the detrimental noise breakthrough from WALTZ-16 transmission observed with the untrapped coil throughout the decoupling duty cycle, as shown in Figure V-3b. Trap 5, with a coaxial stub inductor, led to the highest coil SNR, slightly better than with the unshielded hand-wound solenoid of trap 3. The FIDs from other trap configurations acquired more appreciable noise during WALTZ-16 pulses, with spectral SNR suffering as a result. Notably, capacitors rated for 7.2 kV DC demonstrated superior ability to avoid intermittent transient noise spikes compared to alternatives rated for lower voltages.

In the SPICE model of the coil and *LCC* circuit, the coil *Q* was set to 200. The resulting AC current amplitude exceeded 3 A with voltage surpassing 200 V across both the inductor and the 8.2-pF capacitor. Note this simulation assumes the EMF arises solely

from the decoupling B_2 without considering additional sources such as concentrated E field regions.

As seen in Figure V-3a, the largest ^{13}C peak was from bulk methylene resonances at 30 ppm, with other resolved peaks from methyl (15 ppm), glycerol (62 ppm), and olefin (130 ppm). The two traps resulting in the highest SNR, Traps 3 and 5, were also tested with B_{2max} = 20 μT applied during the initial 70 ms of sampling, a 50% increase in WALTZ-16 duty cycle. The FIDs acquired from these two cases showed no discernable noise breakthrough or voltage spikes; the acquisition from the coil with Trap 3 is shown in Figure V-3c.

Table V-2. Bench measurement and spectroscopy results from the untrapped and five trapped coils.

Coil	Trap *Q*	Coil *Q*	SNR	Noise Ratio	FID Noise Spikes
Untrapped	N/A	267	1383	4.26	14
Trap 1	113	206	1183	1.47	4
Trap 2	122	199	4229	1.68	0
Trap 3	168	239	5958	1.51	2
Trap 4	117	228	3173	2.98	14
Trap 5	108	221	6012	1.58	4

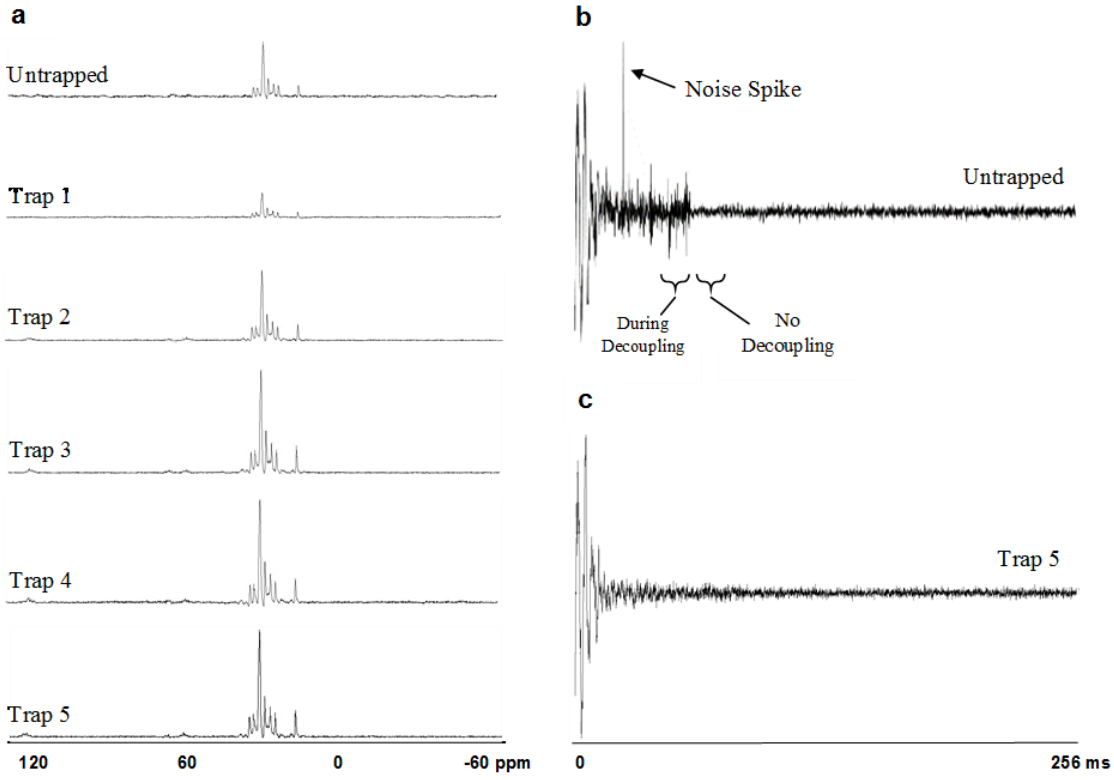

Figure V-3. Spectra and FIDs from MRS experiments. (**a**) Carbon-13 spectra from all coils using WALTZ-16 decoupling B_{2max} = 20 μT with 20% duty cycle. The coils incorporating Trap 3 (unshielded solenoid and 7.2-kV DC rated capacitors) and Trap 5 (coaxial stub and 7.2-kV DC rated capacitors) detected spectra with the largest ^{13}C peaks and greatest SNR. Other configurations resulted in lower SNR owing to reduced peak height, including Trap 1 (variable commercial solenoid) and Trap 2 (shielded solenoid), and baseline oscillations owing to intermittent noise spikes during FID acquisition observed with coils utilizing 2.5-kV DC rated capacitors, including the untrapped coil and Trap 4 (coaxial stub). (**b**) A FID detected from the untrapped coil illustrates an intermittent noise spike. Additionally, this FID clearly exhibits noise breakthrough during WALTZ-16 transmission, and the 200-sample regions used for calculating the Noise Ratio are underscored. (**c**) The coil with Trap 5, demonstrating superior SNR in (a), also withstood noise breakthrough under more demanding conditions: B_{2max} = 20 μT with an extended 30% duty cycle.

V.4 Discussion and Conclusions

Considering the low physical profile, as well as the confined region for magnetic energy storage, the stub inductor may be preferred for *LCC* trap design. As the results presented in this work were acquired at an extreme of power demands for decoupling (^{13}C at 7T), the results should generalize to guide trap design for lower field strengths and MRS of other nuclei. It is worth noting we previously found the inductor stub to be problematic if not shaped conformal to the coil trace, with unacceptable noise introduced when B_2^+ reached 15 μT.

While this study compared decoupling efficiency with WALTZ-16, performance may be improved with alternate decoupling schemes. Adiabatic pulses have been shown to improve decoupling bandwidth over WALTZ-16 by 30% using the same RF power (34), and frequency-modulated rectangular pulses may prove to be more beneficial for high-bandwidth applications (33). Furthermore, eliminating traditional proton-decoupling pulses altogether using alternative techniques may alleviate the power requirements of multinuclear MRS; 2D HSQC was recently demonstrated at 7 T, with initial results yielding linearly-decoupled ^{13}C absolute-value mode spectra (142).

CHAPTER VI

CONCLUSION

This dissertation has described efforts to solve the engineering challenges heretofore restricting the in vivo quantification of broadband-decoupled natural abundance ^{13}C in the breast at high fields. As part of this work, novel RF coil features and implementations were modeled, designed, constructed, characterized on the bench, and utilized in 7T MR scanning. The results presented herein indicate the specific aims of this dissertation have been achieved. Now armed with 1) guidelines for a flexible and easily fabricated shielding configuration in order to improve B_1^+ transmit efficiency, 2) a grasp of the FCE implantation on multi-element RF coils for driving equal currents irrespective of inductive coupling and sample loading, 3) modeling approaches to ensure patient safety during high-field breast studies, and 4) trap circuits capable of isolating multinuclear coils under broadband proton decoupling conditions, the MR community is better prepared to define new directions to advance this line of research.

As with most scientific investigations pushing the boundaries of what is achievable, with high-field broadband proton-decoupled ^{13}C MRS there are several identifiable areas for near-term improvements. From a coil hardware viewpoint, the logical next step forward is to employ the findings of this work to construct and utilize a multi-element ^{13}C breast receive array. Utilizing the FCE transmit coil with judiciously-selected coplanar shielding, and low-profile *LCC* trap circuits on each ^{13}C array element, the resulting improvement in SNR may spur new pathways of metabolic research. From a

decoupling sequence perspective, lower power deposition as compared to WALTZ-16 may be attainable with frequency-modulated, phase-modulated, or adiabatic pulses (33). A decrease in power deposition for equivalent B_2 decoupling performance could potentially spark interest in high-field proton-decoupled ^{13}C studies in other anatomies including the brain, for which SAR safety limits are more stringent. Regarding data acquisition systems, a scalable multi-channel multinuclear receiver interface is needed to detect ^{13}C concurrently from parallel elements, and work continues in this area (143). In due course, significant SNR improvements from massively parallel multinuclear receive arrays will be attained at high fields, possibly with systems capable of acquiring concurrent data from multiple nuclei.

Other areas of MR research may also benefit from the work presented herein. The necessity for adaptable RF shielding schemes in high-field coils is clear. In Chapter II, coplanar shielding was demonstrated with large surface coils as well as volume arrays of overlapped elements. The design flexibility afforded by coplanar shielding permits deployment in a variety of applications, from clinical 3T to leading-edge 10.5T scanners. The FCE technique described in Chapter III was employed for overcoming the asymmetric loading from the thorax that otherwise would limit MR sensitivity in the breast, but applications for FCE extend beyond breast imaging. For example, as the number of elements in transmit arrays scales upward, it becomes increasingly difficult to drive each element from an individual amplifier channel. Traditional power splitting techniques present limitations at higher fields, as minor variations in coil impedances presented by variably-spaced loads, no matter the anatomy, govern the current amplitude delivered to

each element. Accordingly FCE may ultimately find widespread adoption in parallel transmit applications. The trap results presented in Chapter V are relevant beyond 7T ^{13}C coils; they may also be applied to high-field MRS of other nuclei as well as multinuclear RF coil design for lower B_0 fields. As for EM modeling, the list of applications is practically limitless. The automated, iterative capabilities of both custom and commercial EM solvers permit evaluation of a wide variety of design criteria, including geometry, circuitry, and novel materials. The FDTD simulation considerations presented in this work, for both coil design in Chapter II and safety characterization in Chapter IV, convey practical information to the wider MR community that possibly could permeate into other biological EM arenas such as microwave, terahertz, and photonics.

REFERENCES

1. Bloch F. Nuclear induction. Phys Rev 1946;70:460-474.

2. Bloch F, Hansen WW, Packard M. The nuclear induction experiment. Phys Rev 1946;70:474-485.

3. Purcell EM, Torrey HC, Pound RV. Resonance absorption by nuclear magnetic moments in a solid. Phys Rev 1946;69:37-38.

4. Holm C. Observation of chemical shielding and spin coupling of C^{13} nuclei in various chemical compounds by nuclear magnetic resonance. J Chem Phys 1957;26:707-708.

5. Lauterbur PC. C^{13} Nuclear magnetic resonance spectra. J Chem Phys 1957;26:217-218.

6. de Graaf RA. In vivo NMR spectroscopy. 2nd Ed. West Sussex, England: John Wiley & Sons; 2007. p. 43-110.

7. Bottomley PA. Human in vivo NMR spectroscopy in diagnostic medicine: clinical tool or research probe? Radiology 1989;170:1-15.

8. Silverstein RM, Webster FX, Kiemle DJ. Spectrometric identification of organic compounds. 7th Ed. Hoboken, New Jersey: John Wiley & Sons; 2005. 512 p.

9. Subramanian R, Webb AG. Design of solenoidal microcoils for high-resolution ^{13}C NMR spectroscopy. Anal Chem 1998;70:2454-2458.

10. Webb AG, Collins CM. Parallel transmit and receive technology in high-field magnetic resonance neuroimaging. Int J Imaging Syst Technol 2010;20:2-13.

11. Cerdan S, Seelig J. NMR studies of metabolism. Annu Rev Biophys Biophys Chem 1990;19:43-67.

12. Bottomley PA, Hardy CJ, Roemer PB, Mueller OM. Proton-decoupled, Overhauser-enhanced, spatially localized carbon-13 spectroscopy in humans. Magn Reson Med 1989;12:348-363.

13. Heerschap A, Luyten PR, Van Der Heyden JI, Oosterwaal LJMP, Hollander JAD. Broadband proton decoupled natural abundance ^{13}C NMR spectroscopy of humans at 1.5 T. NMR Biomed 1989;2:124-132.

14. Jue T, Rothman DL, Tavitian BA, Shulman RG. Natural-abundance ^{13}C NMR study of glycogen repletion in human liver and muscle. Proc Natl Acad Sci 1989;86:1439-1442.

15. Beckmann N. In vivo ^{13}C spectroscopy in humans. In: Rudin M, editor. In-vivo Magnetic resonance spectroscopy III: In-vivo MR spectroscopy: potential and limitations. Volume 28, NMR basic principles and progress. Berlin, Heidelberg: Springer Berlin Heidelberg; 1992. p. 73-100.

16. Ross B, Lin A, Harris K, Bhattacharya P, Schweinsburg B. Clinical experience with ^{13}C MRS in vivo. NMR Biomed 2003;16:358-369.

17. Bluml S. In vivo ^{13}C MRS. In: Webb GA, editor. Modern magnetic resonance. Dordrecht, Netherlands: Springer; 2006. p. 1099-1112.

18. Seelig J, Burlina AP. Carbon-13 magnetic resonance in biology and medicine. Clin Chim Acta 1992;206:125-136.

19. Gruetter R, Weisdorf SA, Rajanayagan V, Terpstra M, Merkle H, Truwit CL, Garwood M, Nyberg SL, Ugurbil K. Resolution improvements in in vivo ^{1}H NMR spectra with increased magnetic field strength. J Magn Reson 1998;135:260-264.

20. Moser E. Ultra-high-field magnetic resonance: why and when? World J Radiol 2010;2:37.

21. Moser E, Stahlberg F, Ladd ME, Trattnig S. 7-T MR—from research to clinical applications? NMR Biomed 2012;25:695-716.

22. Vaughan JT, Garwood M, Collins C, Liu W, DelaBarre L, Adriany G, Andersen P, Merkle H, Goebel R, Smith M. 7T vs. 4T: RF power, homogeneity, and signal-to-noise comparison in head images. Magn Reson Med 2001;46:24-30.

23. Armstrong B, Doll R. Environmental factors and cancer incidence and mortality in different countries, with special reference to dietary practices. Int J Cancer 1975;15:617-631.

24. Cho E, Spiegelman D, Hunter DJ, Chen WY, Stampfer MJ, Colditz GA, Willett WC. Premenopausal fat intake and risk of breast cancer. J Natl Cancer Inst 2003;95:1079-1085.

25. Bougnoux P, Giraudeau B, Couet C. Diet, cancer, and the lipidome. Cancer Epidemiol Biomarkers Prev 2006;15:416-421.

26. Dimitrov IE, Douglas D, Ren J, Smith NB, Webb AG, Sherry AD, Malloy CR. In vivo determination of human breast fat composition by ^{1}H magnetic resonance spectroscopy at 7 T. Magn Reson Med 2012;67:20-26.

27. Dimitrov I, Ren J, Douglas D, Sherry A, Malloy C. In vivo detection of trans-fatty acids by ^{13}C MRS at 7T. In Proceedings of the 18th Annual Meeting of ISMRM, Stockholm, Sweden, 2010. p. 374.

28. McDougall MP, Cheshkov S, Rispoli J, Malloy C, Dimitrov I, Wright SM. Quadrature transmit coil for breast imaging at 7 tesla using forced current excitation for improved homogeneity. J Magn Reson Imaging 2014;40:1165-1173.

29. Ernst RR. Nuclear magnetic double resonance with an incoherent radio-frequency field. J Chem Phys 1966;45:3845-3861.

30. Shaka A, Keeler J, Frenkiel T, Freeman R. An improved sequence for broadband decoupling: WALTZ-16. J Magn Reson 1983;52:335-338.

31. Adriany G, Gruetter R. A half-volume coil for efficient proton decoupling in humans at 4 tesla. J Magn Reson 1997;125:178-184.

32. Chen X, Boesiger P, Henning A. Cholesterol detection in adipose tissue by natural abundance in vivo ^{13}C MRS at 7T. In Proceedings of the 20th Annual Meeting of ISMRM, Melbourne, Australia, 2012. p. 1762.

33. de Graaf RA. Theoretical and experimental evaluation of broadband decoupling techniques for in vivo nuclear magnetic resonance spectroscopy. Magn Reson Med 2005;53:1297-1306.

34. Gruetter R, Adriany G, Andersen P, Ugurbil K. Feasibility of ^{13}C NMR spectroscopy of the human brain at 7 tesla using adiabatic ^{1}H decoupling. In Proceedings of the 9th Annual Meeting of ISMRM, Glasgow, Scotland, 2001. p. 627.

35. Wright SM, Wald LL. Theory and application of array coils in MR spectroscopy. NMR Biomed 1997;10:394-410.

36. Keltner JR, Carlson JW, Roos MS, Wong STS, Wong TL, Budinger TF. Electromagnetic fields of surface coil in vivo NMR at high frequencies. Magn Reson Med 1991;22:467-480.

37. Vaughan JT. Ultra high field MRI: high-frequency coils. In: Robitaille P-M, Berliner LJ, editors. Ultra high field magnetic resonance imaging. New York: Springer; 2006. p. 127-161.

38. Ong KC, Wen H, Chesnick AS, Duewell S, Jaffer FA, Balaban RS. Radiofrequency shielding of surface coils at 4.0 T. J Magn Reson Imaging 1995;5:773-777.

39. Adriany G, Yacoub E, Tkac I, Andersen P, Merkle H, Vaughan JT, Ugurbil K. Shielded surface coils and halfvolume cavity resonators for imaging and spectroscopy applications at 7 tesla. In Proceedings of the 8th Annual Meeting of ISMRM, Denver, Colorado, USA, 2000. p. 563.

40. Vaughan JT, Hetherington HP, Otu JO, Pan JW, Pohost GM. High frequency volume coils for clinical NMR imaging and spectroscopy. Magn Reson Med 1994;32:206-218.

41. Wu B, Wang C, Kelley DA, Xu D, Vigneron DB, Nelson SJ, Zhang X. Shielded microstrip array for 7T human MR imaging. IEEE Trans Med Imaging 2010;29:179-184.

42. Zhang X, Ugurbil K, Chen W. Microstrip RF surface coil design for extremely high-field MRI and spectroscopy. Magn Reson Med 2001;46:443-450.

43. Adriany G, Van de Moortele P-F, Wiesinger F, et al. Transmit and receive transmission line arrays for 7 tesla parallel imaging. Magn Reson Med 2005;53:434-445.

44. Belliveau J-G, Gilbert KM, Abou-Khousa M, Menon RS. Analysis of circumferential shielding as a method to decouple radiofrequency coils for high-field MRI. Concepts Magn Reson Part B Magn Reson Eng 2013;43B:11-21.

45. Gilbert KM, Belliveau J-G, Curtis AT, Gati JS, Klassen LM, Menon RS. A conformal transceive array for 7 T neuroimaging. Magn Reson Med 2012;67:1487-1496.

46. Gilbert KM, Curtis AT, Gati JS, Klassen LM, Villemaire LE, Menon RS. Transmit/receive radiofrequency coil with individually shielded elements. Magn Reson Med 2010;64:1640-1651.

47. Lanz T, Griswold M. Concentrically shielded surface coils—a new method for decoupling phased array elements. In Proceedings of the 14th Annual Meeting of ISMRM, Seattle, Washington, USA, 2006. p. 217.

48. McDougall MP, Wright SM, Rispoli J, Carrillo M, Dimitrov I, Cheshkov S, Malloy C. A printed loop element with integrated capacitors and co-planar shield for 7 tesla. In Proceedings of the 19th Annual Meeting of ISMRM, Montréal, Québec, Canada, 2011. p. 1875.

49. El-Khair IA, Korvink JG, Hennig J, Moenich G. The shielding of RF MRI coils using double-sided EMI shield. In Proceedings of the 17th Annual Meeting of ISMRM, Honolulu, Hawaii, USA, 2009. p. 105.

50. Doty FD, Entzminger G, Kulkarni J, Pamarthy K, Staab JP. Radio frequency coil technology for small-animal MRI. NMR Biomed 2007;20:304-325.

51. Chen CN, Hoult DI. Biomedical magnetic resonance technology. Bristol, England: Adam Hilger; 1989. 340 p.

52. Hoult DI, Lauterbur PC. The sensitivity of the zeugmatographic experiment involving human samples. J Magn Reson 1979;34:425-433.

53. Gevorgian SS, Mironenko IG. Asymmetric coplanar-strip transmission lines for MMIC and integrated optic applications. Electron Lett 1990;26:1916-1918.

54. Froncisz W, Jesmanowicz A, Hyde JS. Inductive (flux linkage) coupling to local coils in magnetic resonance imaging and spectroscopy. J Magn Reson 1986;66:135-143.

55. Liu W, Yang Q, Collins C, Smith M. Numerical evaluation of power radiated by a loaded volume coil at high fields. In Proceedings of the 11th Annual Meeting of ISMRM, Toronto, Ontario, Canada, 2003. p. 2393.

56. Liu W, Yang QX, Collins CM, Smith MB. Numerical evaluation of power radiated and dissipated by a loaded surface coil at high field. In Proceedings of the 10th Annual Meeting of ISMRM, Honolulu, Hawaii, USA, 2002. p. 915.

57. Balanis CA. Antenna theory: analysis and design. 3rd Ed. Hoboken, New Jersey: John Wiley & Sons; 2005. 1136 p.

58. Best SR. Small and fractal antennas. In: Balanis CA, editor. Modern antenna handbook. Hoboken, New Jersey: John Wiley & Sons; 2007. p. 475-528.

59. Grist TM, Hyde JS. Resonators for in vivo ^{31}P NMR at 1.5 T. J Magn Reson 1985;61:571-578.

60. Liu W. RF field modeling for double-tuned volume coils. eMagRes 2011. doi: 10.1002/9780470034590.emrstm1159.

61. Kumar A, Edelstein WA, Bottomley PA. Noise figure limits for circular loop MR coils. Magn Reson Med 2009;61:1201-1209.

62. Wright SM. Full-wave analysis of planar radiofrequency coils and coil arrays with assumed current distribution. Concepts Magn Reson 2002;15:2-14.

63. Liu W, Kao C-P, Collins CM, Smith MB, Yang QX. On consideration of radiated power in RF field simulations for MRI. Magn Reson Med 2013;69:290-294.

64. Doty F, Connick T, Ni X, Clingan M. Noise in high-power, high-frequency double-tuned probes. J Magn Reson 1988;77:536-549.

65. Roemer P, Edelstein W, Hayes C, Souza S, Mueller O. The NMR phased array. Magn Reson Med 1990;16:192-225.

66. By S, Rispoli JV, Cheshkov S, Dimitrov I, Cui J, Seiler S, Goudreau S, Malloy C, Wright SM, McDougall MP. A 16-channel receive, forced current excitation dual-transmit coil for breast imaging at 7T. PLoS One 2014;9:e113969.

67. Pruessmann KP, Weiger M, Scheidegger MB, Boesiger P. SENSE: sensitivity encoding for fast MRI. Magn Reson Med 1999;42:952-962.

68. Wiesinger F, Van de Moortele P-F, Adriany G, De Zanche N, Ugurbil K, Pruessmann KP. Parallel imaging performance as a function of field strength--an experimental investigation using electrodynamic scaling. Magn Reson Med 2004;52:953-964.

69. Weiger M, Pruessmann KP, Leussler C, Röschmann P, Boesiger P. Specific coil design for SENSE: a six-element cardiac array. Magn Reson Med 2001;45:495-504.

70. Haddadin IS, McIntosh A, Meisamy S, Corum C, Styczynski Snyder AL, Powell NJ, Nelson MT, Yee D, Garwood M, Bolan PJ. Metabolite quantification and high-field MRS in breast cancer. NMR Biomed 2009;22:65-76.

71. Berg WA, Gutierrez L, NessAiver MS, Carter WB, Bhargavan M, Lewis RS, Ioffe OB. Diagnostic accuracy of mammography, clinical examination, US, and MR imaging in preoperative assessment of breast cancer. Radiology 2004;233:830-849.

72. Bolan PJ, Meisamy S, Baker EH, Lin J, Emory T, Nelson M, Everson LI, Yee D, Garwood M. In vivo quantification of choline compounds in the breast with ^{1}H MR spectroscopy. Magn Reson Med 2003;50:1134-1143.

73. Hwang J-H, Bluml S, Leaf A, Ross BD. In vivo characterization of fatty acids in human adipose tissue using natural abundance ^{1}H decoupled ^{13}C MRS at 1.5 T: clinical applications to dietary therapy. NMR Biomed 2003;16:160-167.

74. Hylton NM, Frankel SD. Imaging techniques for breast MR imaging. Magn Reson Imaging Clin N Am 1994;2:511-525.

75. Kuhl CK, Schrading S, Leutner CC, Morakkabati-Spitz N, Wardelmann E, Fimmers R, Kuhn W, Schild HH. Mammography, breast ultrasound, and magnetic resonance imaging for surveillance of women at high familial risk for breast cancer. J Clin Oncol 2005;23:8469-8476.

76. Orel SG, Schnall MD. MR imaging of the breast for the detection, diagnosis, and staging of breast cancer. Radiology 2001;220:13-30.

77. Warner E, Messersmith H, Causer P, Eisen A, Shumak R, Plewes D. Systematic review: using magnetic resonance imaging to screen women at high risk for breast cancer. Ann Intern Med 2008;148:671-679.

78. Ibrahim TS, Hue Y-K, Tang L. Understanding and manipulating the RF fields at high field MRI. NMR Biomed 2009;22:927-936.

79. Mao W, Smith MB, Collins CM. Exploring the limits of RF shimming for high-field MRI of the human head. Magn Reson Med 2006;56(4):918-922.

80. Katscher U, Börnert P, Leussler C, van den Brink JS. Transmit SENSE. Magn Reson Med 2003;49:144-150.

81. Zhu Y. Parallel excitation with an array of transmit coils. Magn Reson Med 2004;51:775-784.

82. Krug R, Stehling C, Kelley DAC, Majumdar S, Link TM. Imaging of the musculoskeletal system in vivo using ultra-high field magnetic resonance at 7 T. Invest Radiol 2009;44:613-618.

83. Welsch GH, Juras V, Szomolanyi P, Mamisch TC, Baer P, Kronnerwetter C, Blanke M, Fujita H, Trattnig S. Magnetic resonance imaging of the knee at 3 and 7 tesla: a comparison using dedicated multi-channel coils and optimised 2D and 3D protocols. Eur Radiol 2012;22:1852-1859.

84. Jasik H. Antenna engineering handbook. 1st Ed. New York: McGraw-Hill; 1961. 1021 p.

85. Lo Y, Wright S, Navarro J, Davidovitz M. Antennas IV: microstrip antennas. In: Chang K, editor. Handbook of RF/microwave components and engineering. Hoboken, New Jersey: Wiley-Interscience; 2003. p. 775-904.

86. McDougall MP, Knight JM, Eigenbrodt EE, Wright SM, Chang C-W. A simple approach to overcoming mutual coupling effects in some transmit array coils for magnetic resonance imaging. In Proceedings of the 30th Annual International Conference of the IEEE Engineering in Medicine and Biology Society, Vancouver, British Columbia, Canada, 2008. p. 2043-2046.

87. Lee R, Moy L, Brown R, McGorty K, Sfefanescu C, Wang Y, Peck N. 7T high resolution breast MRI. In Proceedings of the 14th Annual Meeting of ISMRM, Seattle, Washington, USA, 2006. p. 2900.

88. Sun L, Olsen JO, Robitaille P-ML. Design and optimization of a breast coil for magnetic resonance imaging. Magn Reson Med 1993;11:73-80.

89. Tomanek B, Hoult DI, Chen X, Gordon R. Probe with chest shielding for improved breast MRI. Magn Reson Med 2000;43:917-920.

90. Kaiser WA, Kess H. [A prototype double coil for MR breast measurement]. Rofo 1989;151:103-105.

91. Kelcz F, Santyr GE, Cron GO, Mongin SJ. Application of a quantitative model to differentiate benign from malignant breast lesions detected by dynamic, gadolinium-enhanced MRI. J Magn Reson Imaging 1996;6:743-752.

92. Stanwell P, Gluch L, Clark D, Tomanek B, Baker L, Giuffrè B, Lean C, Malycha P, Mountford C. Specificity of choline metabolites for in vivo diagnosis of breast cancer using ^{1}H MRS at 1.5 T. Eur Radiol 2005;15:1037-1043.

93. Zhai X, Kurpad K, Smith M, Mahay D, Harter R, Fain S. Breast coil for real time MRI guided interventional device. In Proceedings of the 15th Annual Meeting of ISMRM, Berlin, Germany, 2007. p. 445.

94. Krishnamurthy N, Zhao T, Ibrahim TS. Effects of receive-only inserts on specific absorption rate, B_1^+ field, and Tx coil performance. J Magn Reson Imaging 2014;39:475-484.

95. Heilman J, Gudino N, Riffe M, Liu P, Griswold M. A four channel transmission array based on CMCD amplifier. In Proceedings of the 17th Annual Meeting of ISMRM, Honolulu, Hawaii, USA, 2009. p. 3027.

96. Hoult DI, Foreman D, Kolansky G, Kripiakevich D. Overcoming high-field RF problems with non-magnetic Cartesian feedback transceivers. Magn Reson Mater Phys, Biol Med 2008;21:15-29.

97. Gabriel S, Lau RW, Gabriel C. The dielectric properties of biological tissues: II. measurements in the frequency range 10 Hz to 20 GHz. Phys Med Biol 1996;41:2251.

98. Boyer JS, Wright SM, Porter JR. An automated measurement system for characterization of RF and gradient coil parameters. J Magn Reson Imaging 1998;8:740-747.

99. Kanal E, Barkovich AJ, Bell C et al. ACR guidance document on MR safe practices: 2013. J Magn Reson Imaging 2013;37:501-530.

100. Yarnykh VL. Actual flip-angle imaging in the pulsed steady state: a method for rapid three-dimensional mapping of the transmitted radiofrequency field. Magn Reson Med 2007;57:192-200.

101. Takano S, Horie T, Endo K, Shibukawa S, Honda M, Muro I, Ogino T. [Problem of spectral attenuated with inversion recovery fat suppression method with respiratory-gated]. Nihon Hoshasen Gijutsu Gakkai Zasshi 2013;69:92-98.

102. Dimitrov IE, Madhuranthakam A, Cheshkov S, Seiler S, Goudreau S, Rispoli J, McDougall MP, Wright SM, Malloy CR. BreastVIEW: isotropic 3D high resolution T2-weighted breast imaging at 7T. In Proceedings of the 21th Annual Meeting of ISMRM, Salt Lake City, Utah, USA. p. 3370.

103. Cheshkov S, Dimitrov I, Rispoli J, Gonzalez E, Malloy C, McDougall M, Wright S. Proton-decoupled ^{13}C MRS of the breast at 7T. In Proceedings of the 20th Annual Meeting of ISMRM, Melbourne, Victoria, Australia, 2012. p. 4428.

104. Collins CM, Li S, Smith MB. SAR and B_1 field distributions in a heterogeneous human head model within a birdcage coil. Magn Reson Med 1998;40:847-856.

105. Dimbylow P. FDTD calculations of the whole-body averaged SAR in an anatomically realistic voxel model of the human body from 1 MHz to 1 GHz. Phys Med Biol 1997;42:479.

106. Jin J, Chen J. On the SAR and field inhomogeneity of birdcage coils loaded with the human head. Magn Reson Med 1997;38:953-963.

107. Christ A, Kainz W, Hahn EG, et al. The virtual family—development of surface-based anatomical models of two adults and two children for dosimetric simulations. Phys Med Biol 2010;55:N23.

108. Dimbylow P. Development of the female voxel phantom, NAOMI, and its application to calculations of induced current densities and electric fields from applied low frequency magnetic and electric fields. Phys Med Biol 2005;50:1047.

109. Liu W, Collins CM, Smith MB. Calculations of B_1 distribution, specific energy absorption rate, and intrinsic signal-to-noise ratio for a body-size birdcage coil loaded with different human subjects at 64 and 128 MHz. Appl Magn Reson 2005;29:5-18.

110. Nagaoka T, Watanabe S, Sakurai K, Kunieda E, Watanabe S, Taki M, Yamanaka Y. Development of realistic high-resolution whole-body voxel models of Japanese adult males and females of average height and weight, and application of models to radio-frequency electromagnetic-field dosimetry. Phys Med Biol 2004;49:1.

111. Stabin MG, Emmons MA, Segars WP, Fernald MJ. Realistic reference adult and paediatric phantom series for internal and external dosimetry. Radiat Prot Dosim 2012;149:56-59.

112. Winkler SA, Rutt BK. Practical methods for improving B_1^+ homogeneity in 3 tesla breast imaging. J Magn Reson Imaging 2015;41:992-999.

113. van der Velden TA, Italiaander M, van der Kemp WJM, Raaijmakers AJE, Schmitz AMT, Luijten PR, Boer VO, Klomp DWJ. Radiofrequency configuration to facilitate bilateral breast ^{31}P MR spectroscopic imaging and high-resolution MRI at 7 tesla. Magn Reson Med 2014. doi: 10.1002/mrm.25573.

114. Morris E, Comstock C, Lee C. ACR BI-RADS® magnetic resonance imaging. In: ACR BI-RADS® atlas, breast imaging reporting and data system. Reston, Virginia: American College of Radiology; 2013. p. 125-143.

115. Zastrow E, Davis SK, Lazebnik M, Kelcz F, Van Veen BD, Hagness SC. Development of anatomically realistic numerical breast phantoms with accurate dielectric properties for modeling microwave interactions with the human breast. IEEE Trans Biomed Eng 2008;55:2792-2800.

116. Lazebnik M, Popovic D, McCartney L et al. A large-scale study of the ultrawideband microwave dielectric properties of normal, benign and malignant breast tissues obtained from cancer surgeries. Phys Med Biol 2007;52:6093.

117. Hasgall PA, Neufeld E, Gosselin M, Klingenböck A, Kuster N. IT'IS database for thermal and electromagnetic parameters of biological tissues. http://www.itis.ethz.ch/database. Updated: January 8, 2015. Accessed September 16, 2014. doi: 10.13099/ViP-Database-V2.5.

118. Cui J, Bosshard J, Rispoli J, Dimitrov I, Cheshkov S, McDougall M, Malloy C, Wright S. A switched-mode breast coil for 7 tesla MRI using forced-current excitation. IEEE Trans Biomed Eng 2015. doi: 10.1109/tbme.2015.2403850.

119. Yang QX, Wang J, Zhang X, Collins CM, Smith MB, Liu H, Zhu X-H, Vaughan JT, Ugurbil K, Chen W. Analysis of wave behavior in lossy dielectric samples at high field. Magn Reson Med 2002;47:982-989.

120. Klifa C, Carballido-Gamio J, Wilmes L, Laprie A, Lobo C, DeMicco E, Watkins M, Shepherd J, Gibbs J, Hylton N. Quantification of breast tissue index from MR data using fuzzy clustering. In Proceedings of the 26th Annual International Conference of the IEEE Engineering in Medicine and Biology Society, San Francisco, California, USA, 2004. p. 1667-1670.

121. Samani A, Bishop J, Yaffe MJ, Plewes DB. Biomechanical 3-D finite element modeling of the human breast using MRI data. IEEE Trans Med Imaging 2001;20:271-279.

122. Bakic PR, Zhang C, Maidment ADA. Development and characterization of an anthropomorphic breast software phantom based upon region-growing algorithm. Med Phys 2011;38:3165-3176.

123. Li CM, Segars WP, Tourassi GD, Boone JM, Dobbins JT. Methodology for generating a 3D computerized breast phantom from empirical data. Med Phys 2009;36:3122-3131.

124. Homann H, Börnert P, Eggers H, Nehrke K, Dössel O, Graesslin I. Toward individualized SAR models and in vivo validation. Magn Reson Med 2011;66:1767-1776.

125. Voigt T, Homann H, Katscher U, Doessel O. Patient-individual local SAR determination: in vivo measurements and numerical validation. Magn Reson Med 2012;68:1117-1126.

126. Zastrow E, Davis S, Lazebnik M, Kelcz F, Van Veen B, Hagness S. Database of 3D grid-based numerical breast phantoms for use in computational electromagnetics simulations. https://uwcem.ece.wisc.edu/phantomRepository.html. Updated February 21, 2014. Accessed September 16, 2014.

127. Doty FD, Inners RR, Ellis PD. A multinuclear double-tuned probe for applications with solids or liquids utilizing lumped tuning elements. J Magn Reson 1981;43:399-416.

128. Shen GX, Boada FE, Thulborn KR. Dual-frequency, dual-quadrature, birdcage RF coil design with identical B_1 pattern for sodium and proton imaging of the human brain at 1.5 T. Magn Reson Med 1997;38:717-725.

129. Matson GB, Vermathen P, Hill TC. A practical double-tuned $^{1}H/^{31}P$ quadrature birdcage headcoil optimized for ^{31}P operation. Magn Reson Med 1999;42:173-182.

130. Alecci M, Romanzetti S, Kaffanke J, Celik A, Wegener HP, Shah NJ. Practical design of a 4 tesla double-tuned RF surface coil for interleaved ^{1}H and ^{23}Na MRI of rat brain. J Magn Reson 2006;181:203-211.

131. Dabirzadeh A, McDougall MP. Trap design for insertable second-nuclei radiofrequency coils for magnetic resonance imaging and spectroscopy. Concepts Magn Reson Part B Magn Reson Eng 2009;35B:121-132.

132. Klomp DW, Renema WK, van der Graaf M, de Galan BE, Kentgens AP, Heerschap A. Sensitivity-enhanced ^{13}C MR spectroscopy of the human brain at 3 tesla. Magn Reson Med 2006;55:271-278.

133. Webb A, Smith N. 31P spectroscopy in human calf muscle at 7 tesla using a balanced double-quadrature proton-phosphorus RF coil. In Proceedings of the 18th Annual Meeting of ISMRM, Stockholm, Sweden, 2010. p. 3818.

134. Meyerspeer M, Roig ES, Gruetter R, Magill AW. An improved trap design for decoupling multinuclear RF coils. Magn Reson Med 2014;72:584-590.

135. Avison M, Hetherington H, Shulman R. Applications of NMR to studies of tissue metabolism. Annu Rev Biophys Biophys Chem 1986;15:377-402.

136. Serés Roig E, Magill AW, Donati G, Meyerspeer M, Xin L, Ipek O, Gruetter R. A double-quadrature radiofrequency coil design for proton-decoupled carbon-13 magnetic resonance spectroscopy in humans at 7T. Magn Reson Med 2015;73:894-900.

137. Serés Roig E, Xin L, Magill AW, Gruetter R. Towards 13C NMR spectroscopy of human muscle at 7T using broadband ^{1}H decoupling. In Proceedings of the 20th Annual Meeting of ISMRM, Melbourne, Victoria, Australia. p. 4425.

138. Herbert J. Ceramic dielectrics and capacitors. New York: Gordon and Breach Science; 1985. 264 p.

139. Grossbach R. Multi-Layer Ceramic Capacitors: Why & How They Fail. Passive Plus Web site. http://passiveplus.com/addldoc_uploads/MLCC.Reliability.FailureModes.Rev2014.pdf. Updated October 18, 2014. Accessed October 18, 2014.

140. Gauss R, Wong E, inventors; Koninklijke Philips Electronics N.V., assignee. RF traps for radio frequency coils used in MRI. US Patent 7,622,928. November 24, 2009.

141. Miyake Y, Yokomizo K, Matsuzaki N. Determination of unsaturated fatty acid composition by high-resolution nuclear magnetic resonance spectroscopy. J Am Oil Chem Soc 1998;75:1091-1094.

142. de Graaf RA, De Feyter HM, Rothman DL. High-sensitivity, broadband-decoupled ^{13}C MR spectroscopy in humans at 7T using two-dimensional heteronuclear single-quantum coherence. Magn Reson Med 2014. doi: 10.1002/mrm.25470.

143. Ogier S, Hollingsworth N, Rispoli J, McDougall M, Wright S. Adapting ^{1}H receivers for multi-nuclear MRS by frequency translation. In Proceedings of the Biomedical Engineering Society Annual Meeting, San Antonio, Texas, USA, 2014. p. P-Th-647.